Title
A Novel Search for Dark Photons

Author
Godfrey, Benjamin

Publication Date
2022

Peer reviewed|Thesis/dissertation

A Novel Search for Dark Photons

By

BENJAMIN P. GODFREY
DISSERTATION

Submitted in partial satisfaction of the requirements for the degree of

DOCTOR OF PHILOSOPHY

in

Physics

in the

OFFICE OF GRADUATE STUDIES

of the

UNIVERSITY OF CALIFORNIA

DAVIS

Approved:

S. Mani Tripathi, Co-chair

J. Anthony Tyson, Co-Chair

Brian H. Kolner

Committee in Charge

2022

Abstract

Over the course of nearly a century, astrophysical and cosmological evidence has suggested that a large portion of the universe's mass is comprised of some form of non-luminous matter. Called *dark matter*, its source remains an open question to the present day. Inspired by theories such as Supersymmetry (SUSY), in recent years, the weakly interacting massive particle (WIMP) hypothesis, has dominated the dark matter search landscape.

A generic, weak-scale, thermal relic WIMP could account for all of the observed dark matter in the universe, and experimenters continue to probe new WIMP parameter space by developing larger and more sensitive detectors. However, these experiments have detection thresholds for deposited energy, and they tend to lose sensitivity for low mass (below 10 GeV) dark matter particles. This leaves a large range of parameter space open for exploration, and new experiments are being launched to search in this region. Furthermore, while some effort has been directed towards detection of ultra-low mass (below 100 eV) dark matter candidates, all efforts to date have yielded null results, and the regime remains largely unexplored.

Extending the Standard Model (SM) to include an extra U(1) gauge symmetry, requires a new gauge boson called a *dark photon* that can couple very weakly to electrically charged particles. If the dark photon has mass, it will mix with the Standard Model (SM) photon. The mixing parameter effectively translates to a coupling strength ε, between the dark

photon and SM fermions. Due to its mass, it is also a candidate for low-mass dark matter.

This thesis describes the development of the Dark E-Field Radio Experiment: A wideband search for the weak electric field signature of a dark photon in the 200-1250 neV (50-300 MHz) mass range. The experiment utilized a commercial, real-time spectrum analyzer coupled to a wide bandwidth antenna. Over the course of 133 days, 3.8 hours of real-time data were collected and analyzed to set an upper limit on ε of $\sim 10^{-11.5}$. The experiment is the electromagnetic dual of magnetic detector dark radio experiments being carried out elsewhere. A paper based on this work has been peer-reviewed and published (Godfrey et al., 2021). Work done in preparation for the next phase of the experiment, along with suggestions for improvement to the current experimental design, are also described.

This work was supervised by Professors J. Anthony Tyson, S. Mani Tripathi, and Brian H. Kolner, and was performed in collaboration with scientists at Stanford University and the University of California, Davis.

Contents

Contents **iv**

List of Figures **vi**

List of Tables **viii**

1 The Dark Matter Story **1**
1.1 History of Dark Matter 1
1.2 Dark Matter Candidates 13
1.3 Dark Photon Physics 23
1.4 A Search for Dark Photons 31

2 Experimental Design and Verification **34**
2.1 Amplifier Requirements 36
2.2 Windowing 41
2.3 Sensitivity analysis 46
2.4 EM simulation of response 51
2.5 Isolation Testing of RF Shield 52
2.6 Signal Injection Tests 57

3 Signal Detection **61**
3.1 Description of the Filter 62
3.2 Filtering Experimental Data 74

4 Measurements and Results **81**
4.1 The Experiment 82
4.2 Data Acquisition and Analysis 83
4.3 Search for a Signal 86
4.4 Limits on ε in the 50–300 MHz Range 89

5 Improving Acquisition Efficiency for the Next Phase **96**
5.1 Design of the ROACH System 97

5.2 Using the ROACH 102
5.3 Reach of the proposed experiment 119

6 Future Plans and Conclusions **121**
6.1 Improvements in Understanding of the AF 121
6.2 Next Run Logistics 128

Bibliography **131**

List of Figures

1.1 Flattening of the rotation curves Rubin 4
1.2 Galaxy cluster CL0024+1654 5
1.3 The Bullet Cluster 7
1.4 Planck temperature anisotropies 9
1.5 Temperature power spectrum from Planck 2018 10
1.6 Sea of dark matter candidates 13
1.7 Exclusion limits on WIMP spin independent cross section 17
1.8 Feynman diagrams of axion decay 19
1.9 Current exclusion limits on dark photons 32
1.10 More room at the bottom 33

2.1 Schematic of Dark E-Field Radio Experiment 35
2.2 Block Diagram of Dark E-Field Radio Experiment 37
2.3 Various windows 42
2.4 Power spectrum of various windows 46
2.5 SNR dependence on number of scans 49
2.6 Time dependence of detection 50
2.7 COMSOL simulation of TE035 room mode 53
2.8 CST simulation of antenna factor 54
2.9 Shielding FM radio 56
2.10 Bicon amplitude spectral density 58
2.11 Power spectrum showing a 22σ detection at 70.5 MHz 59

3.1 Simulated time domain acquisition 63
3.2 Histogram of simulated time domain acquisition 64
3.3 Power spectrum of simulated acquisition 65
3.4 Example of shaping spectrum 66
3.5 Power spectrum after adding shaping signal 67
3.6 Butterworth highpass filter frequency response 68
3.7 Histogram of filtered magnitude-squared spectrum 70
3.8 Averaged power spectrum 71
3.9 Filtered averaged power spectrum 72

3.10 Histogram of filtered averaged power spectrum 73
3.11 Spur at 60.0 MHz 75
3.12 Frequency response of high pass Butterworth filter 76
3.13 Filtered span 77
3.14 Histogram of filtered data 79

4.1 Total system noise versus total system noise 84
4.2 Flowchart of the search process 87
4.3 Spot check limits 88
4.4 Candidate at 145.5 MHz 91
4.5 Candidate at 288 MHz 92
4.6 Spot limits overlaid with existing limits 93
4.7 Limit plot on ε in different stages 95

5.1 Picture of the ROACH system 97
5.2 ROACH design: ADC block 98
5.3 ROACH design: FIFO block 99
5.4 ROACH design: FIFO block 100
5.5 ROACH design: *Pkt_sim* subsystem 101
5.6 Spurious free dynamic range definition 105
5.7 ROACH terminated spectrum 107
5.8 Noise on DC-to-DC converters 111
5.9 Effect of setting the digital attenuator 112
5.10 Diagram for ROACH switching tests 114
5.11 Stability of ROACH spurs 117
5.12 Projected reach of the Dark E-Field Radio Experiment 120

6.1 Variation in energy density at modes of the room 126
6.2 Uncertainty in the energy density versus number of positions of the antenna . . 127
6.3 Preliminary event display 129

List of Tables

2.1 Window parameters of interest 45

4.1 Details of the initial run of the Dark E-Field Radio experiment 89

5.1 Spur stability results 118

Acknowledgments

I started my journey with UC Davis Physics over 10 years ago when I began clearing out lab spaces as an undergraduate. In that time, I have been very lucky to be part of a myriad of projects and work with a wide variety of people too numerous to mention here. Undoubtedly, I will forget names in this brief space, but know that, if you are reading this, you have had a hand in my development as a scientist and a person over the years.

Firstly, to the entire UC Davis Dark E-Field Radio Group - Amin, Brian, Daniel, Jon, Joseph, Mani, Molly, Paul, Seth, and Tony, it is amazing to see this project develop from an idea on a blackboard to where it is today. It is very rare nowadays to be able to see an experiment from design conception through to analysis over the course of a graduate school career. You have all played an instrumental role in making that happen, and I have been lucky to learn things from every one of you.

To the PI's of the group: Tony, your wisdom and expertise have proven a steady keel helping me navigate through whatever squalls may come up. I have learned to be a scientist under your guidance. To Brian, I really enjoyed our conversations. You always entertained my ideas, and you have taught me to think big. I always leave our discussions with an eye towards the future, and I hope to continue that. And finally, to Mani, I owe a huge debt of gratitude. We met in March 2011, my first year at Davis. I would never have imagined that we would be working together 11 years later (and onwards). You have been my advocate from day 1, and I am ever grateful for the mentorship you have provided both professional

and personal. I am excited to see what the future brings.

Joseph and Amin, I cannot imagine having a more fun group to work with. I genuinely enjoy getting to work with you guys. Every day I learn something new, and you are never afraid to discuss all sorts of crazy ideas. One of these days, I promise we will get lunch.

Jacob and Jyothis, you put up with me bothering you constantly. You guys have always been willing to listen and offer help, and I have appreciated getting to chat about whatever you are working on. Jyothis, very excited to see where your next journey goes. Jacob, don't stay a stranger.

To my roommates and friends, Ben, Jeff, and Kristine, you guys have provided immeasurable support throughout the years. You are always welcome back to Davis. The garden is suffering, and Oscar misses you.

To Olivia, your support over these many years has been perpetual. From inauspicious beginnings, we developed a relationship that has meant the world to me. While life may have thrown a curve ball or two, you are a friend through and through, and I trust you implicitly.

Finally, to family, Gary, Teresa, and Josh. To say I am lucky to have you guys is a disservice because it minimizes the role you all have played in getting me to this point. There are no words that can accurately describe how important you guys are to me. From physics conversations that last until the break of dawn to your unwavering, constant support, it is not an exaggeration that without you guys, I would not have been able to get to where I am today, and I am truly fortunate.

Chapter 1

The Dark Matter Story

1.1 History of Dark Matter

Astronomy at the turn of the twentieth century was heavily focused on stellar observations. Even though prisms had been around since Newton ([1]), it took until 1912 when John Stanley Plaskett began developing high enough quality diffraction gratings that allowed for the observation of both dimmer objects and the dynamics of celestial bodies [2]. This also coincided with the development of photographic plates as a recording mechanism for these spectra [3, p. 42].

By the early 1920's, efforts were underway to map out the local mass density of the Milky Way. In 1922, J.C. Kapteyn was one of the first to do this by modeling the shape and velocity profile of the Milky Way [4]. He established a relationship between the motion of stars and their velocity dispersion concluding that the effective mass density was higher than

the observed luminosity (M/L ratio) [5], although he ultimately concluded that *it appears at once that this mass cannot be excessive*[6]. This work was followed up by James Jeans, similarly finding a mismatch between mass density and luminosity in the Milky Way. In 1932, Jan Oort, Kapteyn's student, provided a more detailed analysis to understand the kinematics of stars in the local solar neighborhood and also provided an estimate of the local mass density once again finding that there was more matter than suggested from looking at the luminosity of the stellar objects [5].

Contemporaneous with the work of Kapteyn and Jeans, Alexander Friedman showed that Einstein's field equations allowed for the possibility of an expanding universe [7]. This was independently derived in 1927 by Georges Lemaître [8]. Hubble built off these results experimentally showing the linear relationship between the distance to an object and its recessional velocity due to the expansion of space [9]. This important result lead to the famous work of Fritz Zwicky who is popularly attributed with coining the phrase *dark matter* [5].

Looking at eight galaxies within the Coma Cluster, Zwicky used the virial theorem to relate the velocity dispersion of the galaxies to the gravitational potential energy. Doing this, Zwicky found a large discrepancy between the two, finding that the galaxies had a larger velocity dispersion than expected attributing *das dunkle Materie*, to non-luminous astrophysical objects [4, 10].

While World War Two brought with it untold amounts of devastation, it also hastened the development of radar, which ended up a boon for the astronomical community. Old military radars were re-purposed for astronomical observations, heralding the start of radio

astronomy [4]. This in turn hastened the discovery of the hydrogen line, an electromagnetic spectral line from microwaves coming from the hyperfine transition of the hydrogen 1s ground state. First predicted in 1944 by Oort's student, Hendrik van de Hulst, de Ewen and Purcell experimentally observed it in 1951[11, 12].

This incredibly important discovery sets the stage for a significant amount of astrophysical evidence for the existence of dark matter. The discovery of the hydrogen line allowed astronomers to peer out to large radii through the interstellar cosmic dust that is opaque to visible light.

1.1.1 Rotation Curves

By the 1960's, radio observations confirmed the large mass-to-light ratios seen by Zwicky for individual galaxies up to galaxy clusters [14, 15]. And new technology enabled astronomers to look further out onto the edges of galaxies. The most famous example is the work of Vera Rubin and Kent Ford. Building on the development of a new image tube spectrograph that allowed observation of stars previously too faint to see, Kent Ford and Vera Rubin performed spectroscopic observations of the Andromeda Galaxy looking at the rotational velocity of stars versus distance from the galactic center. A plot from [13] is reproduced in Figure 1.1 showing how rotation velocity flattens out as distance from the center increases.

Now able to look far out from the galactic center, Rubin and Ford's work both expanded the regime of optical spectroscopy and also deepened the mystery of what was causing the

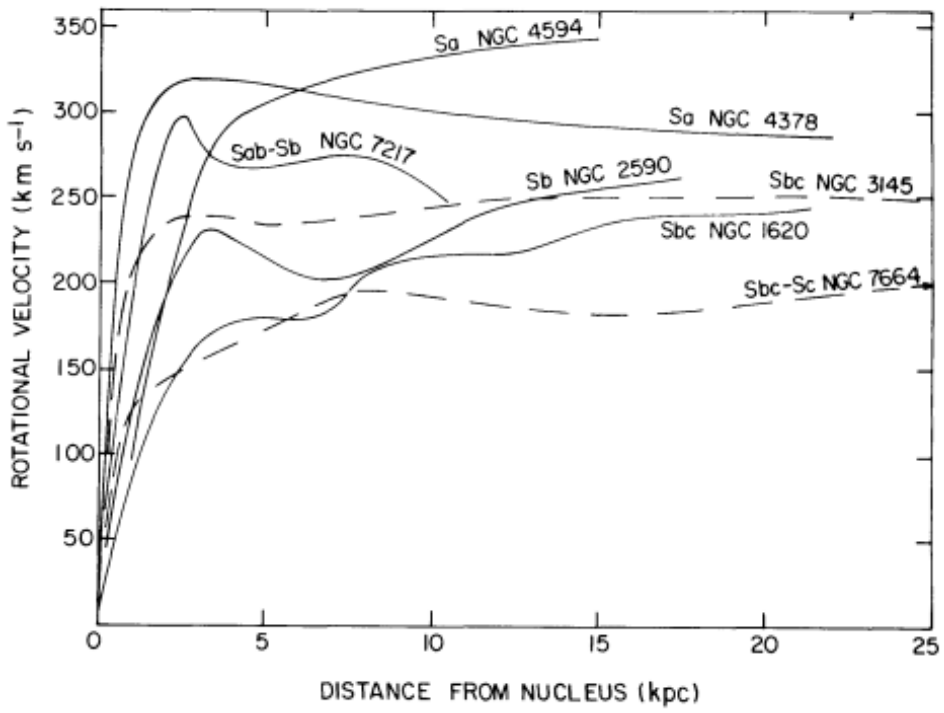

Figure 1.1: Plot from Rubin's 1978 paper *Extended Rotation Curves of High-Luminosity Spiral Galaxies* showing rotational velocities of seven galaxies versus distance from the nucleus [13].

flattening of the rotation curves [16].

It was during this time that explicit statements arguing for additional mass began to appear. Ken Freeman's seminal 1970 paper compared the radius that rotation curves were expected to peak, assuming an exponential mass distribution, using optical data compared to the observed 21cm rotation curves for both M33 and NGC300 spiral galaxies. He found that there must be missing mass with a different mass distribution than what was visible [17].

Today, the astrophysical evidence supporting the the presence of dark matter extends past the presence of large mass-to-light ratios. We now go through a brief summary of some of that evidence.

1.1.2 Gravitational Lensing

Figure 1.2: Galaxy cluster CL0024+1654 (reddish yellow) lensing a background ring galaxy into five images, evident by their faint blue color. The cluster distorts the five images somewhat differently, which is due to the effects of the cluster's gravitational potential [18][19].

In 1916, Einstein published his general theory of relativity that relates energy and momentum to the curvature of spacetime [20, 21]. Since light travels the path of least time, it will appear to bend around massive objects. This effect, is called *gravitational lensing*. Predictions of gravitational lensing are variously attributed to Khvolson, Link, and Einstein ([22–24]). However, it was not until 1979 that the first gravitational lens was discovered [25]. An example of lensing is shown in Figure 1.2 in which a background ring galaxy is lensed by a foreground galaxy cluster to create multiple copies of the same galaxy.

Because dark matter only interacts gravitationally, lensing provides a mechanism by which to discover its effect on EM radiation. Lensing is separated into three categories: Strong, weak, and micro.

Strong lensing is characterized by easily visible distortions of a background source such as arcs, rings, or multiple images. Weak lensing is a statistical measurement, looking at correlations in the shapes of many background objects. Finally, for microlensing, the mass of the foreground object is too low for the displacement of light to be easily seen. However, variation in the brightness of the background object may still be detected. This depends on the lens passing in front of the source in a reasonable amount of time (relative to a human lifespan) in order to be observed [26]. Weak lensing measurements have provided mass measurements of one of the most famous pieces of evidence for dark matter: The *Bullet Cluster*[4, 5].

Discovered in 1998, the Bullet Cluster is one of the strongest pieces of evidence for the nature of dark matter. The cluster consists of two colliding galaxies located 3.7 billion

Figure 1.3: False color composite image of Galaxy Cluster 1E 0657-56, also known as the *Bullet Cluster*. Red shows the location of hot gas detected by the Chandra X-ray Observatory in X-rays. Blue shows the areas with the greatest mass concentration determined from gravitational lensing studies [27].

light years away from Earth. The galaxies contain three main components: Stars, gas, and dark matter. Each behaves differently during the collision. Stars, observable in the visible spectrum, are not affected by the collision and pass right through each other. Gas, seen in X-rays, and comprising most of the visible mass, are slowed down via electromagnetic interactions. Finally, dark matter is observable via weak lensing of background objects. If dark matter interacted through the weak interaction, lensing would be strongest near the X-ray gas. Instead, it is strongest in two regions nearby the visible galaxies. This is

in agreement with predictions that dark matter only interacts gravitationally[27]. This is commonly cited as evidence against theories that do not include dark matter like Modified Newtonian Dynamics (MOND) [4]. A false color composite image of the Bullet Cluster is shown in Figure 1.3.

1.1.3 Cosmic Microwave Background (CMB)

Current understanding of universe formation is that a scalar field called the *inflaton field* drove a period of rapid expansion in the universe called inflation [28]. After the initial expansion, the inflaton field decayed creating a hot, dense, but uniform plasma. This in turn created a mixture of quarks, gluons, and, ultimately, hadrons and leptons. During this time, the lack of neutral particles meant that photons were readily absorbed and re-emitted through Thomson scattering [29, Chapter 21.2]. As the universe continued to cool, charged particles combined to form atoms approximately 370,000 years after the Big Bang[30]. Now that the evolving universe was transparent to light, photons were able to travel long distances and this primordial echo is what we see as the CMB [29, Chapter 28][31].

Discovered serendipitously by Arno Penzias and Robert Wilson in 1964, the CMB looks like a 2.725K black body today and provides primary evidence for the Big Bang model of the creation of the universe[33]. The first map of the CMB was done by the Cosmic Microwave Background Explorer (COBE) between 1989 and 1993 [34]. Since then, much effort has gone into developing experiments to measure the CMB at ever finer angular scales. Most

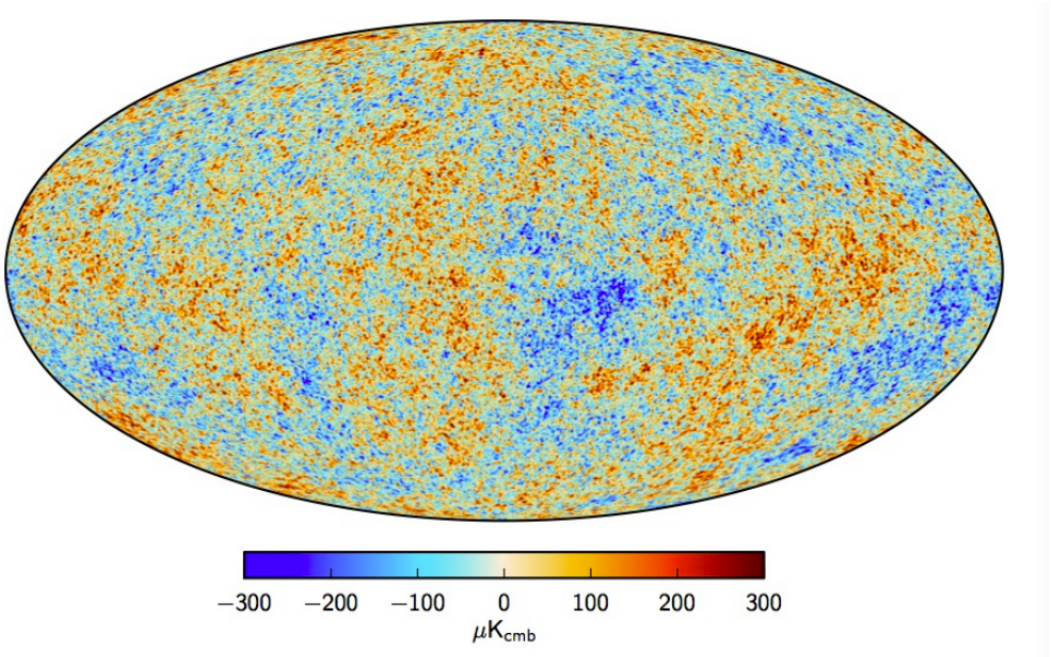

Figure 1.4: Temperature anisotropies of the CMB measured by the Planck space telescope. Reproduced from [32].

notably are the results from the Wilkinson Microwave Anisotropy Probe (WMAP) and the Planck observatory. These experiments revealed that while there was near uniformity in all directions, there were small residual temperature fluctuations explainable from quantum fluctuations in the very early universe quickly expanding out to cosmological scales (Figure 1.4) [35] [36].

Prior to recombination, the universe acted much like a harmonic oscillator. Density fluctuations pulled baryons together, which were then pushed apart when the over-density became too high and radiation pressure forced them apart. As recombination occurred, these fluctuations became locked into place resulting in density waves in the primordial plasma,

which are seen today as anisotropies in the angular power spectrum [37, 38].

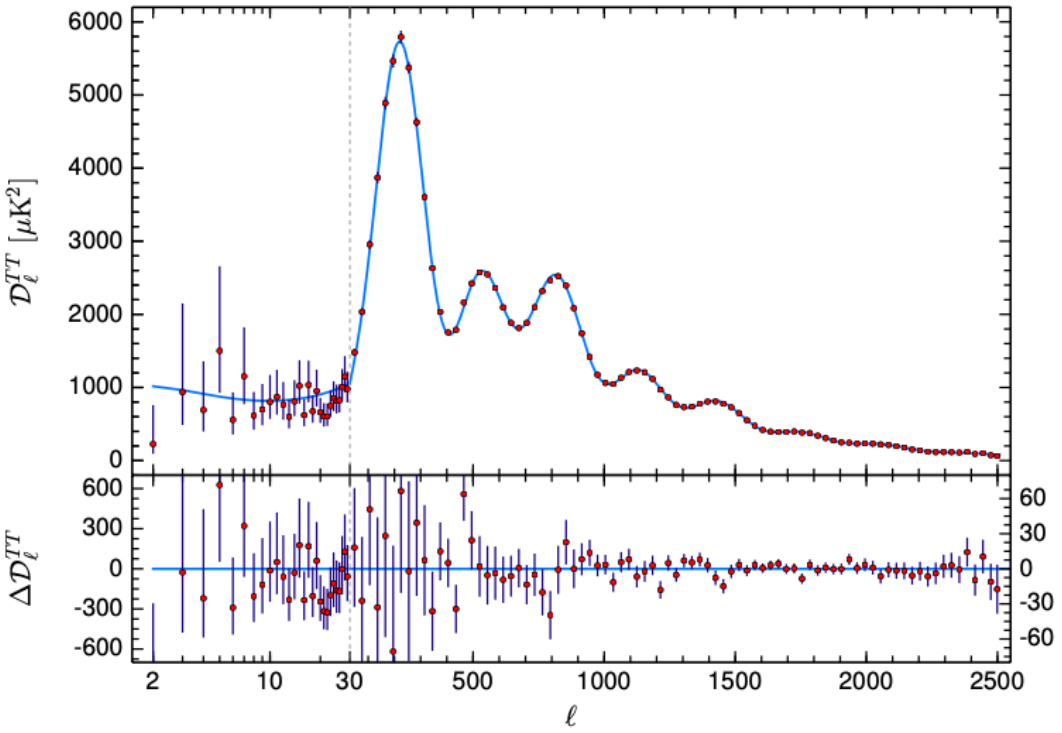

Figure 1.5: Temperature power spectrum from Planck 2018 results showing the spherical harmonic decomposition of the temperature power spectrum. The m index has been averaged over, which partially explains the larger variance at large angular scales (small ℓ). A theoretical spectrum is overplotted in light blue in the upper panel. Residuals with respect to this model are shown in the lower panel. The error bars show $\pm 1\sigma$ error bars [36].

The angular power spectrum measured from the Planck 2018 measurement of the CMB anisotropies is shown in Figure 1.5. The size, shape, and location of these peaks inform models for various parameters of the Universe and give bounds on the amount of baryonic matter, dark matter, and dark energy in the universe. For example, under current understanding, a peak around $\ell = 200$ indicates a flat universe. This in turn informs the energy

density required to maintain a flat universe, which gives an estimate on the amount of dark energy. It is also hypothesized that the abundance of dark matter influences the relative height of the third peak relative to the second peak [39]. Planck 2018 results find that

$$\Omega_\Lambda = 0.6847 \pm 0.0073 \tag{1.1}$$

$$\Omega_m = 0.3153 \pm 0.0073 \tag{1.2}$$

$$\Omega_b = 0.04924 \pm 0.00033 \tag{1.3}$$

corresponding to the fractional mass densities of dark energy, dark matter, and baryonic matter, respectively [36]. All values are normalized with respect to a critical density

$$\begin{aligned} \rho_0 &= \frac{3H^2}{8\pi G} \\ &\approx 8.6 \times 10^{-27} \mathrm{kg}/m^3, \end{aligned} \tag{1.4}$$

defined as the average matter density required to halt the expansion of the universe after an infinite time [40]. This thesis will not discuss dark energy, but a good review is in [41].

Big Bang Nucleosynthesis provides an independent measure of the baryon mass density by looking at the relative abundances of light elements besides ^{1}H that were produced from around 10 s until around 20 min after the Big Bang [42]. Immediately after hadronization, nuclear reactions of the sort

$$n + e^+ \rightleftarrows \overline{\nu}_e + p \tag{1.5}$$

$$n + \nu_e \rightleftarrows p + e^- \tag{1.6}$$

kept the ratio of protons to neutrons close to parity[43]. As temperature dropped, the number density of protons increased over neutrons due to their slightly lower mass. These reactions slowed down until it became energetically unfavorable when the temperature of the universe was approximately 0.8 MeV.[1] Neutrons continued to decay into protons until the temperature cooled below the energy that photons could disassociate deuterium signaling the production of bound light nuclei (around 0.1 MeV) and light elements (mostly ^{4}He) up to lithium. Looking at the mass fraction of any of the light elements, allows the computation of the baryon-to-photon number density. Multiple elements gives further confirmation of the model [44].

Current measurements give a baryon-to-photon ratio of

$$n = (5.931 \pm 0.051) \times 10^{-10} \tag{1.7}$$

[45] and a baryon density of

$$\Omega_b h^2 = 0.02235 \pm 0.000016 \pm 0.00033 \tag{1.8}$$

[46], which is consistent with CMB results in Equation 1.3. Here, h is the reduced Hubble constant defined by the dimensionless quantity

$$h = \frac{H_0}{100\,\mathrm{km}/\,(\mathrm{s}\cdot\mathrm{Mpc})}. \tag{1.9}$$

[1] As a point of reference 1 eV corresponds to approximately 11,600 K.

1.2 Dark Matter Candidates

In light of the overwhelming evidence in support of missing mass, theories have been proposed to explain what the missing mass may be. A survey of them is given in Figure 1.6 showing the sea of possibilities. A few are highlighted and discussed in this section.

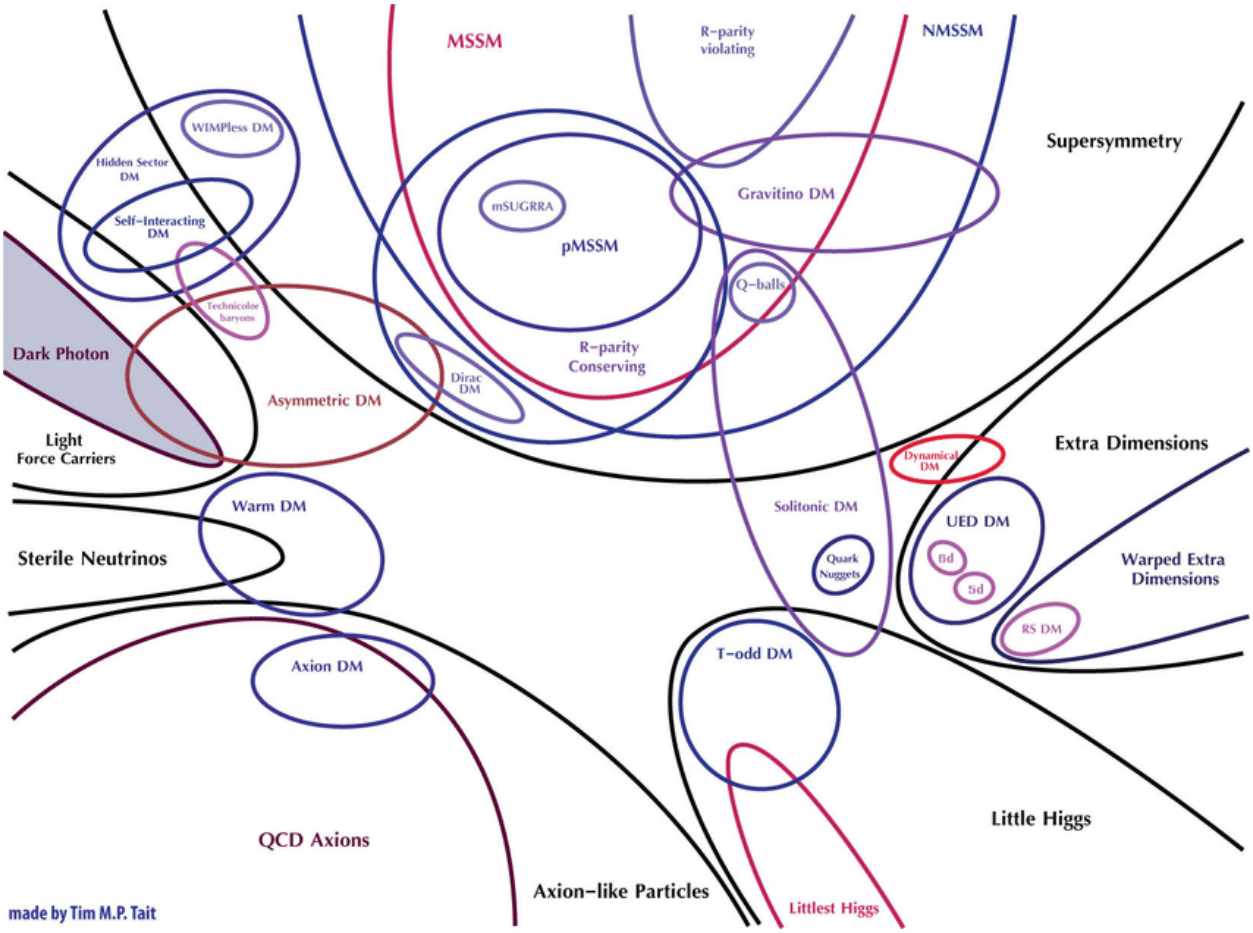

Figure 1.6: Sea of dark matter candidates showing highlighting the wide variety of theoretical candidates [from T. Tait][47]

.

1.2.1 Baryonic matter

A natural candidate for dark matter is normal baryonic matter that is massive but non-luminous. The mass range of these massive compact halo objects (MACHOs) spans a wide mass range from 10^{-9} to $10^{-6}M_{\odot}$ [48, 49]. Candidates include black holes, neutron stars, red, white and brown dwarfs, and planets.

Gravitational micrloensing surveys have searched for MACHOs in mass ranges over many orders of magnitude and found that they cannot contribute a significant fraction of the total dark matter mass in the galaxy [50–55]. Observations by the Hubble Space Telescope of the faint spectroscopic signature from red dwarfs showed that they compose only a small fraction of the dark matter halo mass.

CMB observations constrain the amount of mass attributable to primordial black holes. When black holes accrete matter, they emit X-rays, which then become microwaves due to Thomson scattering and cosmic expansion. These microwaves distort the CMB isotropy, which means limits on their numbers can be set by looking at the temperature variations of the CMB [56]. These calculations have mostly ruled out primordial black holes as the dominant form of dark matter, which effectively rules out MACHOs [57–59].

1.2.2 Weakly Interacting Massive Particles (WIMPs)

To obtain the observed dark matter abundance via thermal production requires a self-annihilation cross section approximately equal to what is expected for a weakly interacting

massive particle of order 100 GeV. This coincidence, combined with the prevailing opinion that most of the mass in the Universe consists of cold, non-baryonic particles has pushed the WIMP hypothesis to be one of the leading dark matter candidates for more than 35 years because a generic weak-scale thermal relic could account for all of the observed dark matter in the universe.

Thermal production of WIMPs during the early universe was kinematically allowed until the temperature of the universe cooled below the WIMP mass. At this point, self-annihilation reduced the number density until the mean free time for annihilation exceeded the age of the universe. This so called *freeze-out* is what accounts for the current density of WIMPs [60].

WIMP searches are broadly focused in three main areas: Indirect, direct, and particle searches. Indirect searches comprise astronomic searches for annihilation or decay products of WIMPs such as high energy gamma rays that are a byproduct of either direct annihilation or the inverse Compton scatter of charged particles. Non-observation of an annihilation signal sets limits on the WIMP annihilation cross section [61].

Direct detection searches comprise lab-based detection techniques to observe the effect of a WIMP-nucleus collision. There are many such experiments with a few different detection modalities. Noble gas detectors such as DEAP, XENON, DarkSide, DARWIN, and LZ use a noble element as a scintillation medium to detect the charge and light yield of a WIMP-nucleus interaction. Similarly, there are experiments that use scintillating crystals instead of a noble gas as a detection medium. These include experiments like DAMA/Libra (which famously observed an annual modulation in the number of detection events consistent with

WIMP detection), IceCube (looking for an excess of solar neutrinos that could be explained by solar WIMP annihilation), ANAIS, and COSINE. Other experiments such as CDMS, CoGeNT, CRESST, and EDELWEISS use cryogenic crystal detectors to measure the heat generated by a WIMP vibrating the crystal lattice. Bubble chambers like PICO and COUPP look for WIMP energy depositions inducing acoustic shock waves in a superheated liquid. A comprehensive list of references to these experiments are contained in [62].

Even with all this experimental effort, no conclusive evidence for WIMPs has been found. Measured and predicted limit curves for the spin-independent cross section versus mass for various experiments are given in Figure 1.7. Null results from these searches have motivated alternative theories.

1.2.3 Neutrinos

Long thought to have zero mass, the disappearance of atmospheric muon neutrinos, as evidenced by an up-down asymmetry at the Super-Kamioka Neutrino Detection Experiment (Super-K) provided the first indication of oscillations[64] and implied neutrinos have a non-zero rest mass. Further proof of oscillations was in the resolution of the long-standing solar neutrino problem, wherein the observed flux of electron neutrinos was about one-third of what was expected from prevailing models of the sun [65]. This was then confirmed by comparing the rates of charged current versus neutral current neutrino interactions because only electron neutrinos participate in charged current interactions below the muon mass

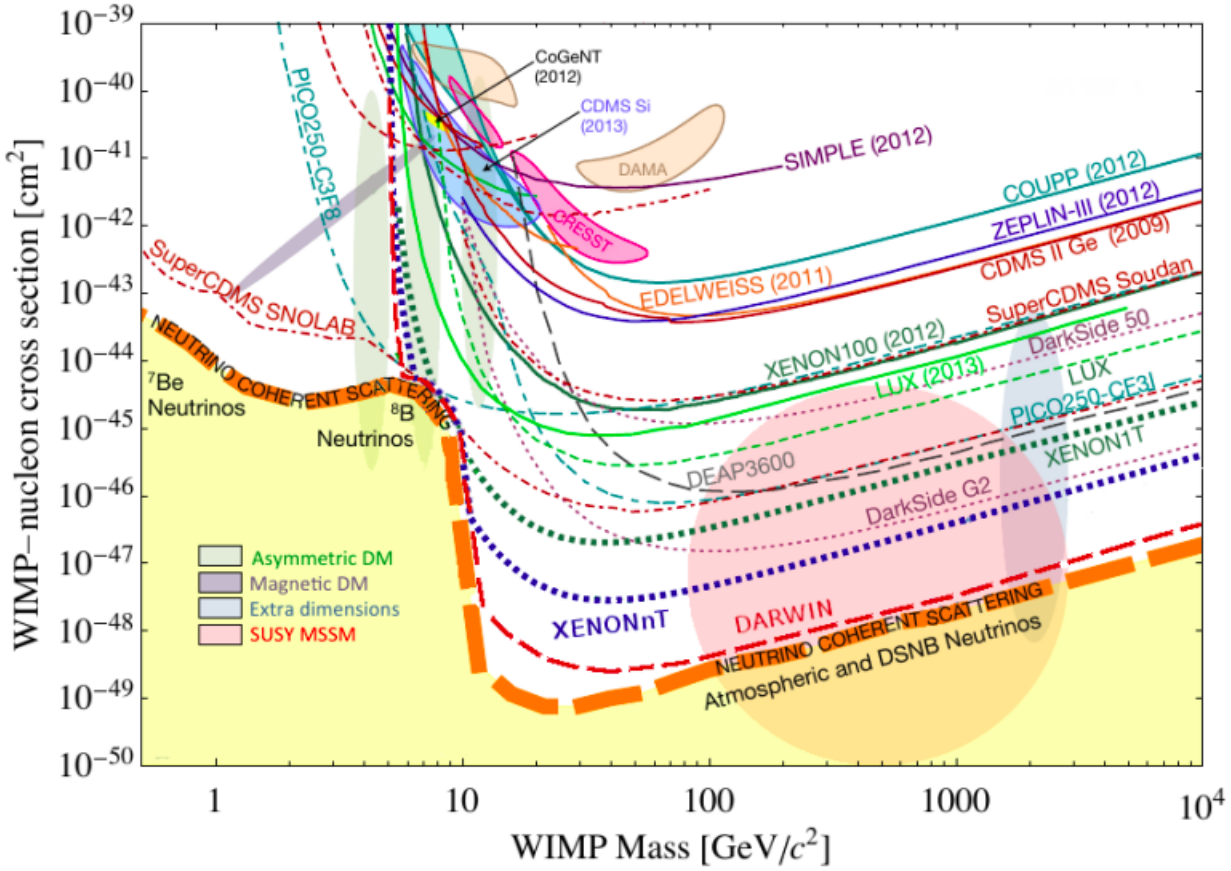

Figure 1.7: Exclusion limits on the WIMP spin independent cross section vs. WIMP mass for various experiments both pass and future. The yellow region shows the neutrino floor, where detectors will be able to see the neutral current interaction of a neutrino and a nucleus. This irreducible background makes exploration below this floor very difficult [63].

threshold, whereas all three species can undergo neutral current interactions[66].

Since neutrinos are uncharged under electromagnetism, they qualify as a dark matter candidate due to their small mass. However, current constraints on neutrino masses make them too light and not abundant enough to be a major contributor to the dark matter density

[67]. Furthermore, since they are relativistic and free streaming, they do not contribute towards dark matter clumping and galaxy formation [68].

Searches are ongoing, however, to look for *sterile* neutrinos. Such particles would have opposite chirality to SM neutrinos and could have a large mass [69]. Experimental efforts searching for sterile neutrinos, are inconclusive thus far [69–72]. However, sterile neutrinos remain a viable dark matter candidate.

1.2.4 Axions

Quantum chromodynamics predicts that charge parity (CP)-symmetry should be violated in the strong sector. A byproduct of this prediction is that the neutron, because it is a hadron, should have an electric dipole moment. However, current limits on the neutron electric dipole moment suggest a very small CP violating term. Thus, even though theory predicts that CP violation should exist in the strong sector, no experiment has seen it. This fine-tuning problem is known as the *strong CP* problem [73].

Named after its founders, Roberto Peccei and Helen Quinn, the Peccei-Quinn theory introduces a new scalar field into the SM Lagrangian charged under a new U(1) symmetry that allows for the construction of a quantum chromodynamics Lagrangian that ensures CP symmetry. At some energy scale, spontaneous symmetry breaking creates a pseudo-Nambu–Goldstone boson. This light, psuedoscalar is called an *axion*. The non-zero (negative) vacuum expectation value of the axion field cancels out the CP violating term in the SM

Lagrangian giving a solution to the strong CP problem. Theory predicts that this symmetry breaking should happen below the electroweak scale. Since the energy scale is inversely proportional to the mass, this predicts very light particles. Astronomical bounds place the mass between $10^{-5} < m_a < 10^{-3}\,\text{eV}$ although axion-like particles (ALPs) are theoretically motivated at mass scales many orders of magnitude lower [74].

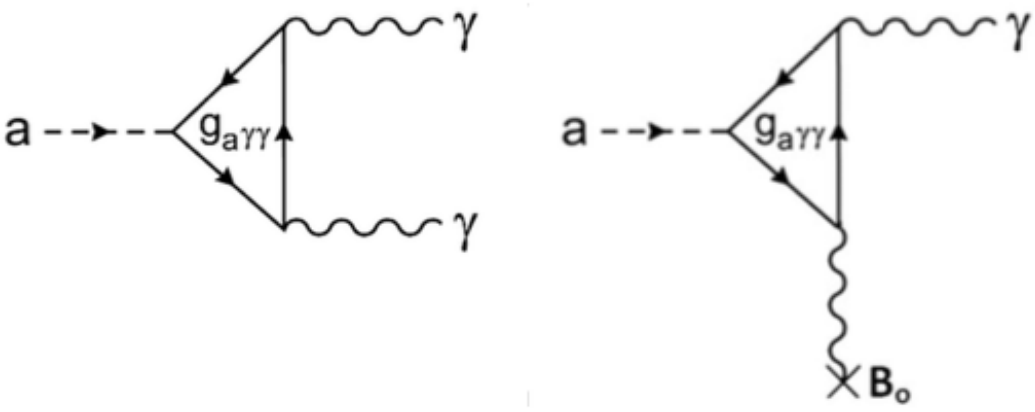

Figure 1.8: Feynman diagrams of axion decay into photons through a quark loop. (Left) The conversion of axions into two photons in vacuum. (Right) The inverse Primakoff effect in a static magnetic field [75].

Axions are postulated to have been produced in the early universe via the misalignment mechanism. This non-thermal process generated a cosmological population of cold axions with an abundance depending on the mass of the axion [76–78]. This production mechanism is one of the possible ways that dark photons could have been produced in the early universe as well [79]. Because axions are produced non-thermally, even though they have low mass, they constitute a cold dark matter candidate [80]. This has important implications on

the history of structure formation in the early universe. In the cold dark matter model, small objects collapse under their self-gravity first, eventually merging with other objects to form more massive structures. This is in general agreement with current observations of cosmological structure in the universe [36, 81–83].

The electromagnetic interaction of the axion with field strength a and coupling $g_{a\gamma\gamma}$ is governed by the interaction Lagrangian given as

$$\mathcal{L}_{a\gamma\gamma} = g_{a\gamma\gamma} a \mathbf{E} \cdot \mathbf{B} [75, 84]. \tag{1.10}$$

This informs the diagram shown in Figure 1.8. There are two general direct detection methods: Light-shining-through wall (LSW) and haloscope experiments [85]. Both take advantage of the Primakoff effect, which is the resonant production of neutral pseudoscalar mesons created via the interaction of two photons with an atomic nucleus [86] [84].

LSW experiments take advantage of high photon flux densities to look for photon excess in a region past an electromagnetically opaque barrier. The experimental goal is that in the presence of a strong magnetic field, placed before the barrier, photons convert into axions via the traditional Primakoff effect. Then, after the barrier, axions convert back to photons via the inverse Primakoff effect and are observed as a photon excess. However, the requirement of two conversions means that the observed power is only proportional to the fourth power of $g_{a\gamma\gamma}$ [87].

Axion haloscopes look for production of axions inside a radio frequency (RF) cavity. The resonance of the cavity provides a large enhancement to masses at the resonance frequency of

the cavity given by the quality factor of the cavity itself [88]. Furthermore, the requirement of only a single axion-to-photon conversion means that the power observed is proportional to the square of the axion-photon coupling constant [89].

The design of axion haloscopes has informed experimental design for dark photon searches [90, 91] too. Furthermore, the experimental signature from axions is nearly equivalent to dark photons except for a couple things:

1. Since dark photons kinetically mix into photons they do not require a magnetic field for detection.

2. Dark photons have an intrinsic polarization (depending on production mechanism) while axions have a preferred direction set by the applied magnetic field.

However, axion limits can be used to set dark photon limits as shown in [85] and [92].

1.2.5 Dark Photons

As already introduced, dark photons are hypothetical, low-mass, gauge bosons, which have been posed as a candidate for dark matter. They are theoretically motivated via fluctuations of a vector field during the early inflation epoch of the universe. A relic abundance of such a particle could be produced non-relativistically in the early universe in a similar way to axions, through either the misalignment mechanism or through quantum fluctuations of the inflaton field [93, 94].

In contrast to axions, a massive, inflation-produced vector boson like a dark photon would have a power spectrum that is peaked at a length scale of roughly 10^{10} km and rapidly decreases in intensity at large length scales. This is important because current CMB observations disfavor large scale CMB fluctuations (see Figure 1.5). Furthermore, a dark photon would adopt the adiabatic fluctuations of the inflaton making it a good dark matter candidate [94]. The high phase space density required for dark photons to constitute a significant portion of the local dark matter density ($\sim 0.3\,\mathrm{GeV}/cm^3$) implies that they would behave as an oscillating field with a frequency equal to the mass of the dark photon. In general, for a theory with two U(1) symmetries, there would be some weak coupling with a corresponding term in the Lagrangian [95–97]. The Lagrangian then varies from the standard model, $\mathcal{L}_{SM}$, as shown in Equation 1.11.

$$\mathcal{L} = -\frac{1}{4}F'_{\mu\nu}F'^{\mu\nu} + \frac{1}{2}m^2A'_\mu A'^\mu - \frac{1}{2}\varepsilon F'_{\mu\nu}F^{\mu\nu}_{EM} + \mathcal{L}_{SM} \tag{1.11}$$

Here m is the mass of the dark photon (determined from its Compton-equivalent frequency), $F_{\mu\nu}$ and A_μ are the electromagnetic field strength and gauge potential, $F'_{\mu\nu}$ and A'_μ are the dark photon field strength and gauge potential, and ε is the dark photon-to-electromagnetic coupling factor, which must be measured. The mixing term between the two coupled fields is then $\frac{1}{2}\varepsilon F'_{\mu\nu}F^{\mu\nu}_{EM}$. Through kinetic mixing, dark photons would be detectable in traditional electromagnetic searches, and ε can be measured. A summary of previous experimental bounds on ε from direct detection experiments is given in [98].

1.3 Dark Photon Physics

Searches for particles beyond the SM have focused on particles that have at least some of the gauge interactions of SM particles. Null results in these searches motivate increased interest in the *dark sector*. This dark sector (or hidden sector) comprises a collection of quantum fields and their corresponding hypothetical particles operating in parallel with the SM world. Contained within these states is dark matter.

Now, if the dark sector were only to interact gravitationally, then lab-based detection would be nigh impossible. Hope hinges that the dark and standard sectors also interact through a *portal* that is experimentally accessible (in lab-based experiments).

This portal may take various forms, defined by the type and dimension of its operators. These are generally specified by the spin of the mediator and are given by: Higgs (scalar), axion (pseudo-scalar), neutrino (spin 1/2), and vector (spin 1) [99].

A dark photon is identified as the boson of an extra U(1) symmetry (exactly like a massive SM photon). First identified by Bob Holdom in 1986 [95], an additional U(1) symmetry would mix between the SM photon and the new gauge boson implying that the dark photon can change back and forth between a dark and SM photon. It is this kinetic mixing that provides a detection *portal*.

There are actually two types of dark photons: Massive and massless. From an experimental point of view, the massive case is more compelling for a couple of reasons: Firstly,

to be a viable dark matter candidate, the dark photon needs to be massive.[2] Secondly, it couples directly to SM currents making it accessible for lab-based searches. As a result, everything that follows will focus on the massive case.

1.3.1 Massive Dark Photons

The Lagrangian for two, Abelian, gauge bosons described by two gauge groups $U(1)_a$ and $U(1)_b$, is given by:

$$\mathcal{L} = \underbrace{-\frac{1}{4}F_{a\mu\nu}F_a^{\mu\nu} - -\frac{1}{4}F_{b\mu\nu}F_b^{\mu\nu} - \frac{\varepsilon}{2}F_{a\mu\nu}F_b^{\mu\nu}}_{\text{kinetic}} + \underbrace{eJ^\mu {A_b}^\mu + e'J'^\mu {A_a}^\mu}_{\text{interaction}} - \underbrace{\frac{1}{2}M_b^2 A_{b\mu}A_b^\mu}_{\text{mass}} \tag{1.12}$$

Here, the gauge boson, A_b^u, is assumed to couple to the SM four-current $J^\mu = e\overline{\psi}\gamma^\mu\psi$. Likewise, the SM gauge boson, A_a^u, is assumed to couple to the dark four-current J'^μ. Consistent with current understanding, the mass of the standard photon field has been set to 0. It is assumed that the dark photon acquires a mass by means of the Stueckelberg mechanism. This is discussed in Section 1.3.2. The Lagrangian has been separated into kinetic, interaction, and mass parts, and is labeled accordingly.

We can make the interaction between the gauge fields manifest by diagonalizing the gauge fields

$$\begin{bmatrix} A_a^\mu \\ A_b^\mu \end{bmatrix} = \begin{bmatrix} \frac{1}{\sqrt{1-\varepsilon^2}} & 1 \\ \frac{-\varepsilon}{\sqrt{1-\varepsilon^2}} & 0 \end{bmatrix} \begin{bmatrix} \cos\theta & \sin\theta \\ -\sin\theta & \cos\theta \end{bmatrix} \begin{bmatrix} A'^\mu \\ A^\mu \end{bmatrix}. \tag{1.13}$$

[2]The dark photon could be a portal to a dark sector with other dark sector particles that may have SM interactions.

Note that the second matrix in the transformation is a general 2d-rotation matrix parameterized by an arbitrary rotation angle. Specifically, this angle parameterizes a mixing matrix and defines the angle between the charge and mass basis vectors.[3] This rotation is always possible because of the Spectral Theorem that says that a real, square, symmetric matrix is orthogonally diagonalizable [101]. We will see that simultaneously diagonalizing the mass terms of the Lagrangian fixes this angle.

We begin the diagonalization process by focusing on the kinetic part of the Lagrangian and plugging in using the definition of the field tensor $F^{\mu\nu} = \partial^\mu A^\nu - \partial^\nu A^\mu$.

$$F_{a\mu\nu}F_a^{\mu\nu} = \frac{1}{1-\varepsilon^2}\cos^2\theta F'_{\mu\nu}F'^{\mu\nu} + \frac{1}{1-\varepsilon^2}\sin^2\theta F_{\mu\nu}F^{\mu\nu} - 2\frac{\sin\theta\cos\theta}{1-\varepsilon^2}F'^{\mu\nu}F_{\mu\nu} \tag{1.14}$$

$$\begin{aligned} F_{b\mu\nu}F_b^{\mu\nu} = &\left(\sin\theta - \frac{\varepsilon\cos\theta}{\sqrt{1-\varepsilon^2}}\right)^2 F'_{\mu\nu}F'^{\mu\nu} + \left(\cos\theta + \frac{\varepsilon\sin\theta}{\sqrt{1-\varepsilon^2}}\right)^2 F_{\mu\nu}F^{\mu\nu} \\ &+ 2\left(\sin\theta - \frac{\varepsilon\cos\theta}{1-\varepsilon^2}\right)\left(\cos\theta + \frac{\varepsilon\sin\theta}{1-\varepsilon^2}\right)F'_{\mu\nu}F^{\mu\nu} \end{aligned} \tag{1.15}$$

$$\begin{aligned} F_{a\mu\nu}F_b^{\mu\nu} = &\frac{\cos\theta}{\sqrt{1-\varepsilon^2}}\left(\sin\theta - \frac{\varepsilon\cos\theta}{\sqrt{1-\varepsilon^2}}\right)F'_{\mu\nu}F'^{\mu\nu} - \frac{\sin\theta}{\sqrt{1-\varepsilon^2}}\left(\cos\theta + \frac{\varepsilon\sin\theta}{\sqrt{1-\varepsilon^2}}\right)F_{\mu\nu}F^{\mu\nu} \\ &- \frac{\sin\theta}{\sqrt{1-\varepsilon^2}}\left[\cos\theta + \sin\theta + \frac{\varepsilon}{\sqrt{1-\varepsilon^2}}(\sin\theta - \cos\theta)\right] \end{aligned} \tag{1.16}$$

Combine equations 1.14-1.16 together to obtain the kinetic part of the diagonalized Lagrangian

$$\mathcal{L}_{diag} = -\frac{1}{4}F'_{\mu\nu}F'^{\mu\nu} - -\frac{1}{4}F^{\mu\nu}F^{\mu\nu}. \tag{1.17}$$

[3] An analog is the PMNS matrix that quantifies the relationship between the mass- and flavor-eigenstate bases for neutrinos[100].

We can go through similar steps for the interaction Lagrangian. Plugging in 1.13 then gives the following

$$\begin{aligned}\mathcal{L}' = &\left[\frac{e'\cos\theta}{\sqrt{1-\varepsilon^2}}J'_\mu + e\left(\sin\theta - \frac{\varepsilon\cos\theta}{\sqrt{1-\varepsilon^2}}\right)J_\mu\right]A'^\mu \\ &+ \left[\frac{e'\sin\theta}{\sqrt{1-\varepsilon^2}}J'_\mu + e\left(\cos\theta - \frac{\varepsilon\sin\theta}{\sqrt{1-\varepsilon^2}}\right)J_\mu\right]A^\mu.\end{aligned} \tag{1.18}$$

For right now, the mixing angle θ is arbitrary and interaction between dark/SM currents and dark/EM currents is made apparent.

Finally, we diagonalize the mass terms of the Lagrangian. We will start by defining the Lagrangian for two U(1) gauge bosons that acquire a mass via the Stueckelberg Lagrangian (see Section 1.3.2)

$$\mathcal{L}_{\text{Stu}} = -\frac{1}{2}M_a^2 A_{a\mu}A_a^\mu - \frac{1}{2}M_b^2 A_{b\mu}A_b^\mu - M_a M_b A_{a\mu}A_b^\mu. \tag{1.19}$$

Note that in equation 1.12 that the mass of the a gauge boson has been set to 0.

The orthogonal matrix R that defines the diagonalization of the mass matrix is given by

$$M_{\text{diag}} = R^T\left(Q^T M_{\text{Stu}} Q\right)R \tag{1.20}$$

where Q is the GL(2) transformation defined in Equation 1.13 and R is the orthogonal transformation parameterized by the mixing angle θ. Multiplying out the matrix of the quadratic form of $\mathcal{L}_{\text{Stu}}$ and the kinetic diagonalization matrix from Equation 1.13 the matrix to be diagonalized is given by

$$\begin{bmatrix} \frac{1}{\sqrt{1-\varepsilon^2}} & \frac{-\varepsilon}{\sqrt{1-\varepsilon^2}} \\ 1 & 0 \end{bmatrix}\begin{bmatrix} M_a^2 & M_aM_b \\ M_aM_b & M_b^2 \end{bmatrix}\begin{bmatrix} \frac{1}{\sqrt{1-\varepsilon^2}} & 1 \\ \frac{-\varepsilon}{\sqrt{1-\varepsilon^2}} & 0 \end{bmatrix} = \begin{bmatrix} \frac{M_a^2+\varepsilon^2M_b^2-2\varepsilon M_aM_b}{1-\varepsilon^2} & \frac{M_b^2-M_aM_b}{\sqrt{1-\varepsilon^2}} \\ \frac{M_aM_b-\varepsilon M_b^2}{\sqrt{1-\varepsilon^2}} & M_b^2 \end{bmatrix}. \tag{1.21}$$

Orthogonalizing this matrix then gives the following

$$\frac{1}{\sqrt{1-2\delta\varepsilon+\delta^2}}\begin{bmatrix} 1-\delta\varepsilon & -\delta\sqrt{1-\varepsilon^2} \\ \delta\sqrt{1-\varepsilon^2} & 1-\delta\varepsilon \end{bmatrix} \tag{1.22}$$

where $\delta = \frac{M_b}{M_a}$. Comparing this to the general orthogonal transformation in Equation 1.13, we can read off the solution for the mixing angle θ and find that

$$\theta = \tan^{-1}\left(\frac{\delta\sqrt{1-\varepsilon^2}}{1-\delta\varepsilon}\right). \tag{1.23}$$

If we associate M_b and M_a with the standard and dark photon masses, respectively, then $\theta = 0$, and we can rewrite the interaction Lagrangian in Equation 1.18 as

$$\mathcal{L}' = \left[\frac{e'}{\sqrt{1-\varepsilon^2}}J'_\mu + \frac{\varepsilon e}{\sqrt{1-\varepsilon^2}}J_\mu\right]A'^\mu + eJ_\mu A^\mu. \tag{1.24}$$

Thus, we find that when $\delta = 0$, the SM photon couples only to the normal EM current, but the massive dark photon couples to both the standard and dark currents. The strength of the interaction to the standard EM current is read off as

$$\mathcal{L}_{\text{dark}\to\text{EM}} = \frac{\varepsilon e}{\sqrt{1-\varepsilon^2}}J_\mu A'^\mu \approx \varepsilon e J_\mu A'^\mu. \tag{1.25}$$

This milli-charged (tiny fraction of the charge of an electron), direct-coupling to standard EM is what sets up a possible detection mechanism in lab-based experimental searches. Interestingly, by setting the mass of the SM photon to 0, it removed the possibility of EM milli-charged particles.[4]

[4]The arguments made in this section are based on results given in [99] and [102].

1.3.2 Stueckelberg mechanism

In general, the QED Lagrangian does not allow a mass term. This is easily seen by looking at the mass term for the free photon field

$$\mathcal{L}_\gamma = m^2 A^\mu A_\mu. \tag{1.26}$$

If the Lagrangian is gauge invariant then it is unchanged under a transformation of the form $A^\mu \rightarrow A^\mu + \partial^\mu \Lambda$. Plugging in to equation 1.26 then gives $\mathcal{L}'_\gamma \rightarrow (A^\mu + \partial^\mu \Lambda)(A_\mu + \partial_\mu \Lambda)$. This is not equal to $\mathcal{L}_\gamma$.

However, construction of a gauge invariant theory is important. For example, charge conservation is a consequence of gauge invariance. And renormalizable theories are required to be gauge invariant [103].

Ernst Stueckelberg devised a clever way around this[5] by introducing a new scalar field $\phi(x)$ and defining the following gauge transformations

$$A^\mu(x) \rightarrow A^\mu(x) + \partial^\mu \Lambda(x) \tag{1.27a}$$

$$\phi(x) \rightarrow \phi(x) - \Lambda(x). \tag{1.27b}$$

In order for the Lagrangian to be invariant under the gauge transformations, redefine the gauge field such that

$$A^\mu = A'^\mu - \partial^\mu \phi. \tag{1.28}$$

[5]This is a summary of [104].

The new gauge field is now invariant under the new gauge transformations given in Equations 1.27a and 1.27b. We can see how this works by looking at the free field Lagrangian of a massive spin-1 field given by

$$\mathcal{L}_{\text{free}} = -\frac{1}{4}F_{\mu\nu}F^{\mu\nu} - \frac{1}{2}m^2 A_\mu A^\mu. \tag{1.29}$$

Plugging in the redefinition of the gauge fields given by 1.29 then gives the following in full form

$$\begin{aligned}\mathcal{L}_{\text{free}} = &-\frac{1}{4}\left[\partial_\mu\left(A'_\nu - \partial_\nu\phi\right) - \partial_\nu\left(A'_\mu - \partial_\mu\phi\right)\right]\left[\partial^\mu\left(A'^\nu - \partial^\nu\phi\right) - \partial^\nu\left(A'^\mu - \partial^\mu\phi\right)\right] \\ &-\frac{1}{2}m^2\left(A'_\mu - \partial_\mu\phi\right)\left(A'^\mu - \partial^\mu\phi\right).\end{aligned} \tag{1.30}$$

This can then be simplified to

$$\mathcal{L}_{\text{free}} = -\frac{1}{4}F^{\mu\nu}F_{\mu\nu} - \frac{1}{2}m^2 A'^\mu A'_\mu + m^2\partial_\mu\phi A'\mu - \frac{1}{2}m^2\partial_\mu\phi\partial^\mu\phi. \tag{1.31}$$

Making the gauge choice $\phi(x) = \Lambda(x)$ sets $\phi(x) = 0$ and leaves the same result as in Equation 1.29. Doing this, we have constructed a gauge invariant theory of a massive vector boson.

1.3.3 Proca Action

The Lagrangian of a massive spin-1 particle is given by [6]

$$\mathcal{L} = -\frac{1}{4}F^{\mu\nu}F_{\mu\nu} + \frac{1}{2}m^2 A^\mu A_\mu. \tag{1.32}$$

[6] These results are a summary of notes from [105].

This looks very much like the source free EM Lagrangian with an extra mass term. Plugging into the Euler-Lagrange equation gives the equation of motion as

$$\Box A^{\mu} - \partial^{\mu} \left(\partial_{\nu} A^{\nu} \right) + m^2 A^{\mu} = 0. \tag{1.33}$$

General plane wave solutions to Equation 1.33 are given by

$$A^{\mu} (x) = \mathrm{Re} \left[\epsilon^{\mu} (p) \, e^{-ip \cdot x} \right], \tag{1.34}$$

where $\epsilon^{\mu} (p)$ is a polarization vector. Plugging in this solution into Equation 1.33 then gives

$$p^2 \epsilon^{\mu} - \left(p^{\nu} \epsilon_{\nu} \right) p^{\mu} - m^2 \epsilon^{\mu} = 0. \tag{1.35}$$

Consider first solutions of the form

$$p^{\mu} \cdot \epsilon_{\mu} = 0. \tag{1.36}$$

In this case, Equation 1.35 becomes

$$\left(p^2 - m^2 \right) \epsilon = 0. \tag{1.37}$$

Then in the rest frame

$$p^{\mu} = \begin{bmatrix} m \\ 0 \\ 0 \\ 0, \end{bmatrix} \tag{1.38}$$

which means that $\epsilon^0 = 0$. The other solution is that $\epsilon^{\mu} (p) = c p^{\mu}$. In this case, Equation 1.33 becomes

$$- m^2 \epsilon^{\mu} = 0. \tag{1.39}$$

This is only satisfied in the trivial case. Thus, it cannot generally exist. Since $\epsilon^0 = 0$, ϵ^u transforms as a 3-vector with components $[0, \mathbf{e}_h]$. Here, the h index specifies the helicity of the polarization vector, which is the projection of the spin-axis onto the direction of momentum. Notice that there are now three degrees of freedom corresponding to $h = 0, \pm 1$. The 0 helicity state represents the longitudinal mode of the massive vector field, which is not allowed by Maxwell (massless spin-1 particles). Graham *et al.* argue in [94] that this longitudinal mode is important because inflation contains a mechanism for the copious production of longitudinal modes that is consistent with CMB observations and could explain the measured dark matter density.

1.4 A Search for Dark Photons

Ultimately, the physical nature of dark matter is unknown. Several highly sensitive searches for weakly interacting massive particles (WIMPs) have failed to observe a signal [106]. The 2014 P5 report [107] emphasizes the importance of searching for dark matter in the entire mass scale using every feasible experimental technique to do so. To date, relatively little effort has been spent on detection of ultra-low mass dark matter candidates, where it is best described as a wave rather than a particle [108]. Figure 1.9 shows the spectrum in both mass and frequency domains and highlights the techniques that have or can be applied in various ranges.

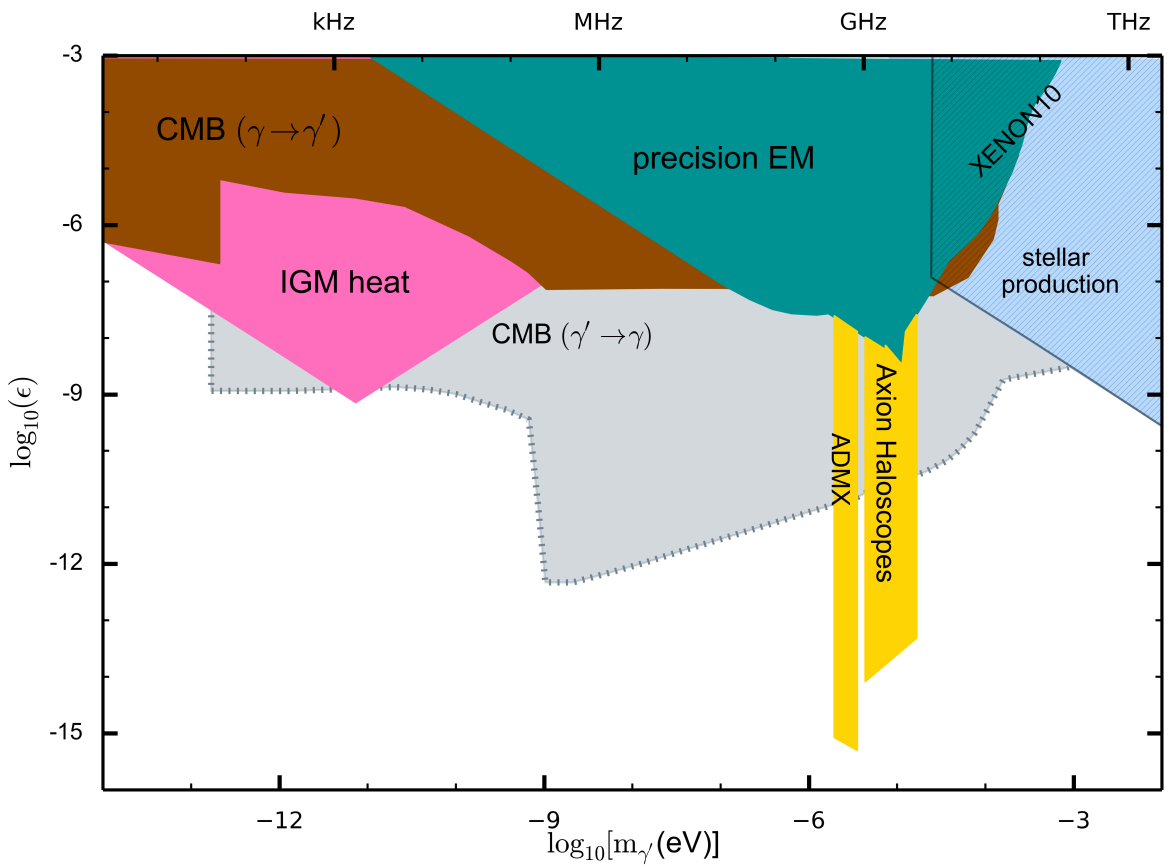

Figure 1.9: Current exclusion limits on dark photons showing coupling constant versus mass range. Regions excluded by both experiment and astrophysics are shown.

A significant fraction of the available phase space in the low mass spectrum, has not yet been explored even though dark matter may exist there as shown in 1.10, wherein the excluded space is shown in various colors. Investigating this parameter space requires the development of new strategies, which invariably lead to new detection concepts.

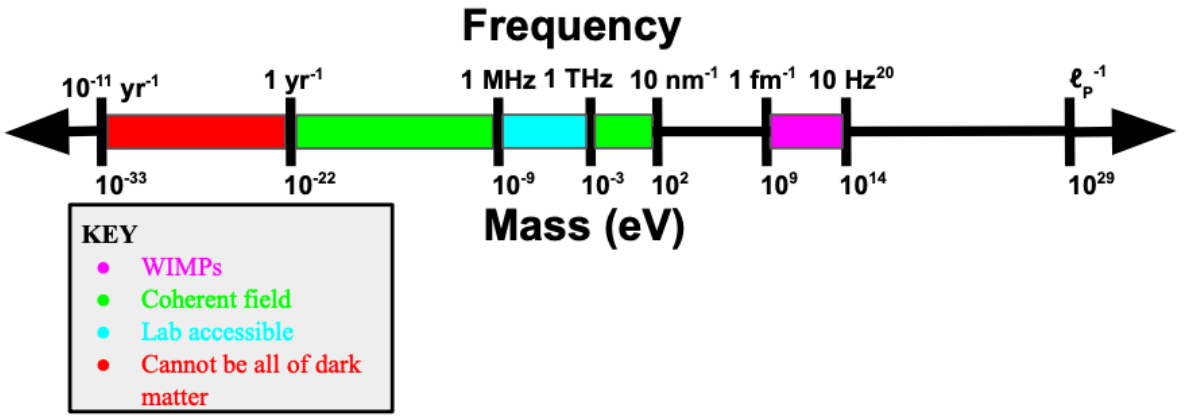

Figure 1.10: WIMP searches have focused on the region in purple, but there is a wide area of unexplored phase space especially in low mass regions.

To this end, we have built an experiment to search for dark photons in the nano- to milli -eV (50-300 MHz) mass range. This experiment is the electromagnetic dual of magnetic dark photon experiments performed by Parker *et al.*, [109] and Chaudhuri *et al.*, [110]. We have completed a feasibility test of the *Dark E-field Radio* experiment, which has shown that the full experiment can work. The strategy for searching for dark photons is discussed in Chapter 2.

Chapter 2

Experimental Design and Verification

In designing the Dark E-Field Radio Experiment there are two overarching unknowns: The mass of the dark photon, and the coupling strength to SM fermions, ε. The coupling strength is determined by measuring the weak electric field signature from a dark photon converting into a normal photon. The mass of the photon is determined by the measurement frequency, ν. Candidates will have a spectral width defined by a fractional bandwidth Q given as

$$\frac{\delta\nu}{\nu} \approx v^2 \approx 10^{-6} = \frac{1}{Q}, \tag{2.1}$$

which comes from the orbital velocity, v, ([110, 111]) of the Earth ($\sim 10^{-3}c$) with respect to a non-rotating galactic frame (assuming that dark matter forms a virialized, non-rotating smooth halo). Therefore, the goal is to detect very small electric fields over a wide bandwidth with a Q of one part-per-million (ppm) or better over the entire spectral range.[1]

[1] If fractional resolution is greater than 10^6 the signal to noise ratio stays fixed.

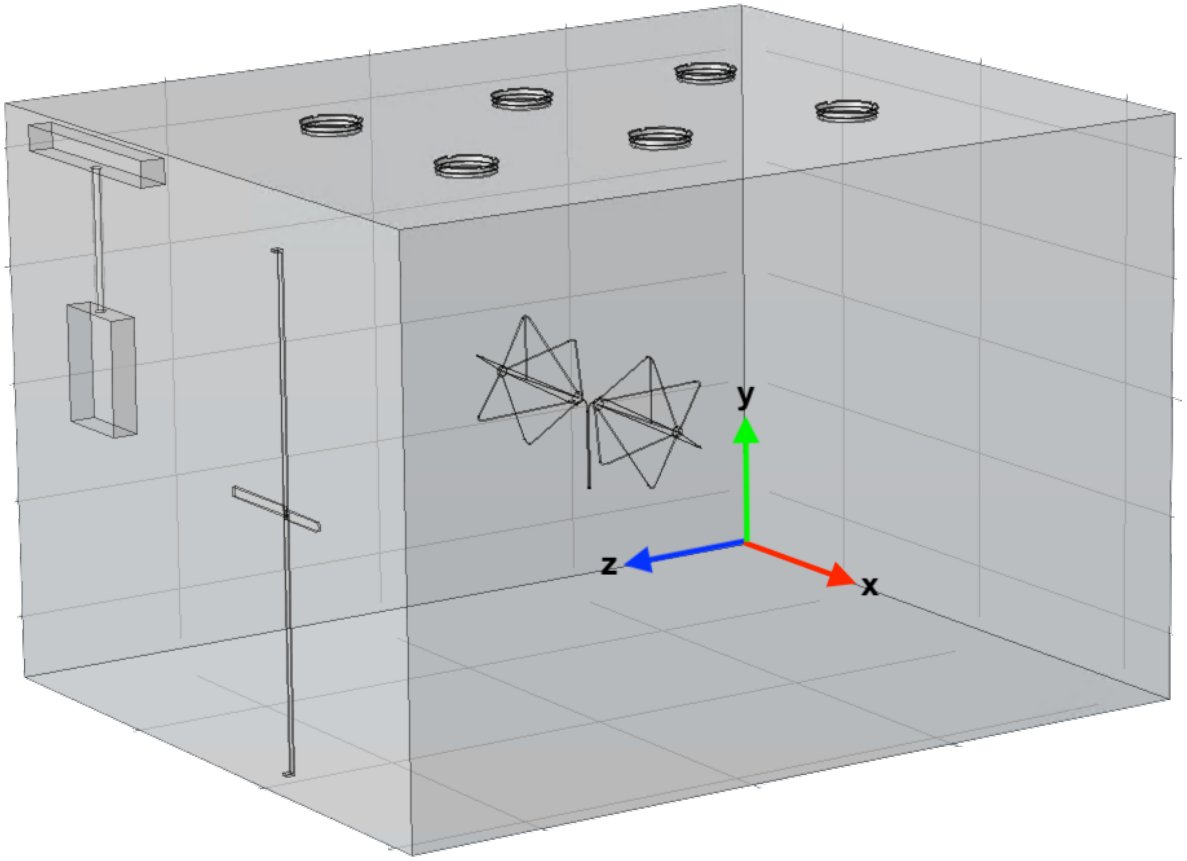

Figure 2.1: The Dark E-Field Radio Experiment inside a large electromagnetic shielded room, searching for a narrowband signal between 30 MHz and 20 GHz from dark photons converting inside the shield. The antenna is placed in the center of the room. Features that affect the modes of the room are shown including light fixtures, electrical box, and door latch. All of these impact the antenna's response to wall currents. The output from the antenna is fed into an LNA inside the shield, whose buffered output is connected to a wideband, real-time, spectrum analyzer for data processing (Rigol RSA-5065-TG). See Figure 2.2 for a block diagram.

Because the coupling strength is weak, we need to shield external RF sources from interfering with candidate signals. Figure 2.1 shows the current 50–300 MHz setup in a

$3.05 \times 2.45 \times 3.67\,m$ commercial shielded room with $\sim$100 dB isolation. Conducting features in the room that affect simulations over a 50–300 MHz range have been included in the solid model. The antenna is placed in the center of the room. Conductive features such as light fixtures, electrical box, and door latch all impact the antenna's response to wall currents and the conversion of incident electric field to a voltage at the feedpoint of the antenna.

The output from the antenna is then fed into a low-noise amplifier (LNA) inside the shield, whose buffered output is connected to a wideband, real-time, spectrum analyzer for data processing. Ultimately, the sensitivity is limited by the thermal noise of the walls, however, it is important to have an amplifier whose noise temperature is subdominant to the temperature of the room. Amplifier requirements are discussed in Section 2.1. A block diagram of the experimental setup is shown in Figure 2.2.

The coherence of the dark photon signal can be leveraged by coherent averaging of the power spectrum. Variance of the incoherent, wideband amplifier/thermal noise will reduce proportional to the number of averages improving the signal-to-noise ratio (SNR) although only proportional to the quarter root of the number of averages. This is discussed in further detail in Section 2.3.

2.1 Amplifier Requirements

It is important that an amplifier is included in the signal chain in order to raise the power from the antenna above the displayed average noise level (DANL) of the spectrum analyzer.

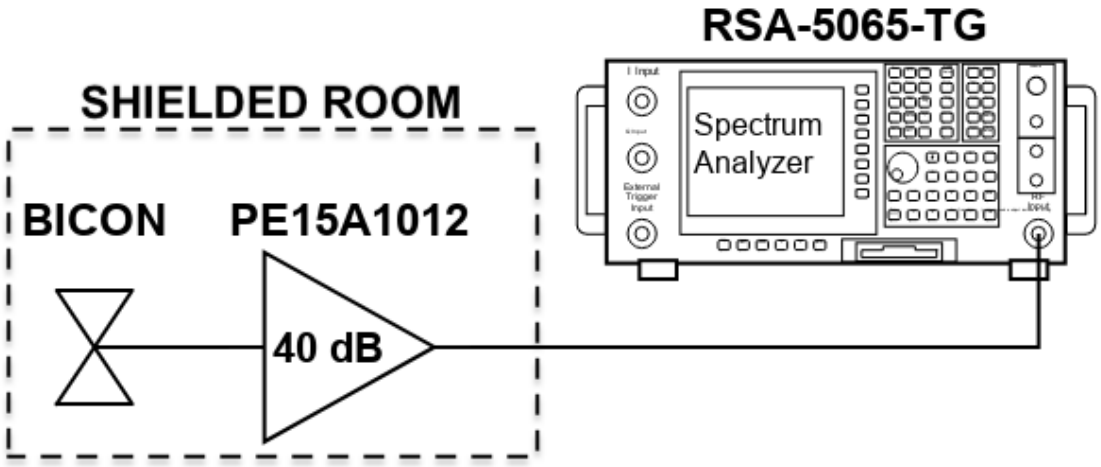

Figure 2.2: Block diagram of the Dark E-Field Radio Experiment (not to scale). The low noise, Pasternack PE15A12012, amplifier is directly coupled to the access panel inside the shielded room while the biconical antenna is placed at the center of the room. They are connected via coaxial cable. Output from the LNA is fed to a Rigol RSA-5065-TG spectrum analyzer, which is controlled via a PC (not shown). The role of the LNA is to raise the level of the power measured by the biconical antenna, which is mostly thermal/Johnson noise, above the baseline noise level of the Rigol spectrum analyzer.

The DANL is normally specified as a power spectral density (PSD). In the region of interest this is

$$\mathrm{DANL}_{\mathrm{RIGOL}} \sim -160 \left[\frac{\mathrm{dBm}}{\mathrm{Hz}}\right]. \tag{2.2}$$

Here, dBm is a logarithmic quantity defined by

$$P_{\log} = 10\log_{10}\left(\frac{P_{\mathrm{lin}}}{1\mathrm{mW}}\right) \tag{2.3}$$

where P_{lin} is a power measured in mW. From this, we can do a calculation to determine requirements for the amplifier.

Since this experiment is being done at room temperature, the PSD of thermal noise is specified by the Johnson noise formula as $k_B T$. At 300 K, this is -174 dBm/Hz. To ensure that the noise from the spectrum analyzer is subdominant to the noise from the antenna, we set a threshold of 20 dB. Then 1 % of the measured power is due to the spectrum analyzer. This is also the gain of the front-end preamplifier on the commercial spectrum analyzer, which simplifies the calculation.

From this, the required amplifier gain is then

$$\begin{aligned} G_{\mathrm{dB}} &= \frac{P_{\mathrm{Rigol}}}{P_{\mathrm{Johnson}}} \\ &= -160\,\mathrm{dBm/Hz} - (-174\,\mathrm{dBm/Hz}) \\ &= 14\,\mathrm{dB}. \end{aligned} \tag{2.4}$$

While this is true for a single acquisition, coherent averaging will increase the SNR such that we are sensitive to baseline fluctuations at the level of the DANL of the spectrum analyzer. This improved SNR is specified by an *averaging gain* that is vitally important in being able to set a good limit on ε, but it also increases the SNR of spurious signals from the spectrum analyzer. If we assume a spur (a high Q signal that mimics a dark photon signal) at the DANL of the spectrum analyzer, then we would like the power in any candidate dark photon signal to be at least 20 dB above the level of a spur. This is very similar to the requirement that the spectrum analyzer noise is 1 % of the amplified power coming from the biconical antenna. However, now, we are requiring that the standard deviation of the power measured by the spectrum analyzer be 20 dB higher than the DANL of the spectrum analyzer.

Since the antenna power has a flat PSD (because it is mostly thermal), its variance decreases as the number of samples, n. Therefore, the standard deviation goes down as $n^{1/2}$. If we would like this to remain true for 10 hours of real-time acquisition, and each acquisition takes 100 ms, then the averaging gain is given by

$$\begin{aligned} G_{\text{avg}} &= 5\log_{10}\left(\frac{10\,\text{h} * 3600\,\text{s/hr}}{0.1\,\text{s/scan}}\right) \\ &= 28\,\text{dB}. \end{aligned} \tag{2.5}$$

Equivalently, this says that the standard deviation decreases by a factor of 631 ($10^{2.8}$) compared to a single acquisition over the course of a 10-hour, real-time, data run. This is discussed further in Chapter 5 for the new ROACH data acquisition system. The nominal gain of the amplifier is then

$$\begin{aligned} G_{\text{amp}} &= 14\,\text{dB} + 28\,\text{dB} \\ &= 42\,\text{dB}. \end{aligned} \tag{2.6}$$

It is because the limit on ε is ultimately set by the standard deviation of the measured power (see Chapter 3), that we are able to relate the physical and averaging gain, which is a statistical quantity. For the experiment, we chose a 40 dB LNA since it closely matched these requirements. Note that adding further gain into the system is risky because of spectrum analyzer saturation and feedback. Saturating the preamplifier on the spectrum analyzer causes a non-linear amplifier response, which means that the input power level, and ultimately the

incident electric field strength on the antenna, is poorly defined. Feedback effects occur when power from the output of the amplifier feeds back into the input. If this power gets radiated into the room, it can pump up modal structure of the room causing spurious signals, which may also saturate the preamplifier/spectrum analyzer.

Assuming wide-bandwidth noise, we can integrate the baseline across the entire 1 GHz bandwidth of the amplifier to make sure that we are well below the saturation level of the spectrum analyzer[112].

$$\begin{aligned}\int_{\nu_{\text{low}}}^{\nu_{\text{high}}} d\nu k_B \left(T_{\text{room}} + T_{\text{amp}}\right) G_{\text{amp}} &\approx k_B \left(300\,\text{K} + 100\,\text{K}\right) \cdot 10^9\,\text{Hz} \cdot 10^6 \\ &= 5.5 \cdot 10^{-3}\,\text{mW} \\ &= -22.6\,\text{dBm}.\end{aligned} \tag{2.7}$$

Here, a 100 K noise temperature front-end amplifier is assumed. Total gain is the product of the external amplifier gain (40 dB) and the internal preamplifier on the spectrum analyzer (20 dB) for a total of 60 dB of gain. Maximum input power on the spectrum analyzer is 30 dBm (1 mW), which we are well below.

Choosing an LNA is important but not overly so. Because this experiment is being done at room temperature, we are ultimately limited by the 300 K walls of the room. A consequence of this, is that there is marginal improvement between a room temperature and a cryogenic LNA. The amplifier we chose has a 60 K noise temperature. This is also specified

in terms of a noise figure (NF) given as

$$NF_{\mathrm{dB}} = 10\log_{10}\left(1 + \frac{T_{\mathrm{amp}}}{T_0}\right) \tag{2.8}$$

where T_0 is a reference temperature. As defined, the NF is non-zero for all non-zero T_{amp}. For a reference temperature of 25 °C, 60 K corresponds to a 0.8 dB NF[112].

However, even if we had a 0 K amplifier, the improvement in the total system temperature is then $(1 - 300/360) \times 100 \approx 16\%$. Since ε is proportional to $T^{1/2}$, then this ultimately improves the limit on ε by 8 %. As a rule of thumb, we would like an amplifier whose noise temperature is under half the 300 K thermal noise of the room.[2]

2.2 Windowing

A discrete Fourier transform (DFT) projects a (periodically extended) set of samples onto an orthogonal set of sinusoids.[3] If the frequencies in the sampled set do not align with the finite basis, there will be non-zero projections on the entire basis set. This is called *spectral leakage*. In general, a set of data will have sharp discontinuities at the boundaries. These boundaries introduce leakage over the entire basis set, which translates to signal power getting distributed into adjacent DFT bins.

A way to mitigate this is by applying a weighting function to the data coming into spectrum analyzer (see Figure 2.2) in order to taper the boundaries so that the periodic ex-

[2]Even an LNA with a 150 K = 2.2 dB NF would only reduce the limit on ε by $\sim 12\%$ over the current amplifier choice.

[3]This section is a summary of results found in [113].

tension of a signal is smooth (over as many derivatives as possible). The weighting functions used to do this are called *windows*. A display of the different windows offered by the Rigol RSA5065-TG used in this experiment is given in Figure 2.3.

Windows have many figures of merit, but there are a few that are important to the Dark E-Field Radio experiment, namely the effective noise bandwidth (ENBW), process loss, and frequency resolution. These are described in detail in this section.

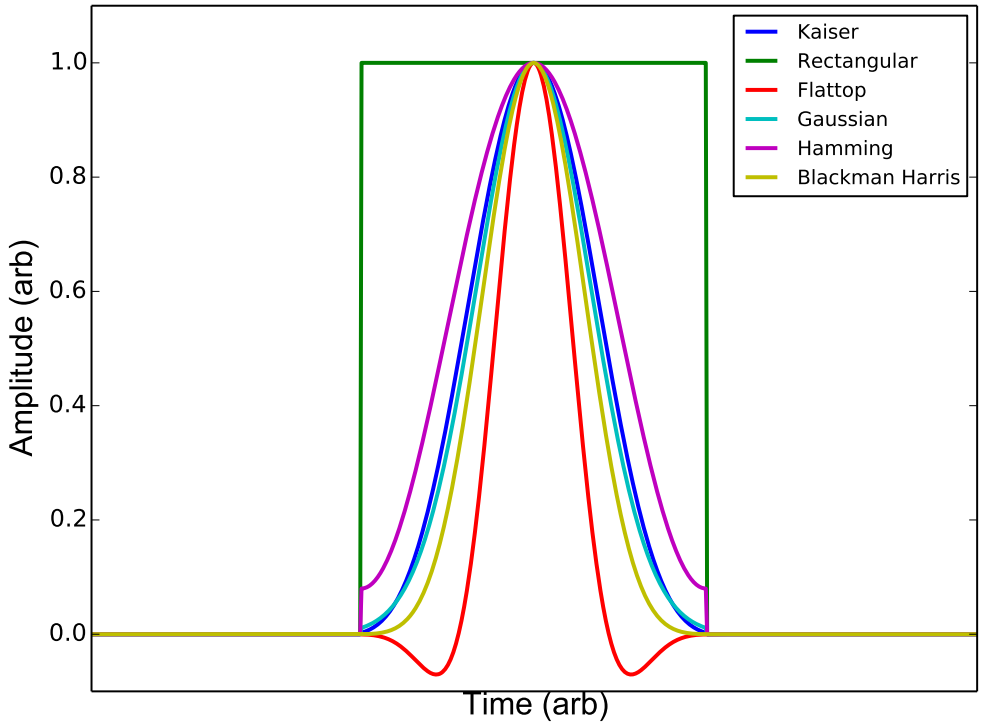

Figure 2.3: Plot of the different windowing functions available on the Rigol RSA5065-TG spectrum analyzer [114] showing the different ways of tapering to zero at the ends.

.

2.2.1 Effective Noise Bandwidth

The ENBW is defined as the ratio of the bandwidth of a rectangular filter to the bandwidth of the chosen window such that the amount of noise power accumulated inside the rectangular filter is the same as the chosen window. Equivalently, for a discrete windowing function $w[n]$ of length N, this is defined as

$$\text{ENBW} = N\frac{\sum_n w^2[n]}{\left(\sum_n w[n]\right)^2}. \tag{2.9}$$

For a rectangular window, the ENBW is identically one. Assuming that the signal is in a single bin, increasing the ENBW reduces the SNR of a candidate signal by increasing the noise floor. An ENBW of 2 bins, decreases the SNR by $10\log_{10}(2) = 3\,\text{dB}$. Since the variation in the noise goes as the quarter root of the number of samples, a decrease of 2 in SNR corresponds to an increase of $2^4 = 16$ in total acquisition time to obtain the same ε. As discussed in Section 2.2.2, this SNR reduction is also called the *power loss*.

2.2.2 Worst Process Loss

Worst case process loss is actually the sum of two separate figures of merit: Power loss and scalloping loss. Power loss is the SNR reduction due to windowing, which is just the ENBW (given in dB). Scalloping loss is the ratio of coherent gain for a signal located a half bin from a DFT sample point over the signal located at a DFT sample point. For a discrete

windowing function $w[n]$ of length N, this is defined as

$$\frac{\left|\sum_n w[n] \exp\left(-j\frac{\pi}{N}n\right)\right|}{\sum_n w[n]}. \tag{2.10}$$

The worst process loss is then the product (sum in log space) of the process and scalloping loss. This represents a reduction in SNR, which is very important for detecting very small signals.

2.2.3 Minimum Resolution Bandwidth

The minimum resolution bandwidth classifies the minimum frequency separation required to identify two equal-strength lines such that at an arbitrary frequency their respective main lobes can be defined.[4] The minimum spacing required to resolve these two peaks is the 6.0 dB bandwidth. For the first run of the experiment, this quantity is important because it defines how many spans are required for the entire spectral range. The RSA-5065-TG spectrum analyzer defines this quantity in terms of a ratio constant that depends on the length of the FFT. For the first run of the experiment, a Kaiser window was chosen based off of [114] page 3-7. Herein, the Kaiser window was listed as having good spectral leakage and amplitude accuracy and moderate frequency resolution. In retrospect, amplitude resolution is not tremendously important since we are not trying to resolve multiple candidates. From Table 2.1, the basic rectangular window is actually the best choice because it has the lowest

[4]The main lobe is frequently defined as the width between zero crossings or as the variance if there are no zero crossings [115, Other Definitions of Main Lobe Width]. See Figure 2.4 for examples of different windows.

Windows and Figures of Merit			
Window	**ENBW (Bins)**	**Worst Process Loss (dB)**	**6.0 dB BW (Bins)**
Gaussian $\alpha = 3.0$	1.64	3.40	2.18
Flat-top	3.82	5.82	5.78
Blackman-Harris	1.61	3.34	2.19
Rectangular	1.00	3.92	1.21
Hamming	1.36	3.10	1.81
Kaiser $\alpha = 2.5$	1.65	3.38	2.20

Table 2.1: Important window parameters taken from [113]. Although specific window parameters are not given in [114], care has been taken to match the numerical order of the 6.0 dB BW and the RBW ratio order as a function of window type. It also appears that the *Hanning* window described in [114] is actually the Hamming window described in [113].

ENBW (thus the lowest baseline) and the best frequency resolution (smallest 6.0 dB bandwidth). These factors mitigate the effect of having a high process loss. Dynamic range is not important since all candidate signals will be very low level so the high side lobe level of the rectangular window is not concerning. A plot of the FFT of the various windows shown in 2.3 is shown in Figure 2.4 visually highlighting the various features discussed. As discussed in Chapter 5, we have developed a real-time FFT system based on the ROACH platform. For the reasons above, and also because it is simple to compute, we are using a rectangular window for this system.

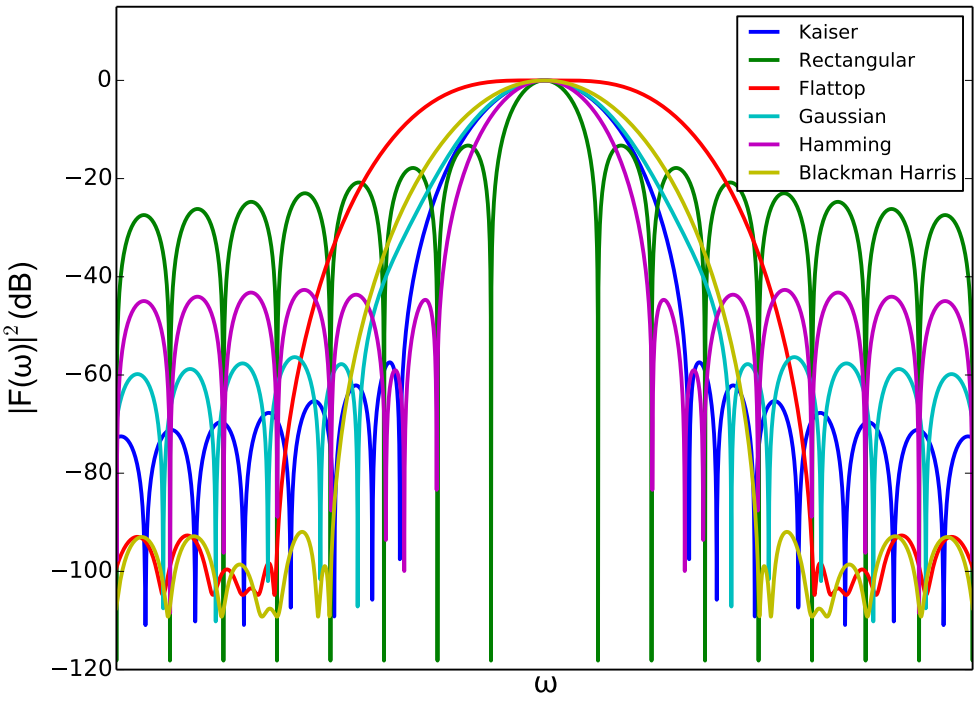

Figure 2.4: Power spectrum of the various window functions in Figure 2.3 showing the different parameters described in Sections 2.2.1, 2.2.2, and 2.2.3. Ultimately, a Kaiser window was used for the first run of the experiment although a rectangular window is a better choice even though it has large side-lobes. The amplitude of the main lobe for all windows has been normalized to 0 dB.

.

2.3 Sensitivity analysis

The direction of a monochromatic E-field from dark photons is unknown. Although we do not save phase, the receiver is sensitive to E-field direction due to the polarization sensitivity of the antenna. For example a dipole has peak sensitivity to an E-field aligned with its axis. We mount the antenna such that it is most sensitive to the east-west component of an E-field, so that if a signal is detected, its amplitude will be modulated on 12-hour periods by

the Earth's rotation [85].

The measurable quantities are the total power, P_T, and the system noise power, $P_{\rm sys}$ (in some bandwidth). The noise power can also be measured by averaging the measured power in nearby frequency bins. The signal power, $P_{\rm sig}$, adds linearly with the noise power and thus can be found by subtracting the noise power from the total power

$$P_{\rm sig} = P_T - P_{\rm sys} = \frac{V_{\rm sig}^2 \,{\rm Re}\{Z\}^2}{\{Z\}} \tag{2.11}$$

where $V_{\rm sig}$ is the measured RMS voltage and Z is the impedance of the antenna. We use a balun to match the impedance of the antenna to the transmission line and therefore ${\rm Re}\{Z\}/|Z|^2 \approx 1/|Z|$. The signal voltage is related to the electric field at the position of the antenna, $\vec{E}_x$ by the *antenna factor*, AF, via

$$AF \equiv \left|\frac{\vec{E}_x}{V_{\rm sig}}\right|. \tag{2.12}$$

The AF is defined as the electric field component coupling to the antenna divided by the corresponding voltage developed at the antenna terminals. AF has units of meters^{-1}.

For example, for an antenna with 50 Ohm termination

$$AF = \frac{9.73}{\lambda G^{\frac{1}{2}}}$$

where λ is the wavelength in meters and G is the antenna numerical gain over isotropic[116].

In free-space, the dark matter energy density is related to the measured electric field via

$$\rho_{\rm DM} = \frac{\epsilon_0}{2\varepsilon^2}\left|\vec{E}'\right|^2 \tag{2.13}$$

where ε is the small kinetic mixing parameter between the dark photon and electromagnetism and ϵ_0 is the permittivity of free-space. From this, the signal power is related to the local dark matter energy density according to

$$P_{\text{sig}} = \frac{2\varepsilon^2}{\epsilon_0 (AF)^2 |Z|} \rho_{\text{DM}}. \tag{2.14}$$

The uncertainty in a noise measurement of a narrow band signal, σ_T, is given by the Dicke radiometer equation [117]

$$\sigma_T \approx \frac{T_{\text{sys}}}{\sqrt{\Delta\nu_{RF}\tau}} \tag{2.15}$$

where T_{sys} is the system noise temperature. The bandwidth, $\Delta\nu_{RF}$, times the integration time, τ, gives the number of trials in the integration. The random uncertainty in the measured power, σ_P, is therefore given by

$$\sigma_P \approx k_B \Delta\nu_{RF} \sigma_T. \tag{2.16}$$

This uncertainty applies to both the measurement of total power and to the measurement of the baseline power. The total power is measured for a single bin, whereas the baseline power is measured using a large number of bins, so the statistical uncertainty in the signal power is approximately given by

$$\sigma_P \approx k_B \sigma_T \approx \frac{k_B T_{\text{sys}}}{\sqrt{\Delta\nu_{RF}\tau}}. \tag{2.17}$$

Figures 2.5 and 2.6 illustrate the predicted behavior of the averaged spectral data and eventual measurement error in the event of a detection of a 10 nV dark matter signal. Figure 2.5 shows the time-evolution of the baseline noise near a detection. As the baseline

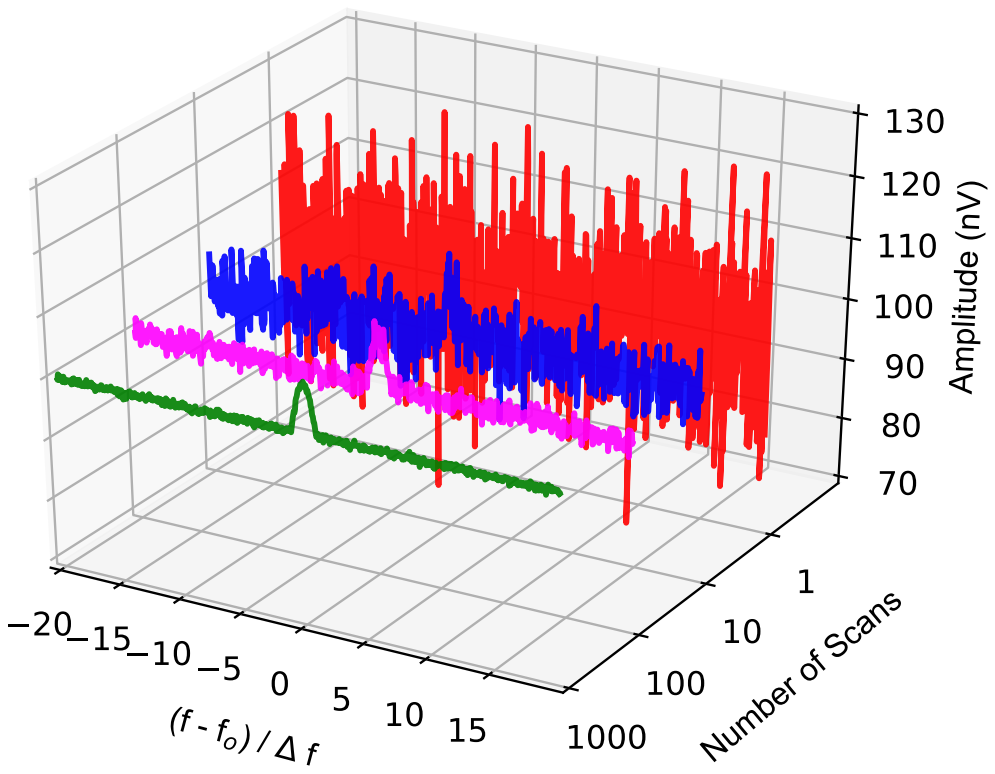

Figure 2.5: SNR dependence on number of scans averaged for a 10nV signal, relative to a 100 nV long-time averaged noise floor, at a frequency of f_0. The red, blue, magenta, and green curves represent the signal after 1, 10, 100, and 1,000 scans, respectively. The width of this signal is assumed to be $\Delta f = f_0/10^6$. Note that even though the average noise level goes down like the square root of time (Equation 2.18), the limit on the scalar coupling constant, ε, goes as the quarter root of time (Equation 2.19).

averages down, the exclusion limit will decrease as (number of scans)$^{1/4}$. As it approaches the 10 nV signal, the additional power from the dark photon field will manifest as a worsened exclusion limit around the central frequency, f_0. Once the 5σ threshold is crossed, the uncertainty on the measurement will decrease as the inverse square root of time.

Figure 2.6 shows the integration time dependence of the 5σ exclusion limit, and of the

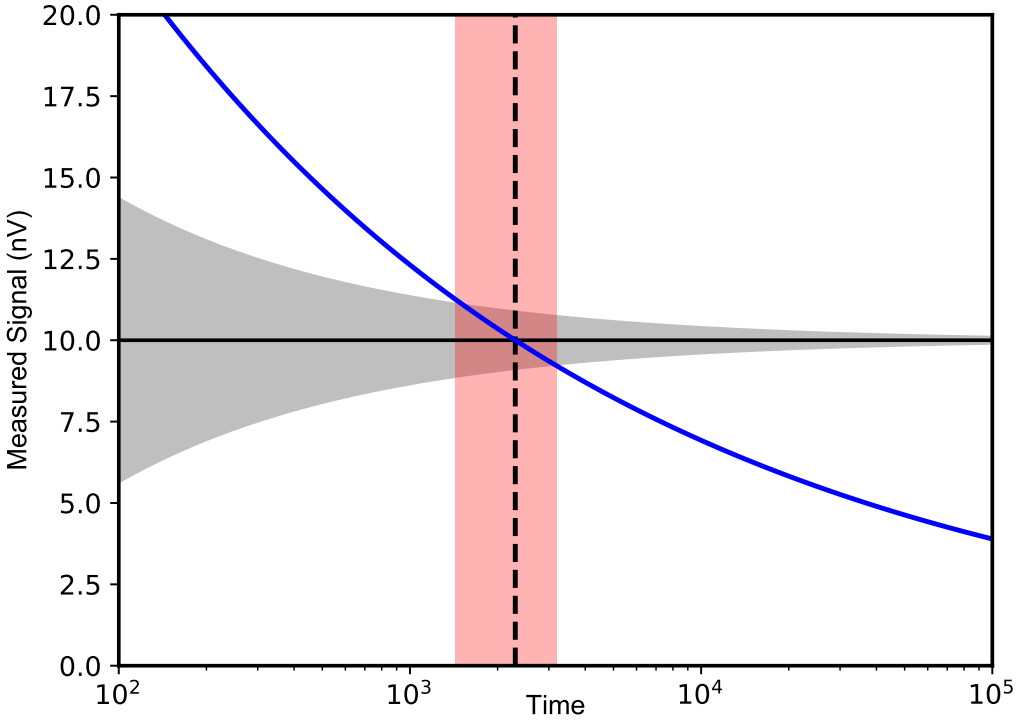

Figure 2.6: Time dependence of a detection. The gray shaded region shows the predicted $\pm 1\sigma$ band of the integrated voltage measurement from a 10 nV signal as a function of time. The solid blue line shows the 3σ exclusion limit as a function of time. The black dashed line and shaded region shows the predicted time until a 3σ detection.

predicted integrated voltage measurement from a 10 nV dark matter signal. The limit curve again decreases like the quarter root of the number of scans, and a discovery will occur when the measurement rises above this line. The exclusion line enters the $\pm 1\sigma$ band of the voltage measurement at 1,428 scans and exits at 3,272 scans. This means that although the expected time until detection of such a signal is 2,304 scans, the actual time will vary by roughly 40 %.

The uncertainty in the coupling constant due to system noise, σ_ε, can be found using

standard error propagation

$$\sigma_\varepsilon^2 = \left[\frac{\partial}{\partial P_{\text{sig}}}\left(\sqrt{\frac{(AF)^2\,|Z|\epsilon_0 P_{\text{sig}}}{2\rho_{\text{DM}}}}\right)\right]^2 \sigma_P^2$$
$$\sigma_\varepsilon = k_B T_{\text{sys}} \sqrt{\frac{(AF)^2\,|Z|\epsilon_0 \Delta\nu_{RF}}{8\rho_{\text{DM}} P_{\text{sig}}\tau}} \tag{2.18}$$

If a positive detection is defined as a signal equal to a constant multiple of the system noise, $\xi \in \mathbb{R}^+$, the limit of detection for a given integration time is given by

$$\frac{\varepsilon}{\sigma_\varepsilon} = \frac{2P_{\text{sig}}}{k_B T_{\text{sys}}}\sqrt{\frac{\tau}{\Delta\nu_{RF}}} \equiv \xi$$
$$\varepsilon\Big|_{\text{SNR}=\xi} = \left(\frac{\Delta\nu}{\tau}\right)^{1/4} \sqrt{\frac{\xi k_B T_{\text{sys}}\,(AF)^2\,|Z|\epsilon_0}{2\rho_{\text{DM}}}} \tag{2.19}$$

Equation (2.18) describes how the uncertainty of a given dark photon signal decreases with integration time, while Equation (2.19) (obtained by substituting Equation 2.14) describes how the limit of detection is improved with integration time. The former scales like the inverse square root of time and can be thought of as an expression of the Central Limit Theorem, while the latter scales as the inverse quarter root of time. For example, in order to reduce the limit of detection measured using an hour of data by a factor of 10, the integration time would have to be increased to about 1 year.

2.4 EM simulation of response

The antenna and the shielded room are sufficiently complex that an analytic derivation of the effective AF is impractical. Using both COMSOL and CST EM software ([118], [119]) we

carried out simulations of the response of the antenna to an E-field in the shielded room. As mentioned above, this response is the AF. For the antenna in a shielded room, the boundary conditions of the conducting walls mean that the AF exceeds the free-space value (antenna response suppressed) at frequencies for which the wavelength is large compared to the size of the shielded room. At frequencies above this cutoff, the AF is quite unlike the free-space AF because of the strong coupling of the antenna to the modes of the shielded room. [120]. The model for the shielded room and antenna is taken from measurements with precision of 0.2 % of the shortest wavelength. An example of the mode structure in the shielded room from a COMSOL simulation is shown in Figure 2.7.

An EM simulation of the AF for the biconical antenna in the shielded room, using CST, is shown in Figure 2.8. This simplified antenna-plus-room model *empty room* allows comparison to analytically derived modes.

2.5 Isolation Testing of RF Shield

External EM signals can mimic candidates and reduce sensitivity. As a result, understanding the isolation of the RF shield is an important part of understanding the system setup. We can get a sense of the isolation requirements we would like via a back of an envelope calculation and then do spot frequency checks to check that we meet those requirements.

Noise inside the shield is dominated by 300K thermal noise, which has a power spectral density of -174 dBm/Hz in the Rayleigh-Jeans region (in the frequency range of interest this

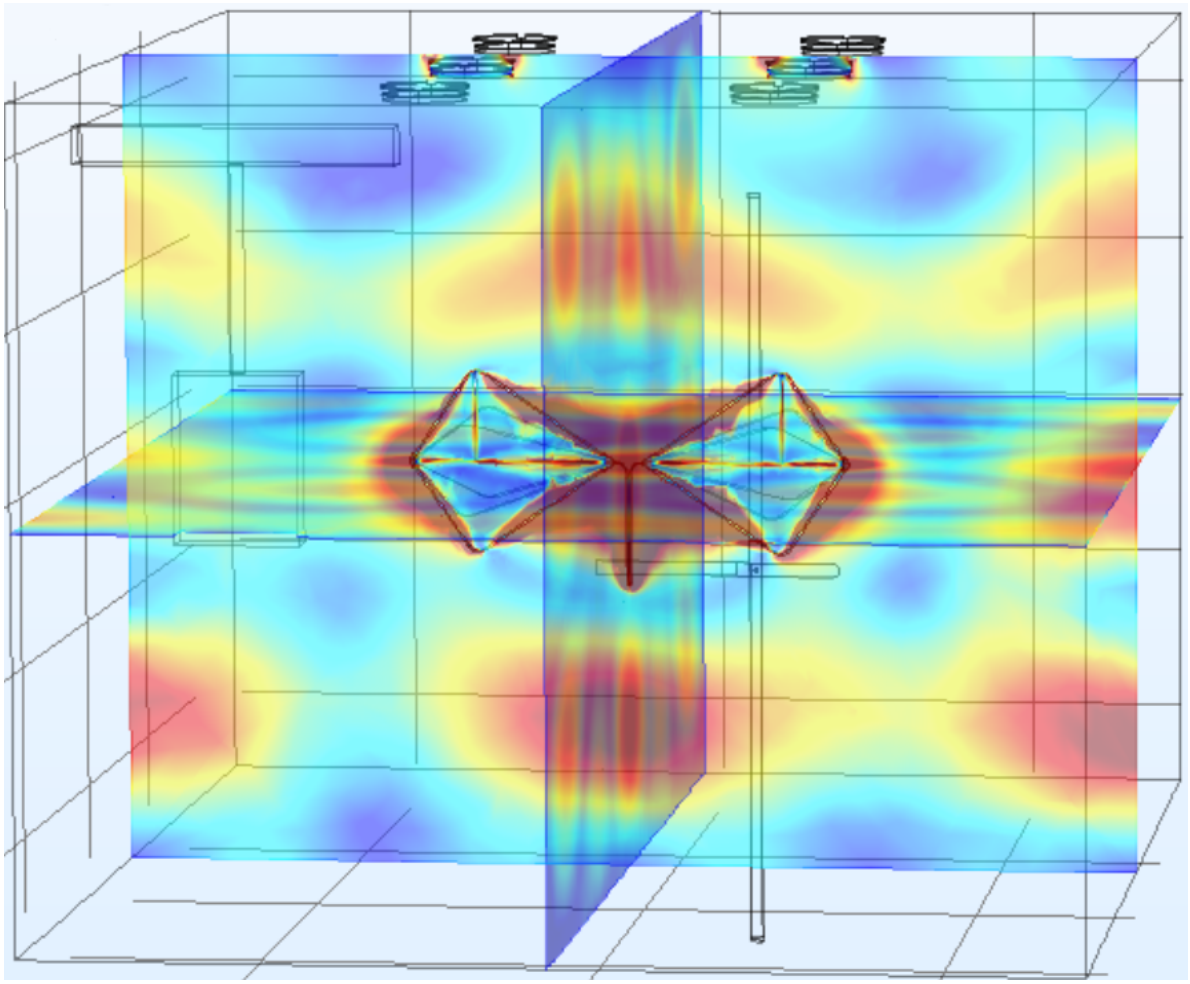

Figure 2.7: COMSOL simulation of the TE035 room mode at 275.9 MHz. The interior of the room with the biconical antenna is shown filled with heat-map slices of the E-field strength. Dark blue corresponds to zero field and dark red to 10^3 V/m.

is a very good approximation since $k_B T = 300\,\mathrm{K} \gg h\nu$ for frequencies $\nu \lesssim 100\,\mathrm{GHz}$). In a 100 Hz bandwidth ($Q \sim 10^6$) into a 50 Ω load, the noise voltage is ∼100 nV. A strong radio station outside the room has a signal strength of 1 V/m. In order for external RF to be less

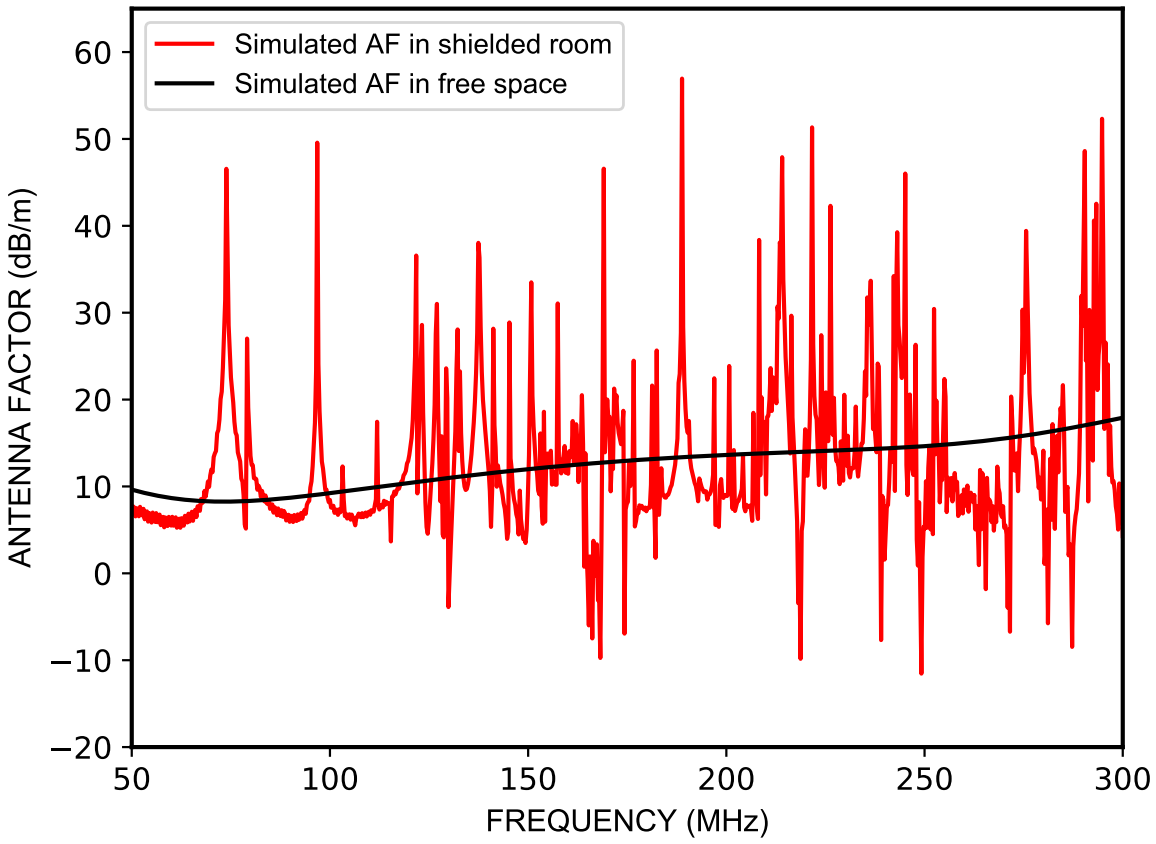

Figure 2.8: CST simulation of the AF of the biconical antenna in the shielded room as a function of frequency with (red). Also shown is the simulation of the free-space AF (black) emphasizing how the room and antenna become a strongly coupled system.

than the thermal noise inside the shield then requires a shielding factor of

$$SF = 20\log_{10}\left(\frac{V_{outside}}{V_{inside}}\right) = 100\text{dB}. \tag{2.20}$$

Thus, the goal is to have >100 dB of isolation in the frequency range of interest.[5] We can test the isolation of the RF shield by either injecting signals of known power or listening at

[5]There is the further complication of averaging that makes us even more sensitive to external RF. Thus this is a lower limit.

frequencies with known interfering signals. Local FM stations are good candidates for this.

In order to do this, a candidate signal is identified. With the door to the RF shield open, data are acquired. Then the door to the RF shield is closed and the process repeated. Because a signal may no longer appear, a lower limit is set by looking at the RMS voltage of the background and calculating a 5σ limit.

An example of this testing is shown in Figure 2.9. KSFM is a 50 kW transmitter located ∼10 miles from the lab transmitting at 102.5 MHz. With the biconical antenna located inside the room with the door open, a $46.4\,\mu V$ signal was measured. Afterwards, the door to the RF shield was closed, the RMS voltage fell to 47.1 pV representing an isolation of

$$\begin{aligned} \mathrm{SF}_{\mathrm{ROOM}} &= 20\log_{10}\frac{4.64 * 10^{4}}{5 * 4.71 * 10^{-2}} \\ &= 106\,\mathrm{dB}. \end{aligned} \tag{2.21}$$

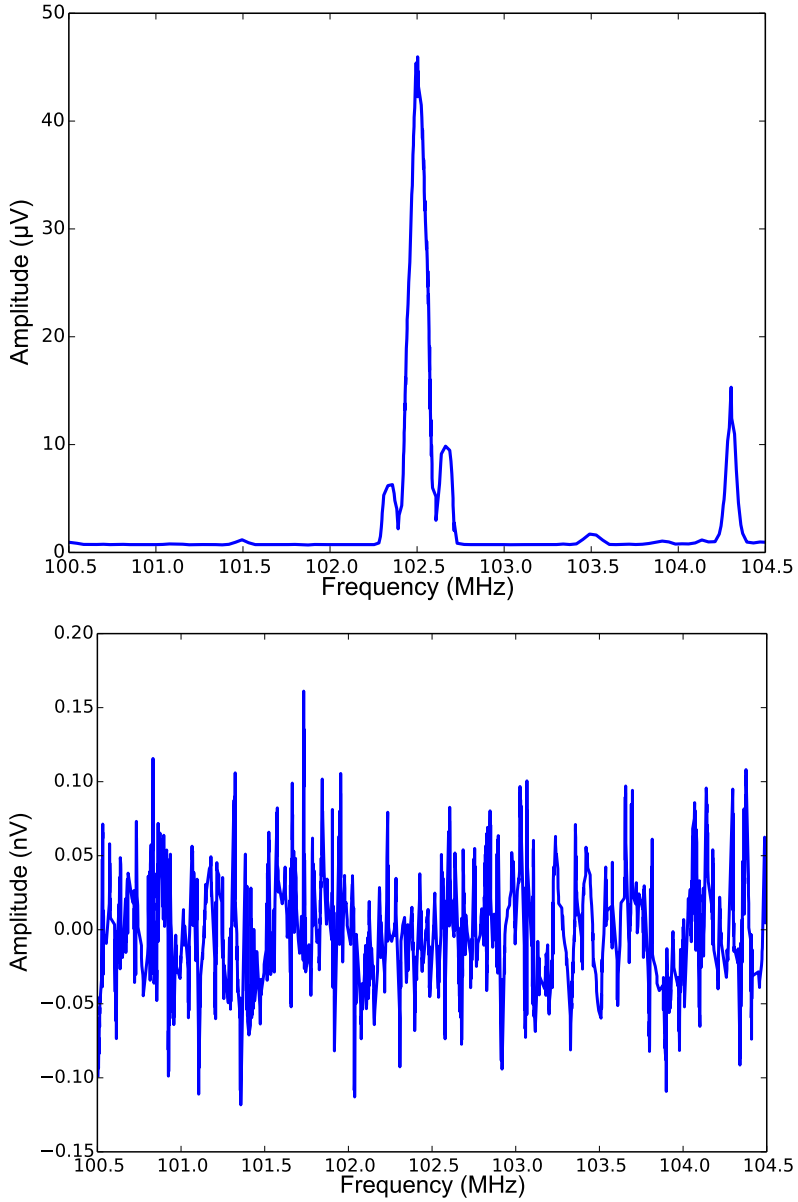

Figure 2.9: (Top) Listening to the KSFM radio station at 102.5 MHz and KXSE at 104.3 MHz. For this test, the biconical antenna was located inside the shielded room and the door was held open. (Bottom) Same span with the door closed.

Figure 2.10 shows the gain corrected amplitude spectral density of the biconical antenna from 50-300 MHz inside the shielded room. The amplitude spectral density of a 50 Ω terminator is also plotted. The expected 0.9 nV/Hz$^{1/2}$ is slightly higher than expected because of amplifier noise. Note that the noise from the terminator is larger than noise from the antenna because the biconical antenna is not perfectly matched to the input of the amplifier. This shows though that the room is successfully shielding external RF down to the level of the thermal noise floor. This is a fundamental limit unless we cool down the shielded room.

2.6 Signal Injection Tests

As a test of the sensitivity of the Phase-I system, we inject a small signal at one frequency and integrate the FFT over a narrow bandwidth. Figure 2.11 shows an example of the resulting spectrum. For this test, we inject a small signal at 70.5 MHz into the shielded room using a small bow-tie antenna. This signal is well below the noise floor of the receiver. A narrow-band sweep from 70.48-70.51 MHz was then performed many times to extract the signal from the noise. Since the span is narrow, we can scan in real-time, performing a nearly 100 % efficient FFT over this frequency range. The result for a 10^6 s integration shows an amplitude of 42 pV (RMS) referred to the input of the preamplifier. Using the standard deviation of the baseline in the narrow-band sweep, and the known AF, a 5σ-limit on the kinetic mixing parameter, ε, of 6.4×10^{-13} between 70.49 and 70.51 MHz can be inferred.

We test the limiting detectable signal versus integration time and find that the peak

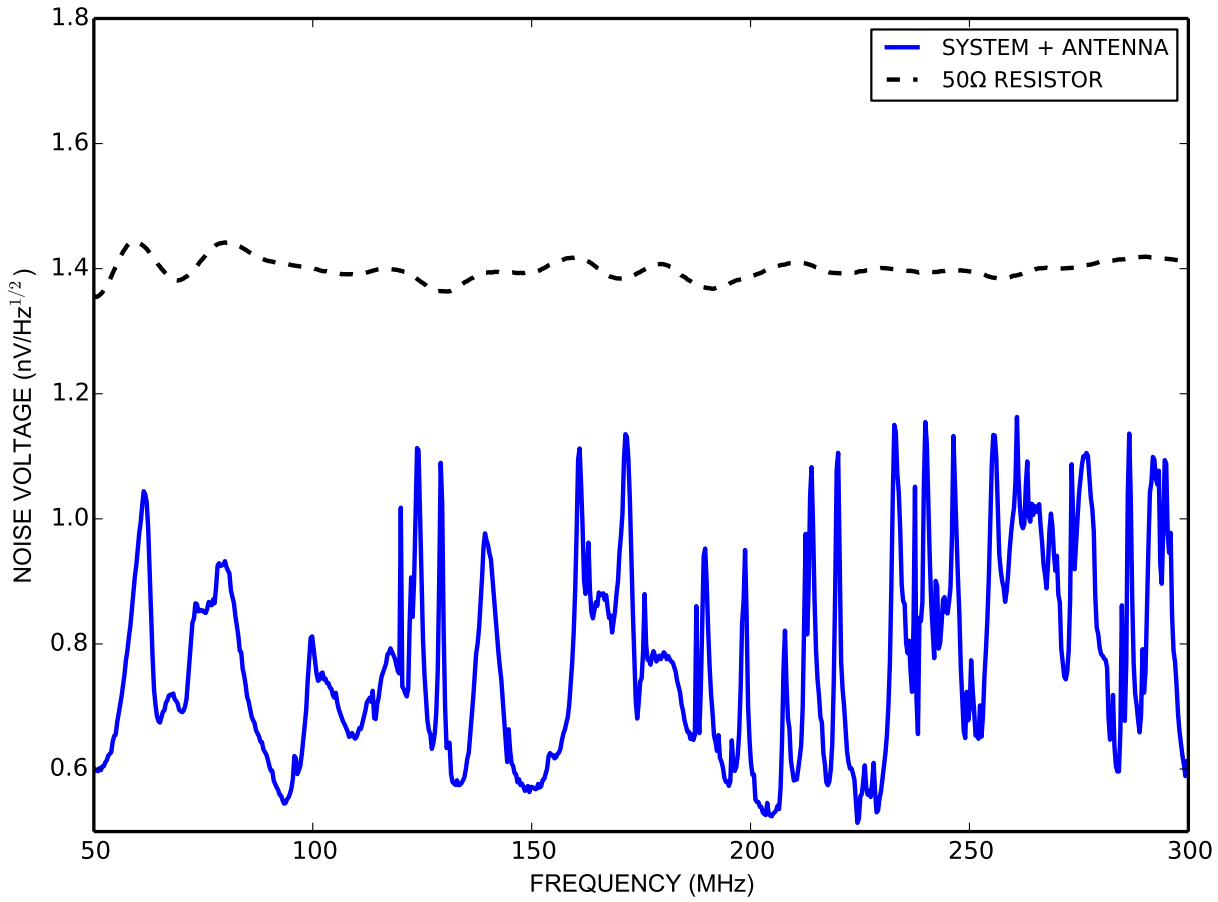

Figure 2.10: Gain corrected amplitude spectral density of the biconical antenna from 50-300 MHz inside the shielded room compared to the thermal noise amplitude spectral density of a 50 Ω terminator. While the expected noise of the terminator is 0.9 nV/Hz$^{1/2}$ the measured value is slightly higher because of amplifier noise. Noise from the terminator is larger than noise from the antenna because of matching. This shows that the room is effectively shielding external RF signals.

detectable power scales inversely as the square root of integration time. As discussed in Section 2.3, the limiting ε then scales as the fourth root of integration time. A study of the average of many scans with a weak injected signal demonstrated that the expected behavior from Equation 2.18 is observed.

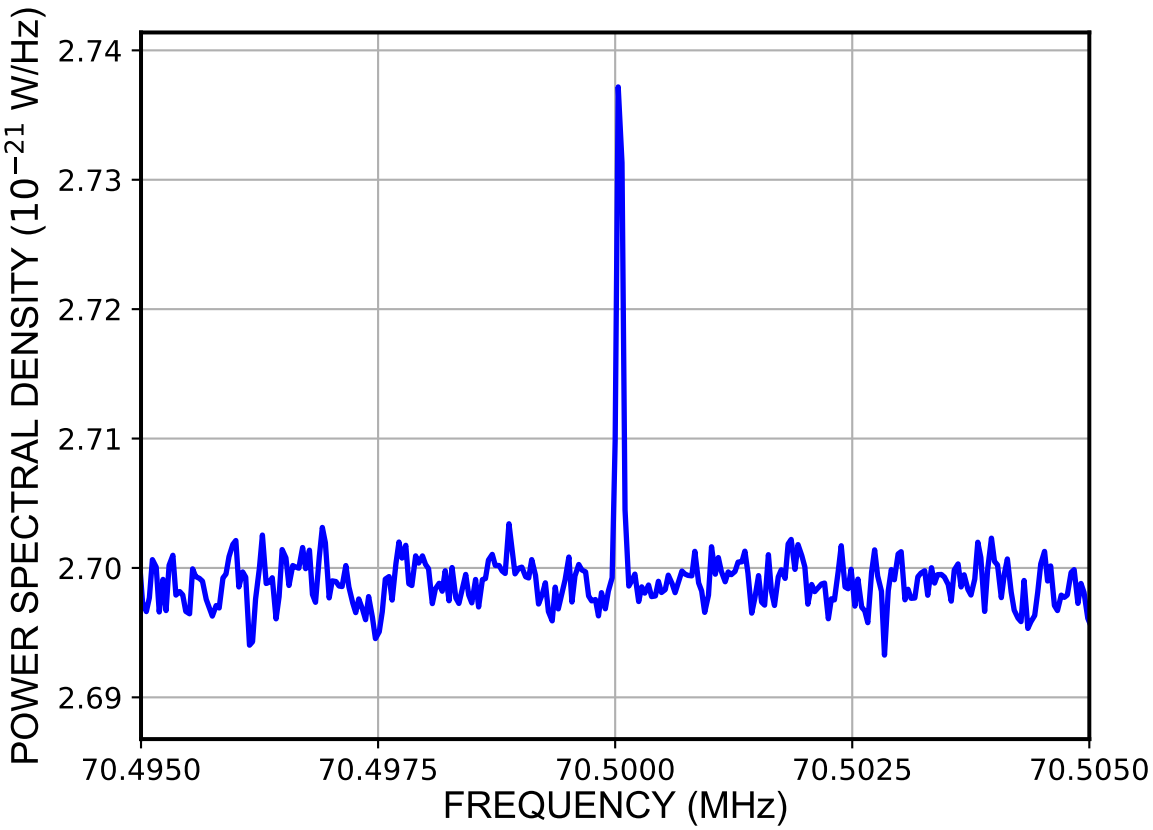

Figure 2.11: Power spectrum showing a 22σ detection at 70.5 MHz after integrating for 10^6 s (frequency span=10 kHz). Total signal power received by the antenna is 3.5 $\times 10^{-23}$ W, which is a factor of 730 below the detection threshold without averaging. This signal injection test demonstrates the sensitivity of the system.

There is a trade-off between channel width (needed to attain high Q), number of spans, and integration time in the search phase versus followup phase for any detected signal. In the search phase, detection of a monochromatic signal buried in noise is the goal. This puts emphasis on integration time-per-Hz. However, because the frequency of the signal is unknown, the maximum range must be covered during the search phase. For example halving

the FFT resolution doubles the spectral efficiency (half the number of required spans) for a given run time. Splitting the spans during data acquisition into sequential time samples enables additional filtering for the expected constant signal.

Once candidate signals are detected above threshold, a run at high efficiency may be made with much higher spectral resolution in spans centered on the candidate frequencies. A surviving candidate may then be validated by demanding a non-detection in the spectrum monitoring system with an antenna outside the shielded room.

Chapter 3

Signal Detection

Defining candidate signals is crucial to the experiment. However, the baseline is not flat and, without an analytic model for it, this makes it difficult to claim signal detection because we do not know how significant a candidate is. However, we do have a couple of handles that we can take advantage of: Dark photons are monochromatic and they are high Q (occupy only a single FFT bin). Using this information, we can develop a high-pass filter to remove unwanted shaping of the baseline of the power spectrum. In so doing, the baseline distribution becomes Gaussian because of the Central Limit Theorem, and defining a signal detection is simplified. The motivation for doing this and an example applied to experimental data are discussed in this chapter.

3.1 Description of the Filter

The issue at hand is that we would like to make significance claims about candidate signals in the spectrum without having a good understanding of the underlying baseline. The dominant noise source is thermal, which we know the probability density function (PDF) of. However, the baseline also includes a combination of effects due to antenna mismatch, room geometry, environmental conditions, etc. Without an analytic model for the PDF of the baseline, making significance claims seems impossible (see Section 3.2 for an averaged power spectrum span from the data run).

However, we do know that the signal is monochromatic and mostly constant in time.With this in mind, we know that any wide structure in the power domain can be ignored. We can use this fact to remove the baseline shaping. The following series of simulations describe this process.

Figure 3.1 shows a simulated time-domain acquisition sampling a Gaussian white noise source. In total, 1024 acquisitions are shown sampling at 600 MHz. This is meant to mimic the pilot data where the maximum frequency in any span was 300 MHz and the number of frequency bins was 800.

To show that these data are normally distributed, the data in Figure 3.1 are put into a histogram in Figure 3.2. Since these samples are drawn from a known Gaussian-distributed parent distribution, this is simply a consistency check.

Now we compute the magnitude-squared of the FFT (length 2^{10} for this example) to get

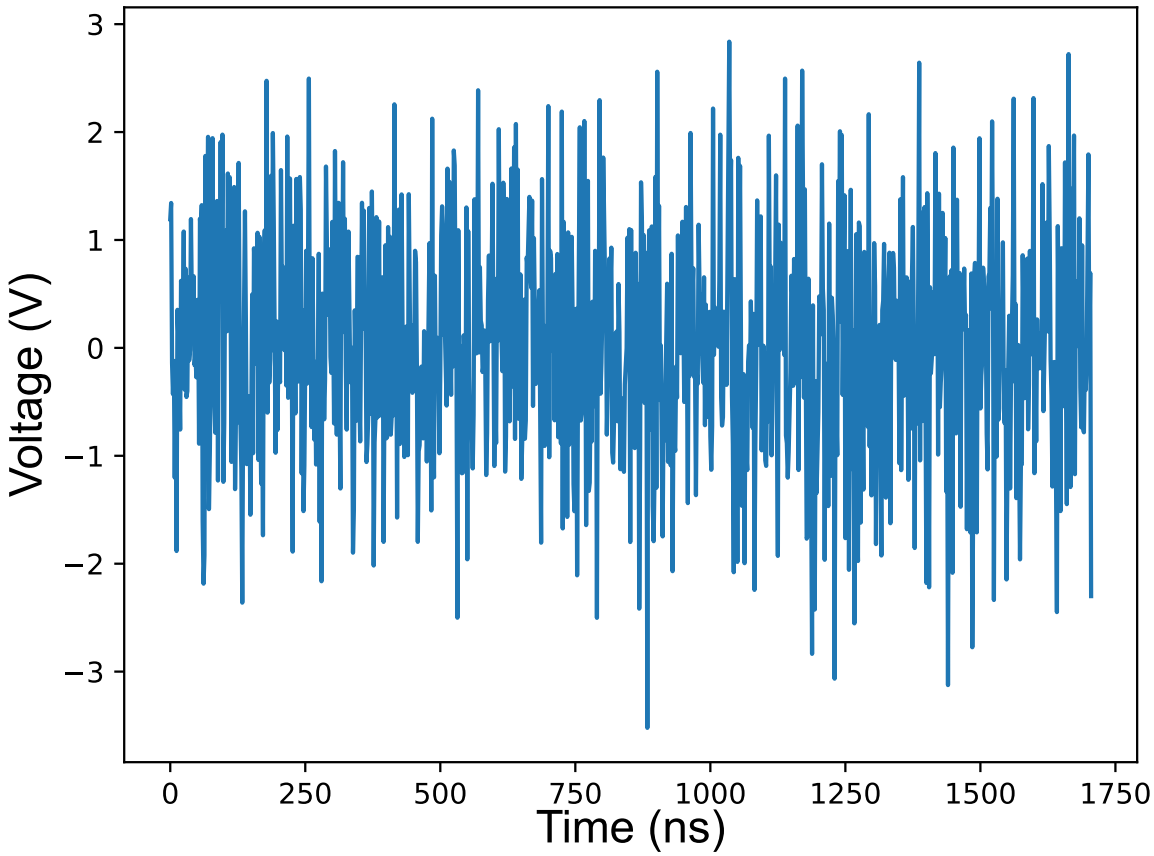

Figure 3.1: Simulated acquisition in the time domain. Data are assumed to be white and Gaussian. The sampling rate is set at 600 MHz and there are 1024 time samples shown.

the FFT power spectrum. In order to normalize the FFT, the following factors need to be included:

- A factor of two to account for the signal only containing real frequencies.
- Division by a factor (FFT length)^2. One power is needed by Parseval's theorem [121]. The other is a normalization factor, which is a byproduct of not including a normal-

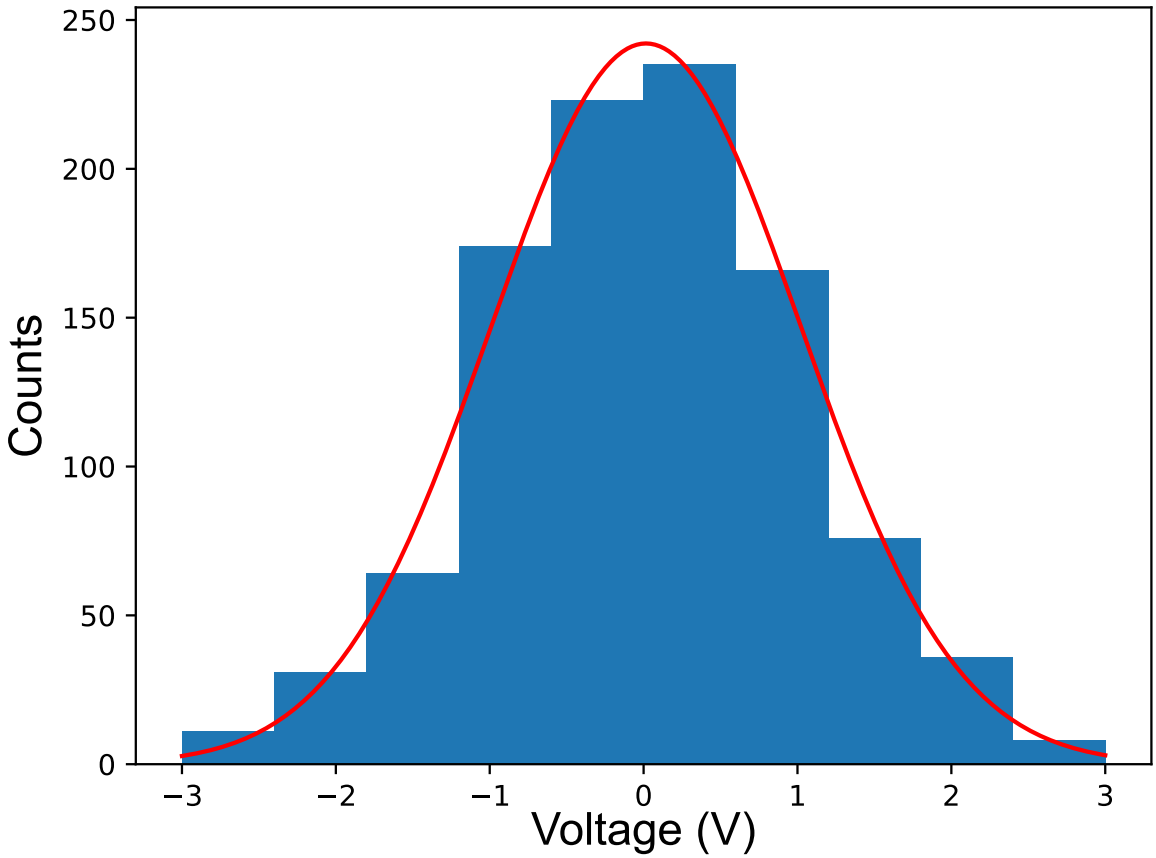

Figure 3.2: Histogram of the simulated data in Figure 3.1. A Gaussian is fit to the data and a simple χ^2-test done. For the data shown here, the p-value is 0.36, which is consistent with the null hypothesis that the data are normally distributed (at least the null hypothesis cannot be rejected at the standard $p < 0.05$ level).

ization factor when computing the FFT.

- A factor of 1000/50 to convert Volts^2 to mW.

The frequency separation, $\Delta\nu$ has been set such that

$$\Delta\nu = \frac{\text{clock rate}}{\text{FFT length}} \tag{3.1}$$

where the clock rate has been set at 600 MHz, implying that the highest frequency that can be resolved is 300 MHz (Nyquist-Shannon sampling theorem [121]).

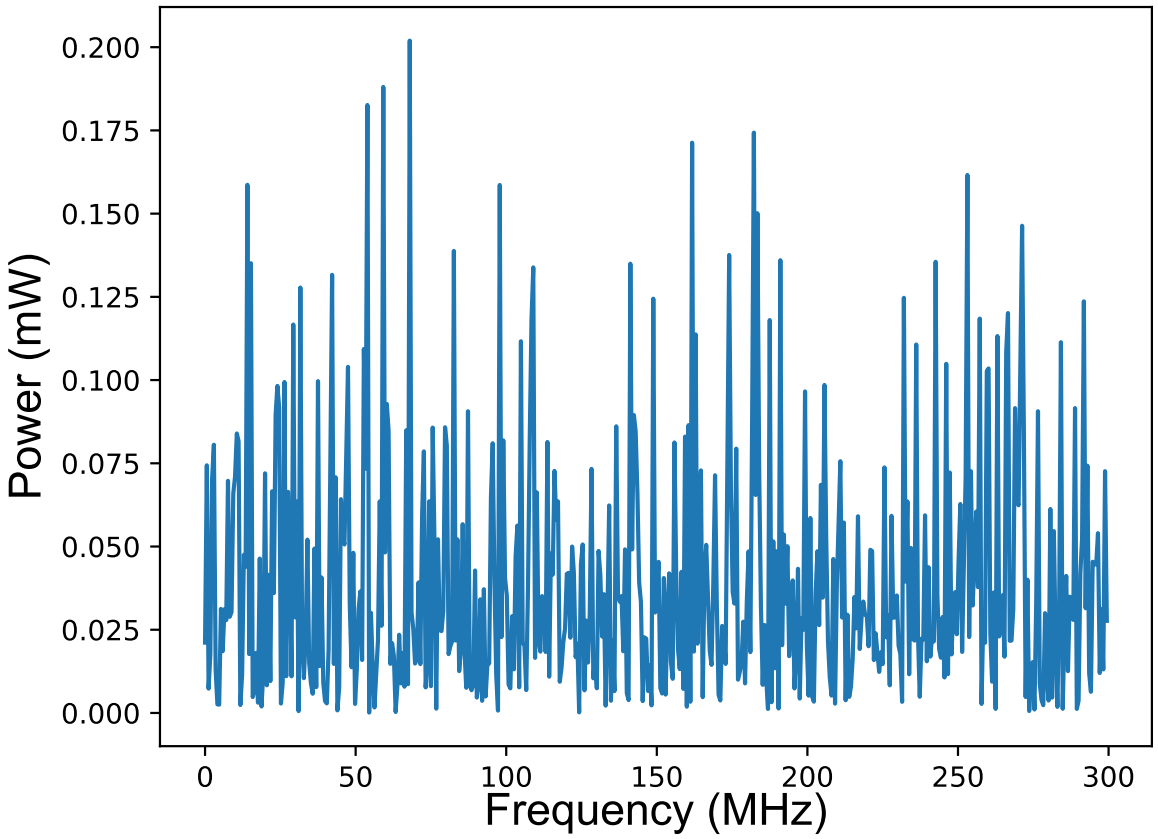

Figure 3.3: Power spectrum of data shown in Figure 3.1 after doing a 2^{10}-point FFT and converting units.

This simulated power spectrum is different from real data because in experimental data, we see shaping in the power spectrum. To model this, a constant factor, which is a sum of two sinusoids and a damped exponential is added to the power spectrum of the Gaussian-distributed noise. There is no analytic model to motivate this form. It is given here only as an

example of the process. See Section 3.2 for an example of baseline shaping the experimental data. The shaping signal is shown in Figure 3.4.

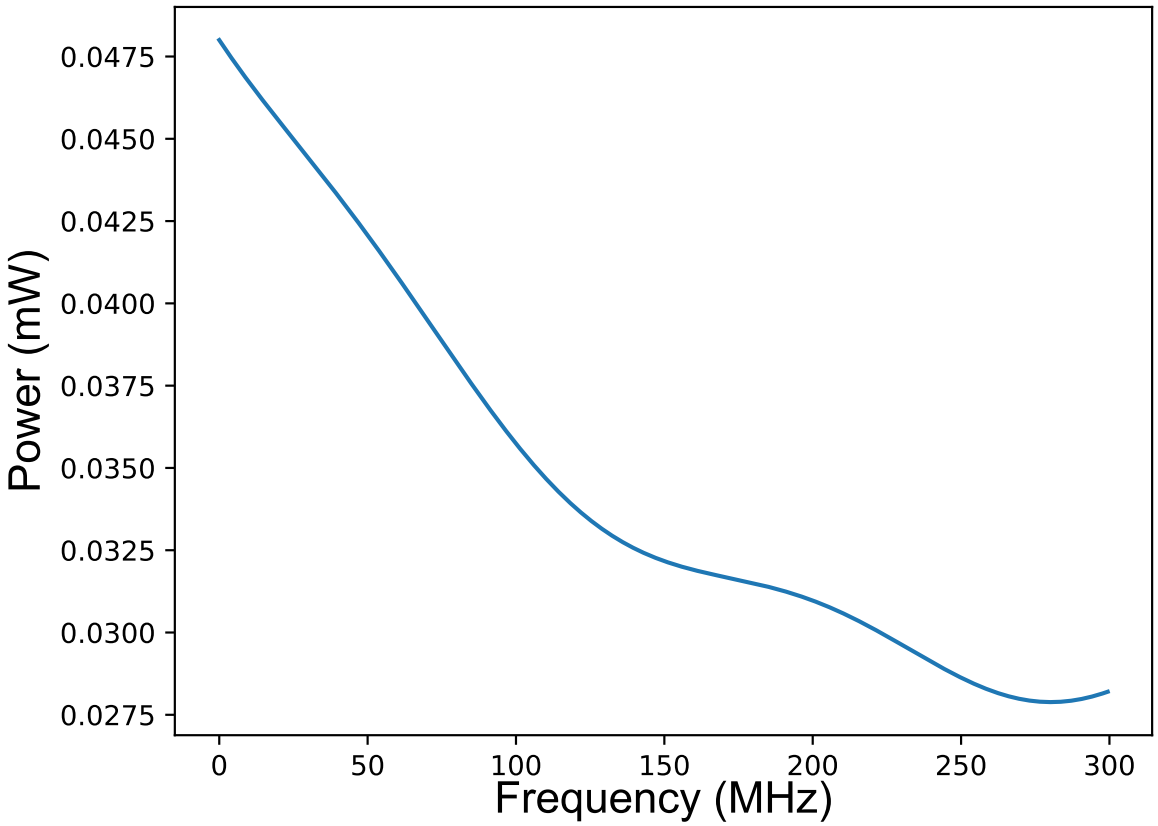

Figure 3.4: Constant shaping spectrum added pointwise to the power spectrum. While this form is only a model, it sufficiently shapes the baseline to make the thrust of the argument clear.

The shaping spectrum in Figure 3.4 is added pointwise to the spectrum in Figure 3.3 to produce a simulated power spectrum with shaping in Figure 3.5.

The question now becomes: How do we deal with a power spectrum (magnitude-squared FFT spectrum) that has baseline shaping in it? As noted, we only care about the components

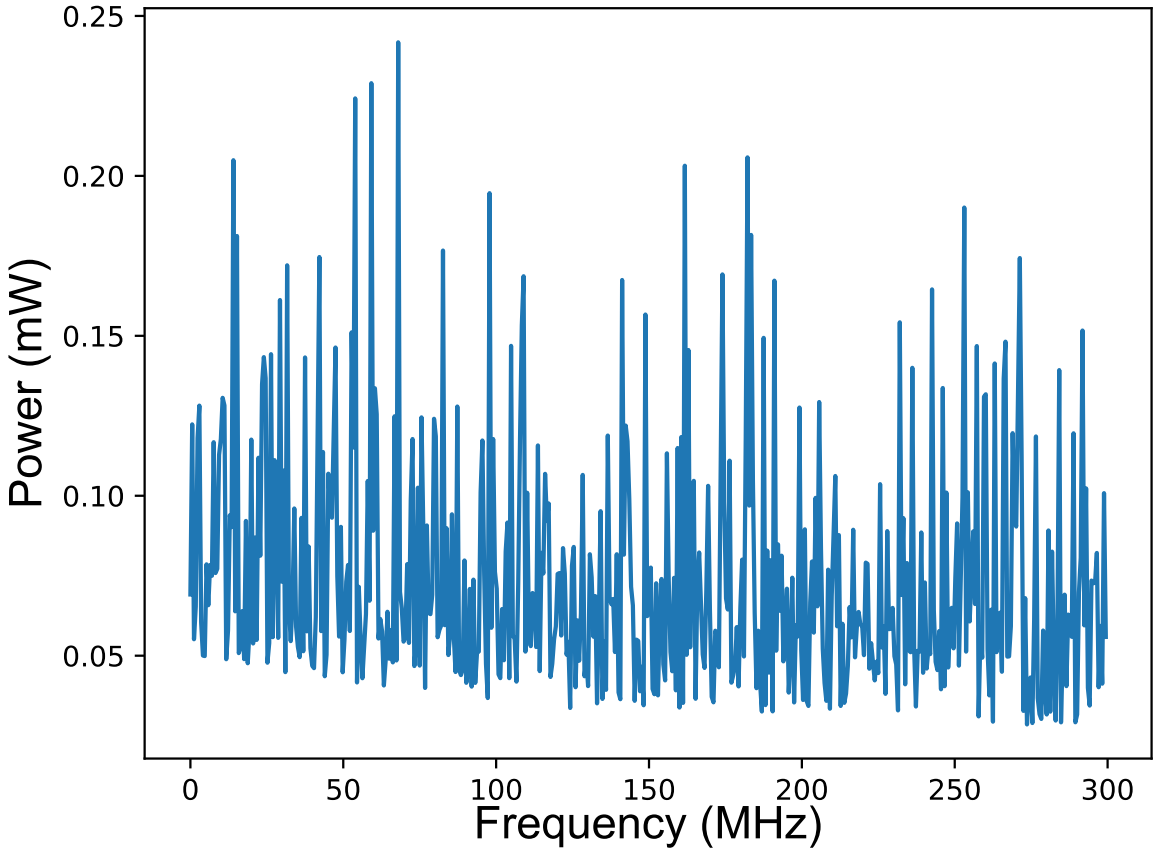

Figure 3.5: Power spectrum of data shown in Figure 3.3 after including baseline shaping.

.

in the waveform that are narrow and do not care about any wide undulations. If we were in the time domain, the natural conclusion would be to high-pass filter. We can do the same thing here. Now, however, the filter is acting on the spectral components of the magnitude-squared spectrum.

Candidate signals occupy only a single spectral bin. In power spectrum space this is the equivalent of saying that candidate signals are high frequency. However, we can make the

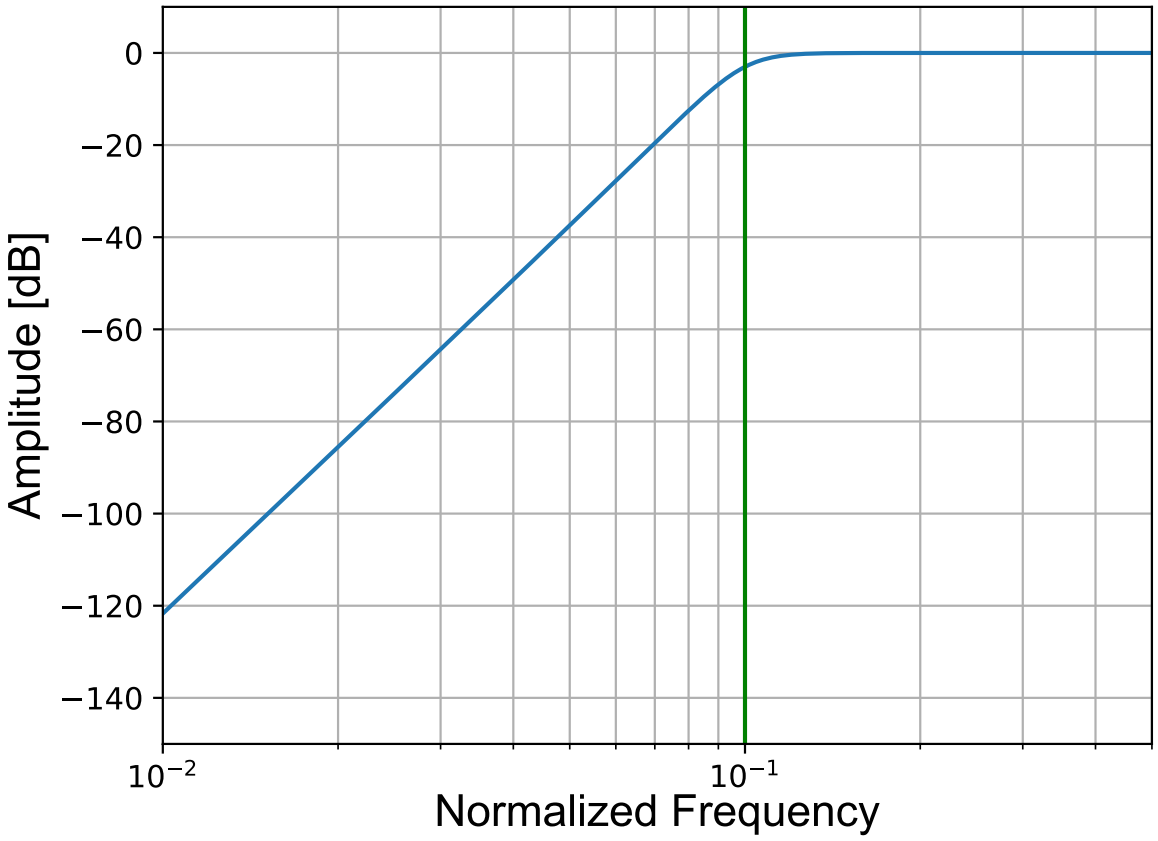

Figure 3.6: Sixth-order high-pass Butterworth filter with a normalized cutoff frequency of 1/10 indicated by the vertical green line.

corner frequency of the high-pass filter considerably lower frequency than that to minimize the chance that we attenuate candidates. We can also minimize this attenuation by choosing a filter that is maximally flat in the passband. This was the motivation for choosing a Butterworth filter. For this example, the cutoff frequency is 1/20 the span. The cutoff frequency is given in frequency units normalized by the sampling rate. To find the cutoff

frequency in these units given a cutoff in bins

$$f_{\text{cutoff}} = \frac{1}{\text{bins}}. \tag{3.2}$$

(Note that bins is really just a normalized time). Equation 3.2 abstracts the magnitude-squared spectrum to a sampled waveform in which the Nyquist frequency is 1/2. We have now designed a digital filter to remove the baseline shaping that we can apply to the magnitude-squared spectrum in Figure 3.5. We then histogram the results after filtering and show the result in Figure 3.7. Note that technically the units are still watts, but they have lost some meaning now that we have applied a filter. The negative values are a result of removing the DC component of the magnitude-squared spectrum. This is okay though because we are ultimately concerned with the size of the fluctuations on the baseline (namely the standard deviation), not the value of the baseline itself.

Interestingly, from Figure 3.7 we see that the resulting distribution is not Gaussian. However, this is not a true simulation of the experiment. We actually average many power spectra together before we apply the filter. This means that we can take advantage of the Central Limit Theorem, which says that even if the underlying distribution is not Gaussian distributed, an independent randomized sum of many of these spectra should approach a Gaussian distribution [122].

To test this, we repeat the same process as before. However, we now average together 10^5 magnitude-squared spectra that are generated in the same way as in Figure 3.1. Note too, that for this simulation, we have assumed that the shaping is independent of the voltage

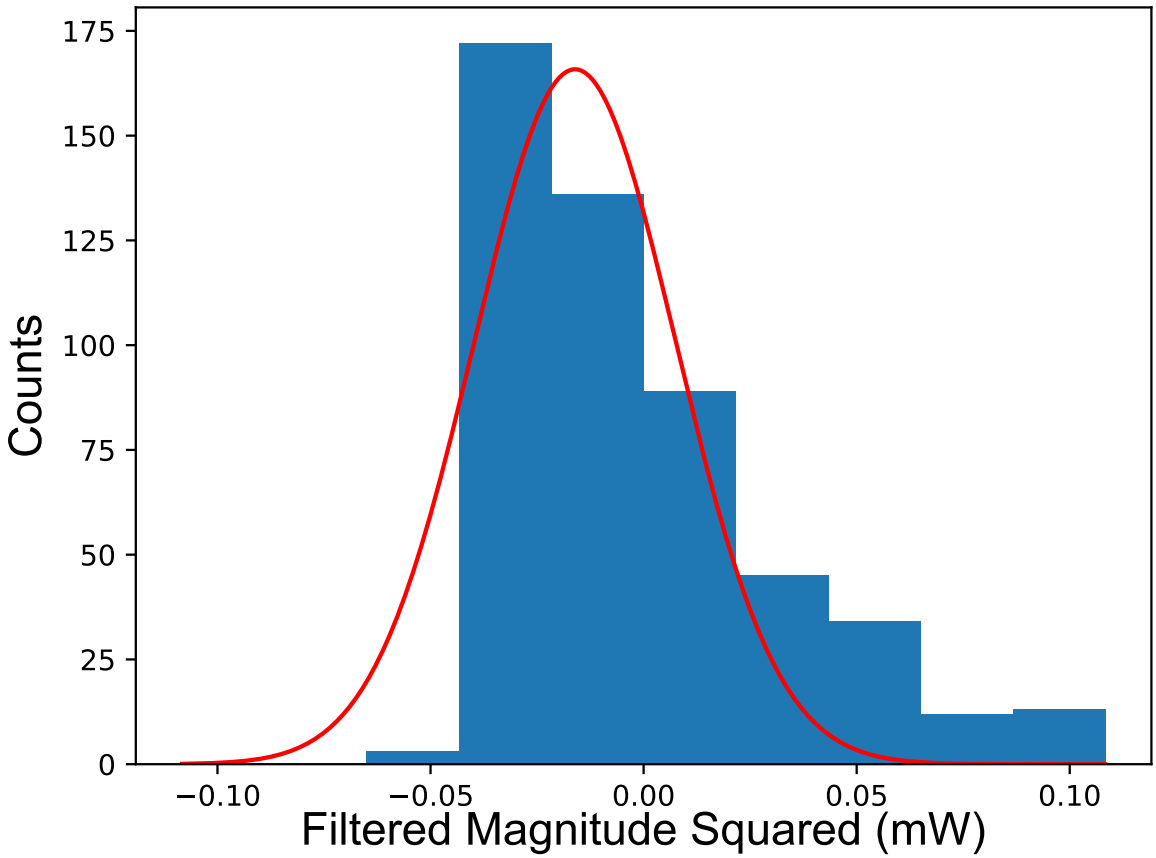

Figure 3.7: Histogram of the magnitude-squared spectrum after applying the filter in Figure 3.6 to the data in Figure 3.5. A Gaussian was fit to these data and a χ^2-test was run, which gave a p-value of 0. This means that we reject the null hypothesis that these data are Gaussian distributed.

signal (the power in Figure 3.4 is added to each power spectrum). The resulting averaged power spectrum is shown in Figure 3.8.

Herein, the shaping due to the addition of the baseline shaping spectrum in Figure 3.8 is apparent. We can now apply the filter in Figure 3.6, as we did for a single acquisition, to these data. Note that the DC bin in the power spectrum has been removed before doing the

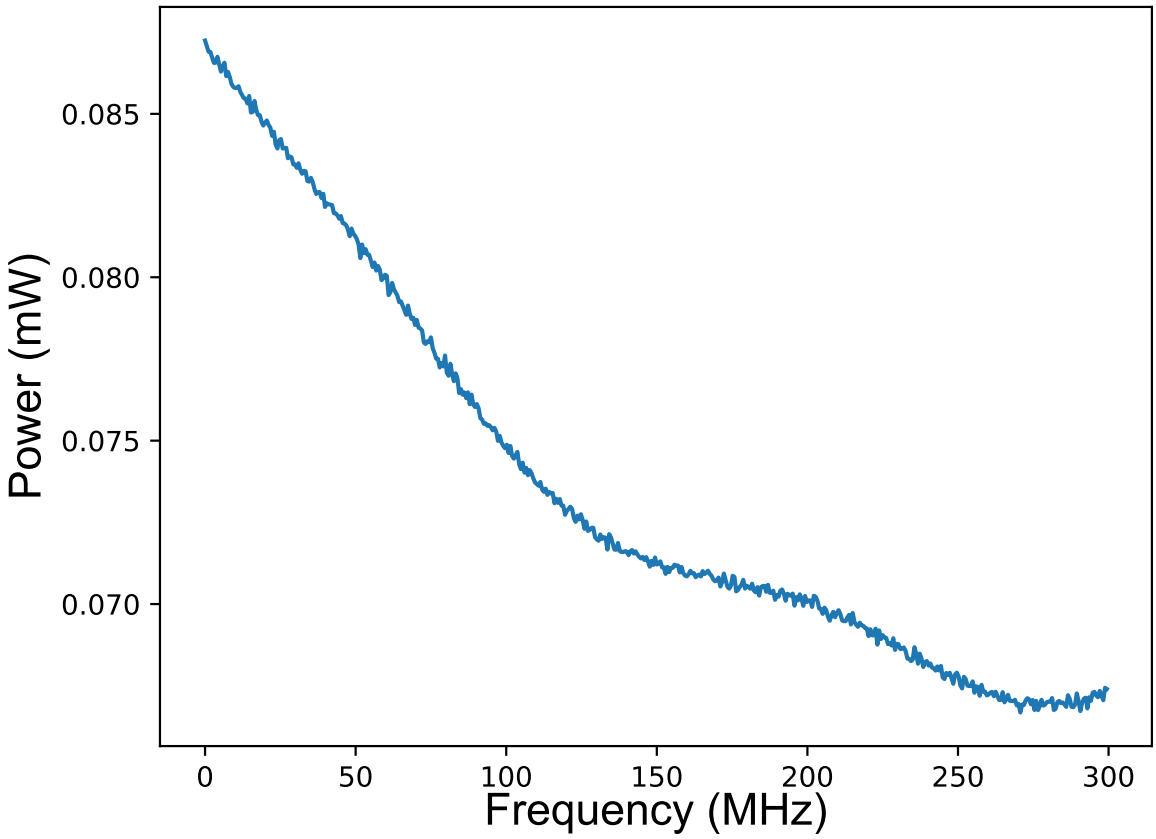

Figure 3.8: Averaged power spectrum after taking and averaging 10^5 acquisitions with shaping like that shown in Figure 3.5.

filtering. This is because the DC bin is notoriously much larger than the rest of the spectral components. When the filter passes over a sharp transition, there are ringing artifacts that heavily skew the fitted Gaussian in the histogram even though the order of the filter was set such that this effect was reduced.[1]

Applying the filter, removes the low frequency shaping of the averaged magnitude-squared

[1]Removing the first bin was done for the run as well. To mitigate the effect of missing frequencies, spans were slightly overlapped.

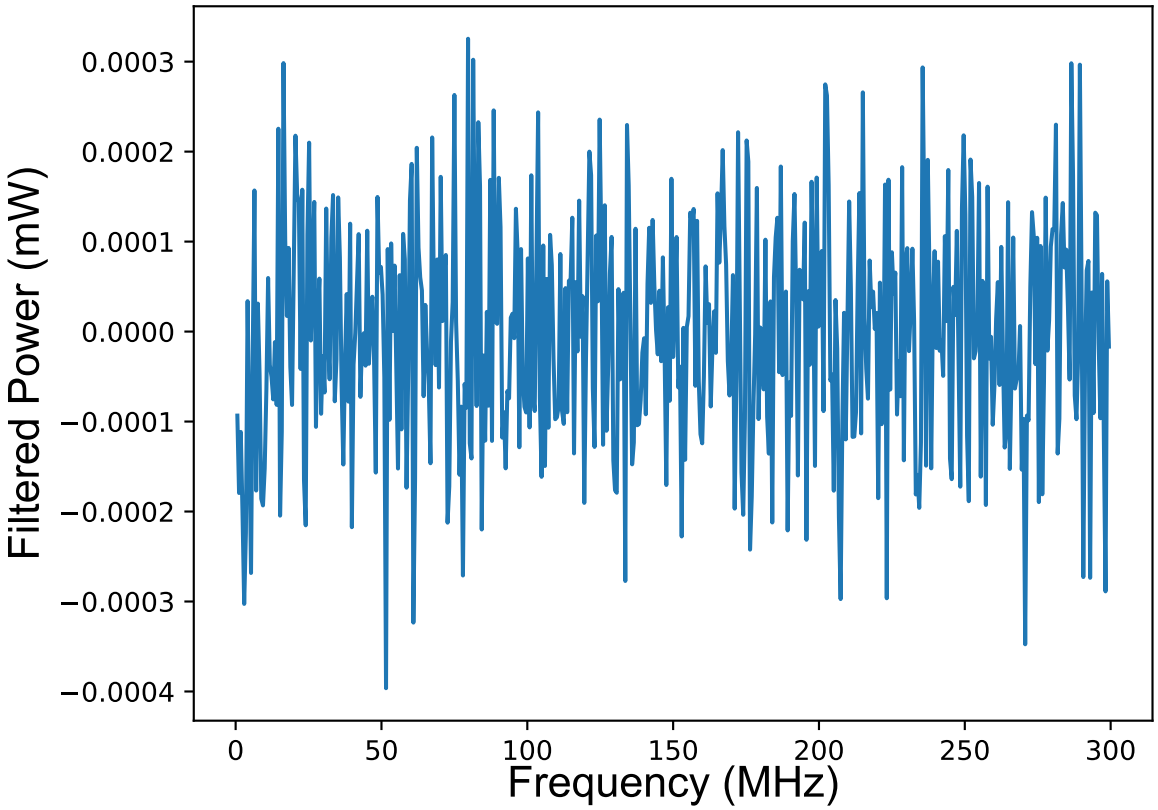

Figure 3.9: Power spectra after averaging together 10^5 acquisitions and filtering through the filter shown in Figure 3.6. Note that the DC bin has been removed to prevent ringing artifacts in the first couple of bins.

spectrum. Furthermore, when the data from Figure 3.9 are put into a histogram, we get the result shown in Figure 3.10. Even though each magnitude-squared spectrum is not Gaussian-distributed, by averaging many such spectra together and then filtering, we have a distribution which does not reject that the null hypothesis that these data are Gaussian distributed.

We can now identify candidates by looking for signals that are more than a certain

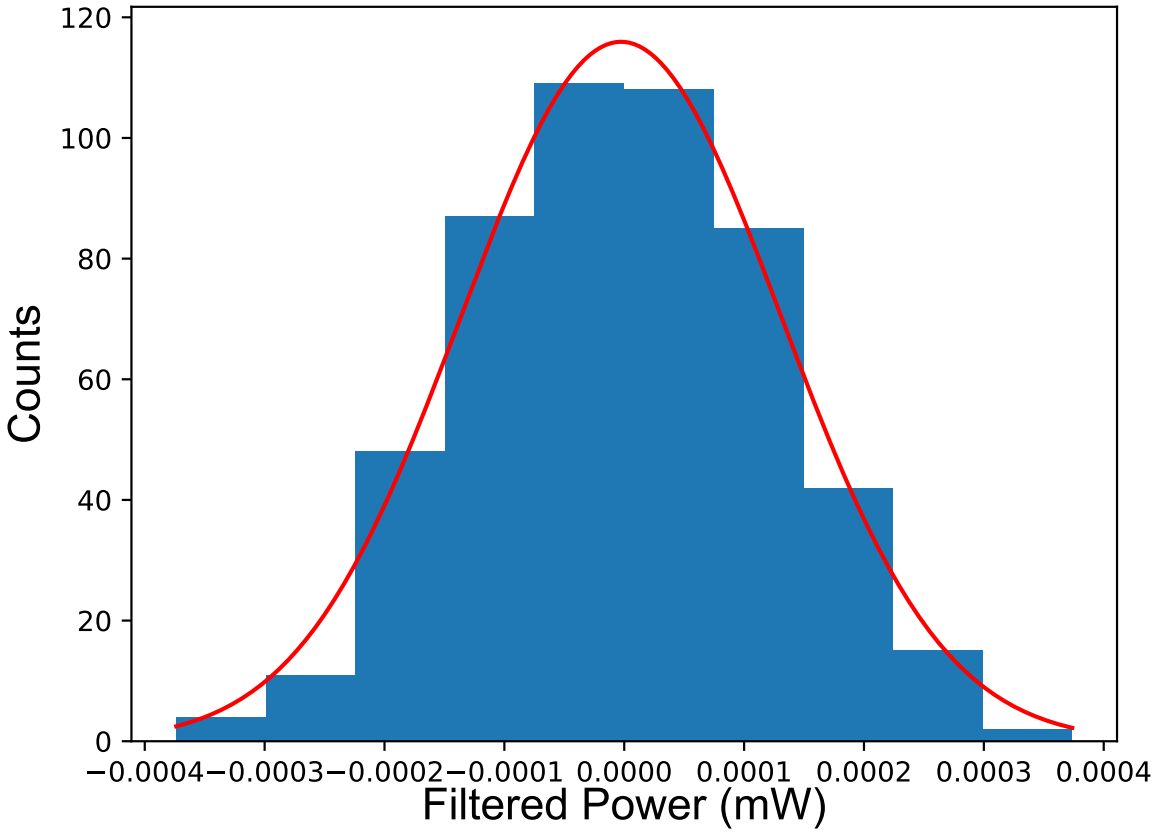

Figure 3.10: Histogram of the data shown in Figure 3.9. A Gaussian has been fit to the data and a simple χ^2-test run giving a p-value of 0.80. This is consistent with the null hypothesis that the data are normally distributed.

number of standard deviations above the mean. For the experiment, we set this number at 5 standard deviations (5σ). At this significance level, we expect to see 1/10 event. For the data run we were able to exclude all events that were greater than 5σ as candidates of interest.[2]

For the data run, each spectrum had 800 points, and, in total, ∼13,600 s of data acquired

[2]This actually defines the 90% confidence interval.

for each span (approximately 1.36×10^5 total averages per span). For data taken with the new, ROACH-2-based data acquisition system, we can take many more averages (1.54 million averages per day) and the number of data points in each spectrum are also much larger (2^{24}). This technique works well when the Q of the baseline shaping is much less than the Q of candidate signals. Since candidate signals are only a single bin wide, this is always the case.

3.2 Filtering Experimental Data

As an example of the filtering technique developed in Section 3.1, we examine a single, averaged power-spectrum span from the experimental data. The spectrum is shown in Figure 3.11. This span has both baseline shaping and a candidate signal at 60.0 MHz, which was ultimately identified as spurious by performing a scan with the input to the spectrum analyzer terminated. Correlated behavior across multiple frequency bins is not a dark photon feature and can be filtered out. As already described, the filter is acting on the averaged, magnitude-squared FFT spectrum with the goal of removing features that exist over many bins.

For the data run, we set the cutoff frequency at 1/10 the span (or 80 bins in power spectrum space) to push the stop-band sufficiently far away so as to minimize the risk of filtering signals and also to reduce ringing effects from large signals with sharp cutoffs. The order was set to 6 to balance a sharp fall-off in the stop-band while minimizing ringing. This can be converted to a normalized frequency in the power spectrum via

$$f_c = \frac{1}{n_b} \tag{3.3}$$

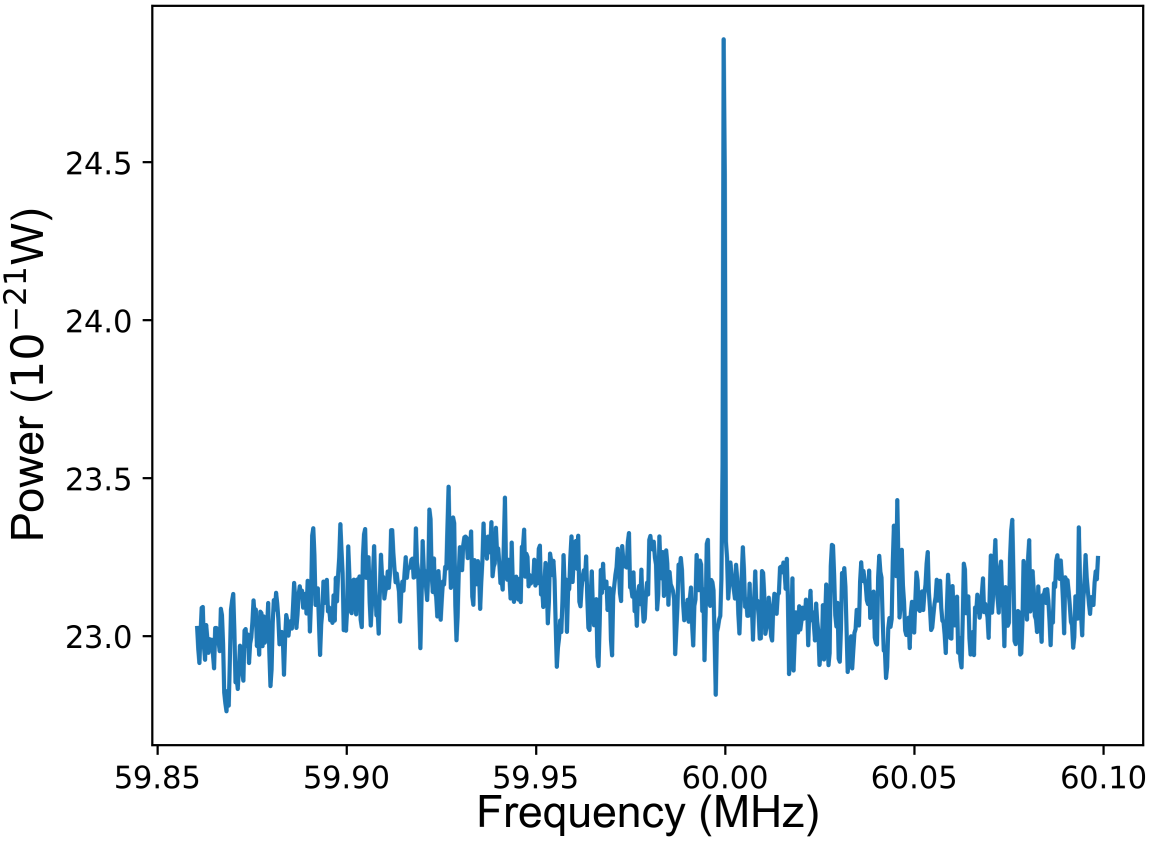

Figure 3.11: Single span from experimental data showing averaged data between 59.860 and 60.099 MHz. Baseline shaping and a candidate signal at 60.0 MHz are evident. This candidate was later identified as spurious.

where n_b is the width of features in the power spectrum. As an example, for a cutoff width of 80 bins, the normalized cutoff frequency, f_c is 1/40. In this scheme, the Nyquist frequency is two bins wide. The frequency response of a Butterworth filter with a normalized cutoff of 1/80 is shown in Figure 3.12. Importantly, for bin widths of 10 or less (normalized frequency of 0.1), the attenuation is less than 42 fdB, which highlights how this filter is not significantly attenuating candidates of interest. Applying a filter with a normalized cutoff of 1/80 (80

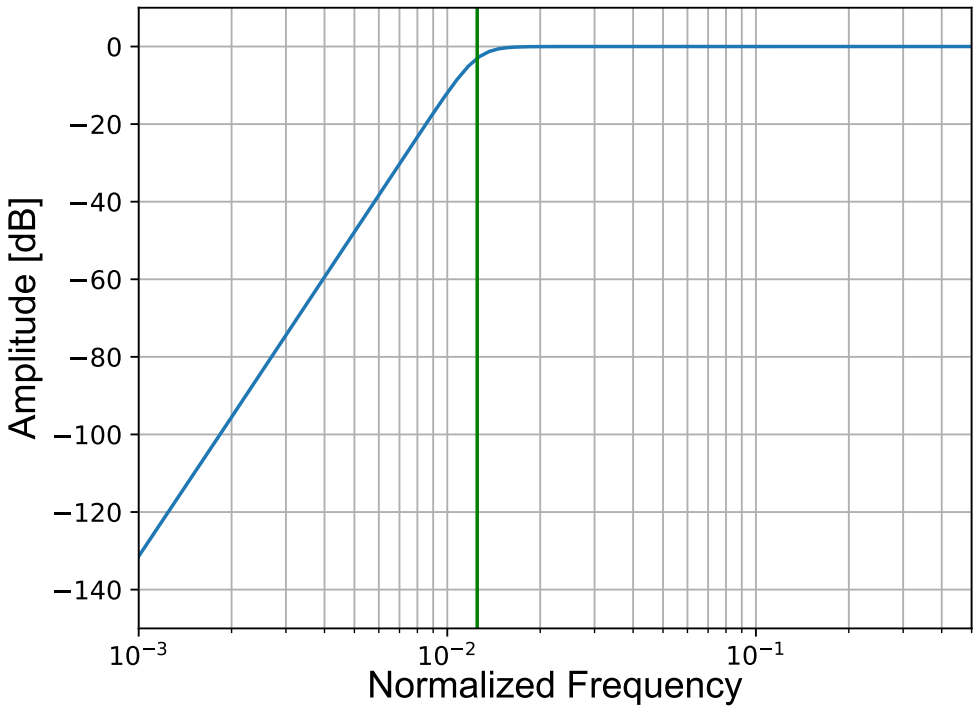

Figure 3.12: High-pass Butterworth filter with an 80 bin cutoff (1/10 the number of bins in a span), indicated with a vertical green line, showing that high frequency signals are not attenuated at a normalized frequency of 1/80. A normalized frequency of 0.5 corresponds to a width of 2 bins (Nyquist limit).

bins) to Figure 3.11 produces the output in 3.13. There are some ringing artifacts because of the size of the candidate signal, however the effect is slight. Importantly, the power of the candidate signal has not been significantly diminished while baseline shaping has been greatly reduced.

As described in Section 3.1, a further benefit of filtering is that it restores the Gaussian behavior of the power distribution (Figure 3.14). Since the baseline is mostly thermal, we expect that the baseline distribution will be Gaussian-distributed. This allows us to set a

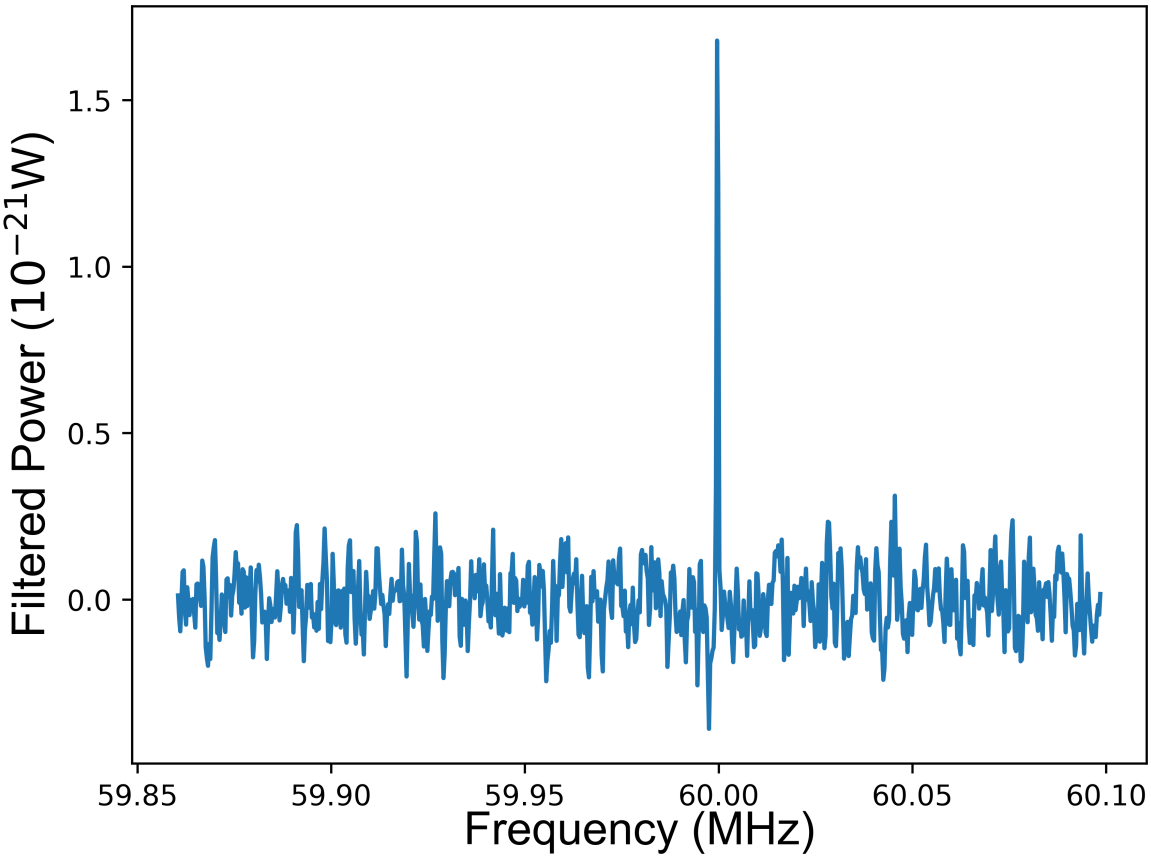

Figure 3.13: Filtered span after being passed through the Butterworth filter shown in 3.12. Note that the amplitude of the high Q candidate at 60 MHz is not reduced after being passed through the filter. This highlights the importance of setting the cutoff such that candidates are not attenuated while still eliminating baseline shaping.

threshold using standard statistics.

Given n Gaussian-distributed, independent, random samples, the goal is to determine threshold such that there is a $p(x)$ chance of seeing such an event (with the null hypothesis that it is drawn from the same Gaussian distribution). Normally, x is set at 0.95. Thus, given n samples, the goal is to set some threshold such that there is only a 5% chance of

seeing a deviation greater than that value.

Equivalently, for n samples, the goal is to solve the equation for the threshold value $0 \leq x \leq 1$ with

$$1 - p^n \leq x \tag{3.4}$$

yielding

$$p^n = 1 - x. \tag{3.5}$$

Substitute $\delta = 1 - p$ and Taylor expand around $\delta = 0$ up to first order to find

$$\delta = \frac{1 - x}{n}. \tag{3.6}$$

Converting to an equivalent z-score can be done numerically or via a table. Using the results for this experiment, with $n = 363,200$, gives a 95 % confidence limit of 5.14σ. However, all candidates greater than 5σ were classified as interesting and looked at. Because of span-to-span differences, each span was analyzed individually in the same fashion as Figure 3.14.

Determination of the mean and standard deviation was done on a sample-by-sample basis by looking at the standard deviation of all the bins not equal to the bin of interest. In other words, to determine the mean, μ_i, and standard deviation, σ_i for the i-th index bin, x_i $(1 \leq i < n)$), in a span of n bins

$$\mu_i = \frac{\left(\sum_{k=1}^{n} x_k\right) - x_i}{n - 1}, \tag{3.7a}$$

$$\sigma_i = \frac{\left[\sum_{k=1}^{n} \left(x_k - \mu_i\right)^2\right] - \left(x_i - \mu_i\right)^2}{n - 1}. \tag{3.7b}$$

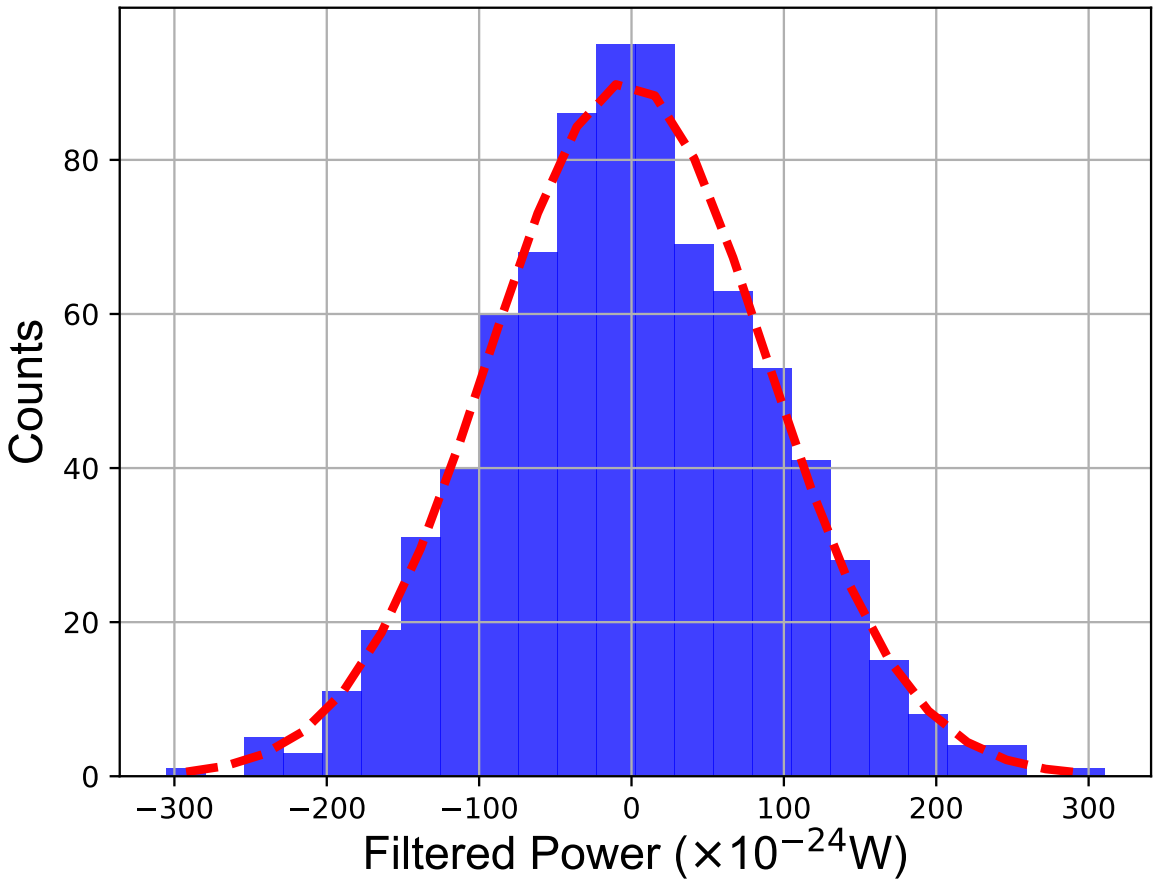

Figure 3.14: Histogram of the filtered power data in 3.13. The candidate signal at 60.00 MHz got removed by setting the 3 bins associated with the spur to the median value of the scan before filtering in order to get rid of ringing artifacts. A Gaussian was fit to the data and a simple Pearson's χ^2-test performed that produced a p-value of 0.96 consistent with the null hypothesis that the data are Gaussian-distributed.

Because of the high-pass filter, u_i should be 0 to high precision, so this is effectively a consistency check. Then, to check if a sample is significant, compute the following test statistic ξ

$$\xi_i = \frac{x_i - \mu_i}{\sigma_i} \tag{3.8}$$

for all bins in the span. All candidates with $\xi_i > 5$ were checked by hand and excluded as candidates of interest. In total, 139 out of 363,200 points were identified in this fashion. The description of how these candidates were excluded as dark photon signals is given in Chapter 4.

Chapter 4

Measurements and Results

This chapter describes the results from the first run of the Dark E-Field Radio experiment. Over the course of 133 days, 3.8 hours of live-time data were taken between 50 and 300 MHz with a resolution of 10^5 or better using a commercial real-time spectrum analyzer (RTSA).The first run of the experiment provided a proof of concept of experimental design. For this feasibility study, a biconical antenna, low noise, room temperature amplifiers, and a commercial real-time spectrum analyzer (Rigol Model RSA5065-TG) were used. Memory limitations on the RTSA necessitated splitting up the full span into 454 sub-spans, which is why we did not increase the resolution to 10^6. This pilot run set a limit on the coupling constant, ε, of $\sim 10^{-11.5}$. We also did four narrow-band spot checks at 63.9, 70.5, 152, and 247 MHz with at least 5×10^5 s of real-time data setting limits on ε of $\sim 10^{-12.5}$.

4.1 The Experiment

In the experiment, memory limitations of the RTSA required splitting up the entire spectral range into a series of sequential spans, which reduced acquisition efficiency. This span is, in part, defined for a given window type, by a span-per-resolution ratio, *SRR*. Given a required resolution, Q (defined as frequency divided by resolution bandwidth), a center frequency, *CF*, the span of a scan can then be calculated from

$$\text{Span} = CF\left[\frac{Q}{SRR} + \frac{1}{2}\right]^{-1}. \tag{4.1}$$

As an example, for a fixed resolution of 10^5 and a 1024-point Kaiser window, this requires 454 separate scans to cover the entire range from 50-300 MHz.[1] This loss in efficiency will be mitigated in the ultimate real-time data acquisition system as discussed in Chapter 5, allowing simultaneous acquisition across the entire spectral range.

In order to make external EM interference subdominant to contributions from thermal and amplifier noise, the shielded room must have greater than 100 dB shielding across the entire spectral range surveyed (discussed in Chapter 2). Experiments done to verify that the shielded room met these requirements confirm that the dominant contribution to the noise floor is not from externally generated EM sources. Nonetheless, we shielded the walls of the external lab space as well. However, a few high-power known signals were detected inside the shielded room. Thus, monitoring of the spectrum outside the shielded room is a necessary feature of the experiment. Any signal detected in the shielded room must be at least 100 dB

[1] The constant of 1/2 comes from requiring that the resolution requirement of 10^5 is met at the beginning of the span.

stronger outside if it is due to external RF. As described in Figure 4.2 and Section 4.3, for the first run of the experiment, candidate signals that were invariant on minute-long time scales were subsequently looked for in the lab space outside the shielded room using the same spectral monitoring setup as the data run but with the shielded room door open. For the next phase of the experiment, data and external lab space scans will be taken contemporaneously allowing for both real-time and post-acquisition vetoing of candidates.

The RF noise in the shielded room is non-zero and originates from two sources. First, the thermal background due to operating this experiment at room temperature. And secondly, the wideband noise of the preamplifier itself. A noise spectrum covering the full range of the biconical antenna is shown in Figure 4.1. The measured RMS noise-voltage spectral density versus frequency is shown, referred to the output of the antenna. Also shown for reference is the short-circuit noise spectral density of the preamplifier.

4.2 Data Acquisition and Analysis

To search for a monochromatic signal (one spectral bin) in the presence of noise, the amplitude of each bin must be understood relative to the noise floor. This noise floor is not flat, due to a combination of shielded room and instrument effects. To resolve this, the power spectrum of each bin-averaged span is passed through a high-pass filter to remove low frequency baseline shape (in the frequency domain). Details of this filtering process are given in Chapter 3.

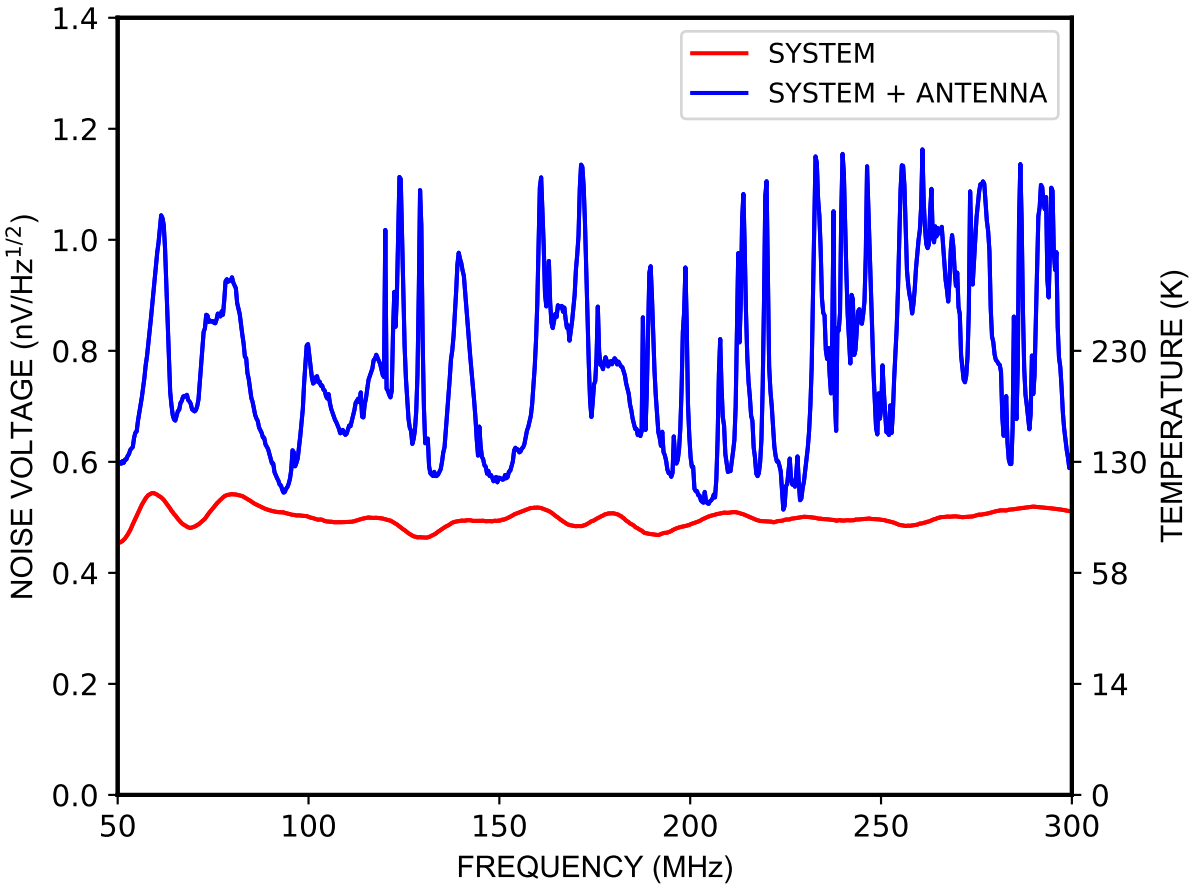

Figure 4.1: Blue: The spectrum of noise in the shielded room referred to the input of the preamplifier. This shielded room thermal noise is on top of the wideband noise of the room temperature preamplifier. Red: System noise temperature referenced to 50 Ω (the input impedance of the preamplifier) for short-circuited preamplifier input.

Memory limitations in the RTSA used in the experiment require dividing the 50–300 MHz range into a series of smaller scans called spans, each of which has the required fractional spectral resolution (see Equation 4.1). These narrow spectral spans are further subdivided in time into smaller, 10-second time intervals to maximize the ability to veto spurious external noise while also being written sufficiently infrequently to avoid write-to-disk bottlenecks

leading to losses in scanning efficiency. All data files are written out in a plain text format and saved to disk. Afterwards, they are converted to fixed-size, binary format (HDF5) files for data processing. The resulting time-frequency database of time-tagged sequential spectral spans enables a series of detection validation tests. Any detection of a monochromatic signal may be examined for its time dependence and also compared in amplitude with the expected 100 dB stronger signal on a spectrum analyzer and broadband antenna outside the shielded room.

Conversion to a limit on ε was done by computing the standard deviation of the filtered power spectrum (filtering was done after subtracting the noise temperature of the amplifier), like that shown in Figure 3.14. Each point in each span was multiplied by a confidence threshold κ to give a threshold power. A discussion of how this threshold was determined is given in Section 4.4.1. Conversion to RMS voltage was done by propagating the error to give

$$\sigma_V = \frac{1}{2}\sqrt{\frac{|Z|}{P}}\sigma_P, \tag{4.2}$$

where σ_V gives the uncertainty on the RMS voltage, σ_P the uncertainty on the power, P is the measured power in a bin, and Z is the input impedance of the spectrum analyzer, which is 50Ω [114]. Then ε was solved for using results from Chapter 2 to give

$$\varepsilon = \sqrt{\frac{\epsilon_0}{2\rho_{\mathrm{DM}}}}\,(AF)\,\sigma_V \tag{4.3}$$

where AF is the simulated antenna factor, ϵ_0 the permittivity of free-space, and ρ_{DM} the local dark matter energy density.

4.3 Search for a Signal

In this section we outline the process of searching for a narrowband constant signal, and describe the results of the first run. Due to the low efficiency of searching 50-300 MHz we consider two types of searches:

1. A 100% efficient search confined to several narrow spans at several spot frequencies.

2. A broadband search covering 50-300 MHz but at $\sim 1/400$ the efficiency of the spot limits.

After an initial run is performed, and the data are processed, we must determine where any potential high Q signals that match the criteria originate. The methodology for this process is outlined in Figure 4.2.

The RF spectrum outside the shielded room is dominated by electromagnetic signals which contain information. Thus, in general, they do not exhibit extremely high Q and constant amplitude. The nature of any signal detected in the shielded room may be revealed by comparing the signal measured inside the shielded room to the signal outside the room. External electromagnetic signals in the frequency range should be attenuated inside the shielded room by 100 dB or more.

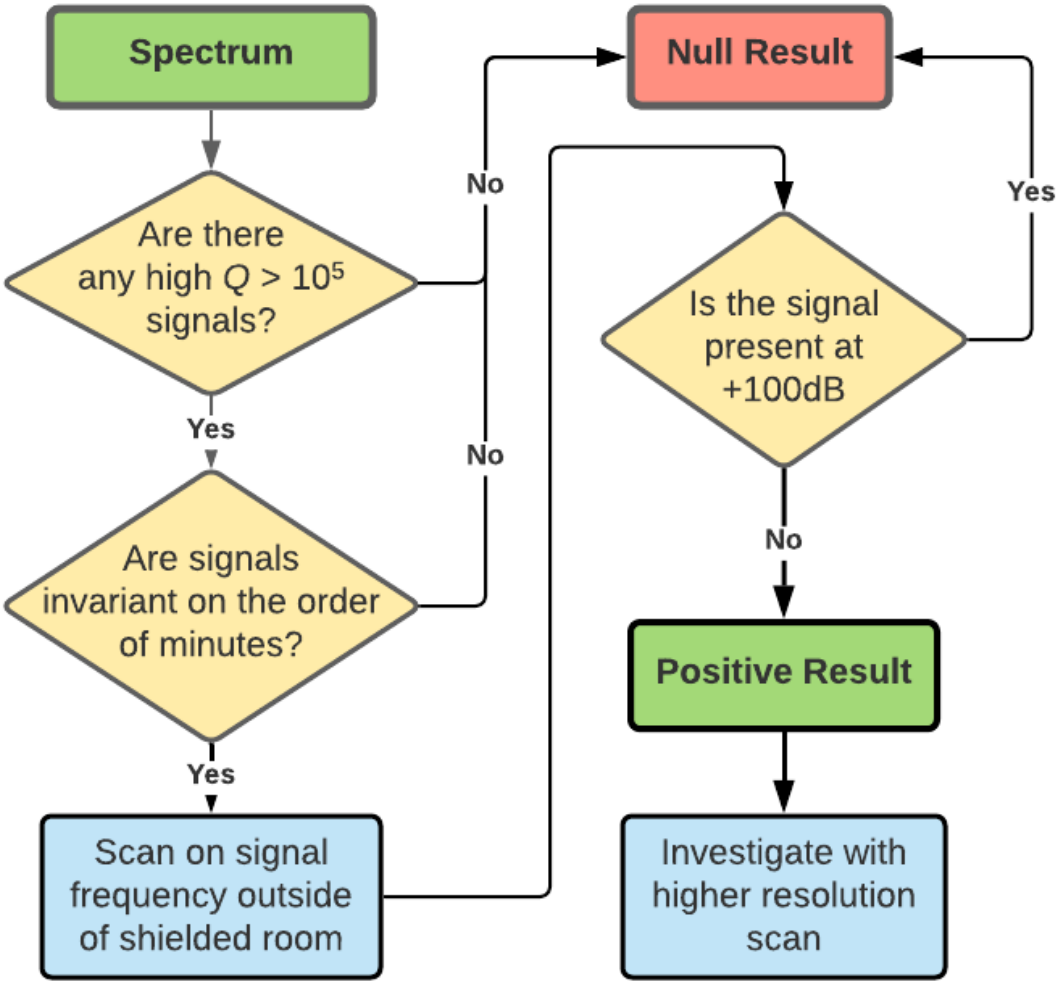

Figure 4.2: Flow chart describing the logic of the search process. Starting with the data from the measured spectrum, the figure shows analysis of a detected signal, and the automated methodology for eliminating false positive signals.

This search logic flowchart applies to the next phases of the experiment as well. Once a candidate high-Q, apparently constant, signal is detected there are a series of investigations that will occur. Using a higher-resolution, smaller-span, targeted run the shape of the line

could be investigated, and any time-variation detected. Based on those results, as well as non-detection outside the shielded room, the next step will be to confirm the signal in an identical setup some distance away. Finally, the next obvious step will be to focus on that frequency with the vastly superior sensitivity of a superconducting quantum limited detector of the kind employed by the Stanford group [123].

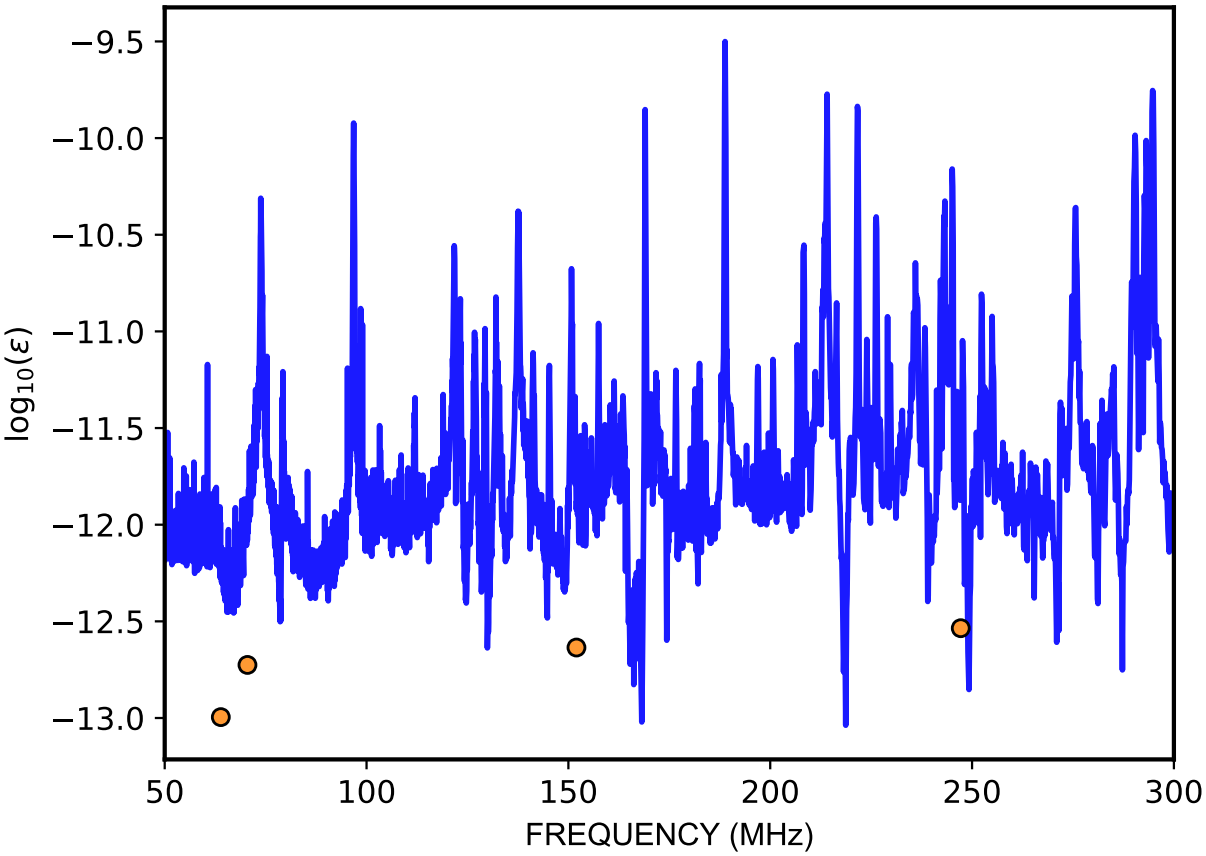

Figure 4.3: Reach of the experiment after short test integrations. The blue curve is for only 3.8 hours of real-time data collection. The orange dots show spot measurements at 63.9, 70.5, 152, and 247 MHz taken with at least 5×10^5 s of real-time data extrapolated to 1 month of data acquisition (assuming the current noisy receiver), and are offset from the blue curve by the expected amount due to the different integration times.

4.4 Limits on ε in the 50–300 MHz Range

The first run of the experiment was done over the course of two months scanning between 50 and 300 MHz. A list of run details is given in Table 4.1. Figure 4.3 shows the results of approximately 3.8 hours of real-time data collection from 50-300 MHz using the system shown in Figure 2.1. This short effective integration resulted from the dead time of the RTSA inherent in the sequential frequency scans. The data-taking procedure is outlined in Sec. 4.2. Conversion from voltage to electric field was done using the modeled AF shown in Figure 2.8. This was converted to an ϵ limit by looking at the standard deviation of the electric field at each bin and calculating the 5σ limit described in Section 4.2.

Run Details	
Span	50-300 MHz
Antenna	AB-900A biconical antenna
RTSA	Rigol RSA5065-TG
Resolution	$\geq 10^5$ across the entire spectral range
Window type	Kaiser
Total spans	454
Acquisition time per span	100 ms
Total time per span	10 s (100 averages)
Total time taking data	133 days
Total time per span	$\sim$ 13800 s
Points per span	800

Table 4.1: Details of the initial run of the Dark E-Field Radio experiment

4.4.1 Determination of Candidates

A 5σ limit was chosen because it overlapped with the 90% confidence limit. To set a confidence limit, the goal is to solve the equation

$$(1-p)^n = \textit{confidence limit} \tag{4.4}$$

where p is the right-handed cumulative distribution function (CDF) of the parent distribution function, n the number of samples, and *confidence limit* the confidence limit normally set to 95%. Samples are taken to be independently drawn from the parent distribution since the expected bin width of a candidate is a single bin. To good precision, this can be Taylor expanded and solved for p given that $n = 454 * 800 = 363,200$.

Assuming that the parent distribution is Gaussian, a z-score, corresponding to a certain number of standard deviations (σ) away from the mean can be solved for a given confidence limit via numeric approximation of the inverse CDF. When this is done, the 90% threshold is set at 5σ and the 95% threshold set at 5.1σ.

This search produced approximately 130 bins where there was a signal of interest (equal to 0.03 % of all bins in the search). Many of these signals were quickly excluded via Step 2 in Figure 4.2. Signals that remained after this process were generally excluded by Step 3. However, care must be taken because some of these candidates were transient. Looking at the dependence of the voltage noise above baseline on the time of day the signal gives a further handle on whether to exclude these as possible candidates. As described in Figure 4.2, splitting up the data into short time bins, enables monitoring signals versus time in order

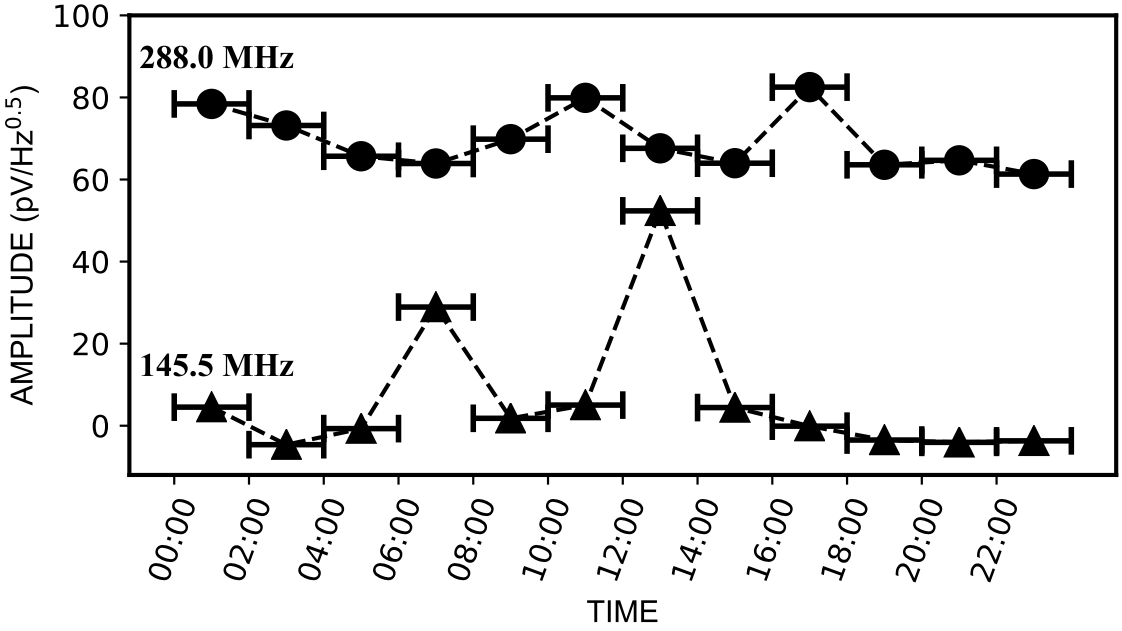

Figure 4.4: Voltage above baseline of ∼19 minutes of data over a 2-hour time window. At 145.5 MHz, a weekly ham radio net on the 100 W K6JRB repeater at 12:30 p.m. is clearly detected. This signal can be eliminated due to short term time-variance. At 288.0 MHz, a possible candidate of unknown origin is shown. This is eliminated by checking the signal outside the shielded room, finding it 110 dB stronger.

to discriminate transient interference from candidate dark photons. Figure 4.4 highlights the transient nature of one of these candidate peaks at 145.5 MHz, which is the location of a weekly ham radio net.

The other candidate detection at 288 MHz was eliminated by comparing with the RF spectrum outside the shielded room. While there is variation in the SNR at 288 MHz, the candidate is only conclusively excluded by doing a narrow-band sweep around the candidate frequency outside the shielded room. The result of this is shown in Figure 4.5. From this, it

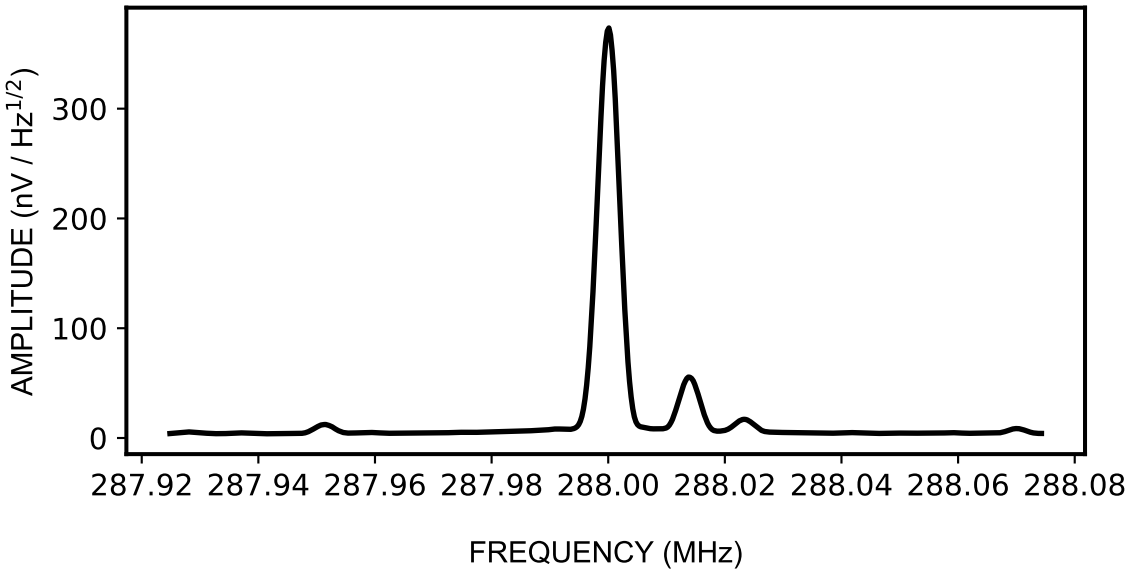

Figure 4.5: A scan around a candidate signal at 288 MHz done with a wide-bandwidth Vivaldi antenna outside the shielded room showing 1,000 seconds of real-time data. The signal is 100 dB stronger than the shielded room detection. This excludes this signal as a candidate. Other EM peaks, also from the same antenna, are evident but are below the sensitivity of the experiment when the shielded room door is closed.

is clear that this signal has terrestrial origins.

4.4.2 Limits on ε at four spot frequencies

Four narrow-span scans around 63.9, 70.5, 152, and 247 MHz were chosen as a second calibration of sensitivity as shown by the orange dots in Figure 4.6. For each spot check, at least half a million seconds of data were obtained and used to compute a 5σ limit on ε. This limit was extrapolated to a month using Equation (2.19). The locations of spot frequencies were chosen to sample across the entire 50–300 MHz span as well as to investigate the sensitivity

of the experiment in regions with and without room modes. Span widths were selected to ensure a resolution of at least one part in 10^5 and are the same as used in the full data run. (Figure 4.3).

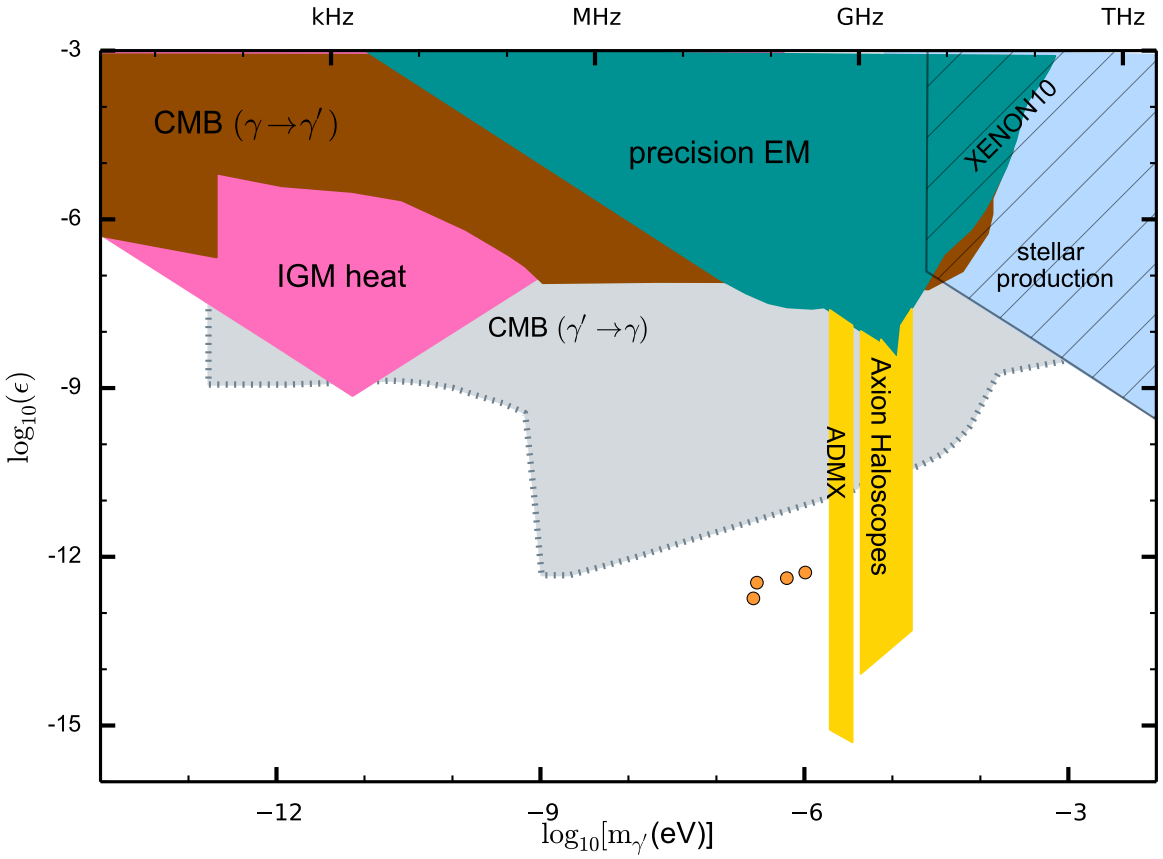

Figure 4.6: Limits from spot measurements in the 50–300 MHz region shown along with existing limits. The equivalent mass range is 264 - 1021 neV.

It is expected that near room modes (see Figure 4.1), sensitivity will improve. However, this is complicated by the properties of the antenna itself (see Figure 2.8). The resulting AF is effectively a convolution of the two and can only be calculated via EM simulation.

Using data from the experiment, we estimated the the constraining power versus integra-

tion time in various frequency (dark photon mass) bands. This is crosschecked with real-time narrow-span scans around 63.9, 70.5, 152, and 247 MHz as a second calibration of sensitivity. The limit plot in Figure 4.6 shows the extracted limits between 50–300 MHz. This set of spot limits has excluded possible values of ϵ at four points in the dark photon mass range of 264 - 1021 neV. While it is not appropriate to interpolate between those points in order to claim such exclusion for ε in that mass range, it is indicative of the power of this technique to extend sensitivity in the hitherto unexplored parameter space.

The limit plot in Figure 4.7 shows current limits for the 3.8 hr run overlaid with extrapolated limits assuming lower noise temperature LNA and improved RBW after a 1-month long data acquisition from 50–300 MHz. Spot checks at 63.9, 70.5, 152, and 247 MHz are also overlaid.

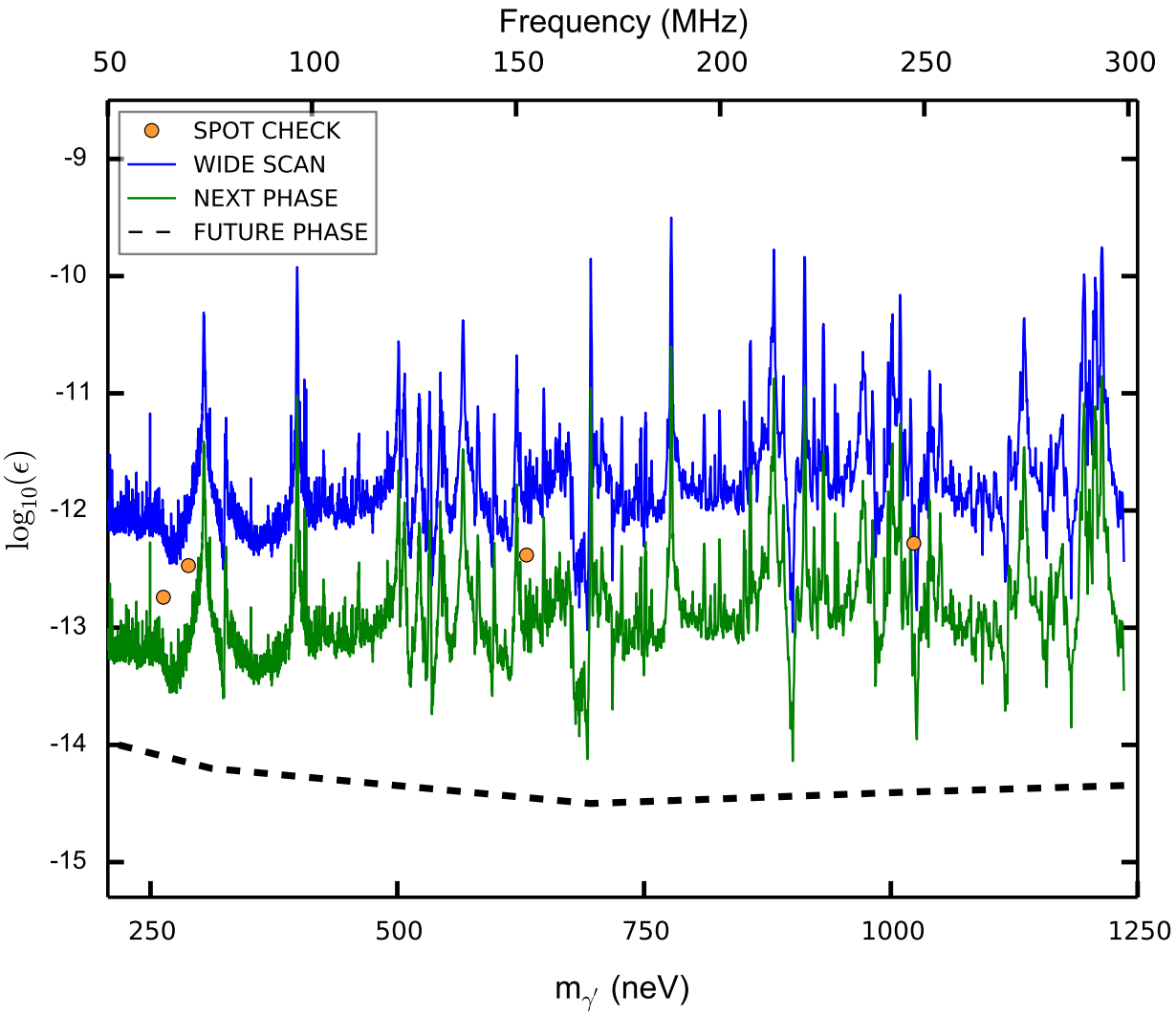

Figure 4.7: Limit plot showing the reach of the experiment from 50–300 MHz in several stages. Pilot (blue) shows 5σ limits after 3.8 hours of data collection using the proof-of-concept setup. Phase-I (green) shows 5σ extrapolated limits using current antenna with LNA noise temperature and RBW improved by a factor of 2 and 10, respectively, after 1-month of real-time data acquisition. Spot checks (orange) show measurements around 63.9, 70.5, 152, and 247 MHz taken with at least 5 $\times 10^5$ s of real-time data in the experiment. Unlike Figure 4.3, these values are not extrapolated to 1 month. As expected, these limits lie between the measured and projected limits from the current and next phase runs, respectively. Phase-II (black) shows the projected 5σ limits for a month-long data run after reducing the system noise temperature.

Chapter 5

Improving Acquisition Efficiency for the Next Phase

The first run of the Dark E-Field Radio Experiment showed the feasibility of this detection method to detect dark photons and set limits on the dark photon coupling strength at RF frequencies. However, this experiment suffers from low acquisition efficiency and poor spectral resolution, a byproduct of the current acquisition method. This chapter describes the work being done in preparation for the next phase of the experiment, which will be a run from 50 to 300 MHz using a custom-designed real-time spectrum analyzer with a resolution of one ppm or greater over the entire span. The rest of the chapter is devoted to a discussion of the development and design of this data acquisition system.

5.1 Design of the ROACH System

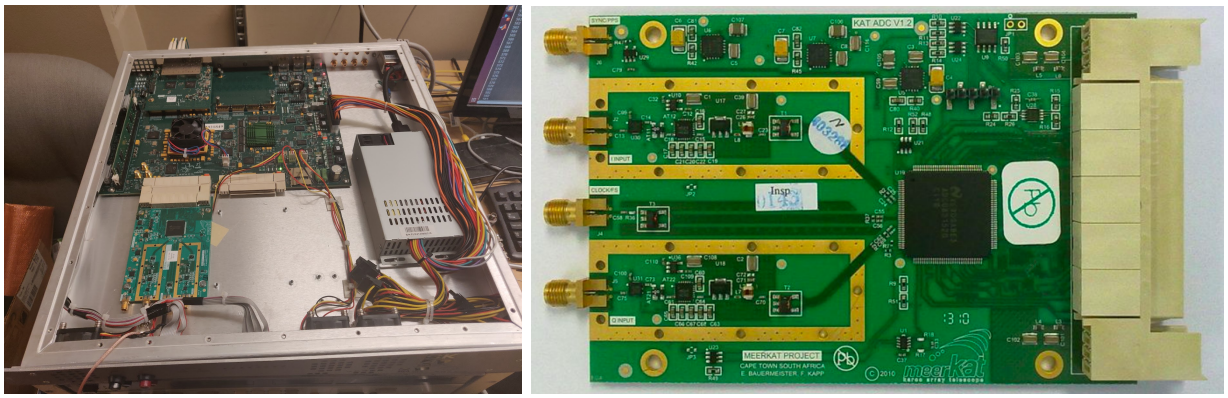

Figure 5.1: (Left) Picture of the full ROACH system showing the KatADC coupled to the ROACH board. (Right) Zoom-in of the Kat-ADC. The KatADC board has four SMA inputs ([124]) for data (I/Q), clock, and sync inputs. For this design, only a single input channel and the clock are used because the input channels are combined (interleaved) to form a single channel, and there is only one KatADC so an external sync connection is unnecessary. The clock is a 0 dBm sine wave externally provided by a Rigol DSG830 RF signal generator. Outputs are routed to SMA connectors on the back of the ROACH enclosure, which allows the entire system to be fully enclosed.

The Reconfigurable Open Architecture Computing Hardware (ROACH)-2 board comprises a standalone field-programmable gate array (FPGA) processing board for generic data acquisition and analysis (although geared towards radio astronomy) designed by the Collaboration for Astronomy Signal Processing and Electronics Research (CASPER). The ROACH-2 (hereafter referred to as the ROACH), also includes the Simulink-based library design blocks specific to CASPER boards.[125] This greatly eases the development of the data acquisition (DAQ) system because everything can be done graphically in Simulink without having to go down to the level of the hardware description language.

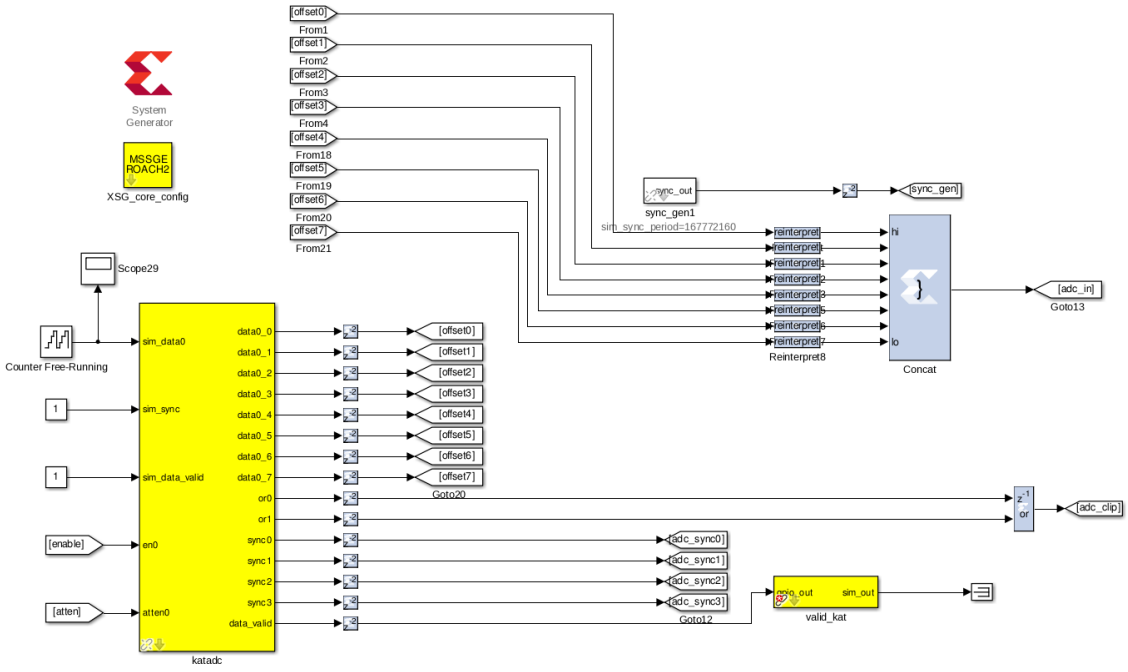

Figure 5.2: Data from the KatADC comes out in 8 1-byte words every FPGA clock cycle. The FPGA clock is 1/8 the sampling rate of the KatADC (75 MHz). Each 1-byte word is concatenated into a 64-byte word that gets sent to the FIFO block. Data are decoded after they are sent to the PC. Care has to be taken to ensure that the data are being digitized and decoded in time-ordered bytes or else there are many FFT artifacts.

The ROACH facilitates communication between a KatADC board, where data are digitized, and a PC, where the data are processed. It is coupled to the KatADC board via its front-end ZDOK+ connector[126, 127]. A picture of the system is shown in Figure 5.1.

When data come into the KatADC, they are first amplified by a 20 dB frontend amplifier on the KatADC. Then, they are digitized by an 8-bit dual 1.5 GHz or single 3.0 GHz Texas Instruments analog-to-digital converter (ADC). Sampled data from the KatADC block are then sent to the Virtex-6 FPGA on the ROACH [128] over the ZDOK+ connector and

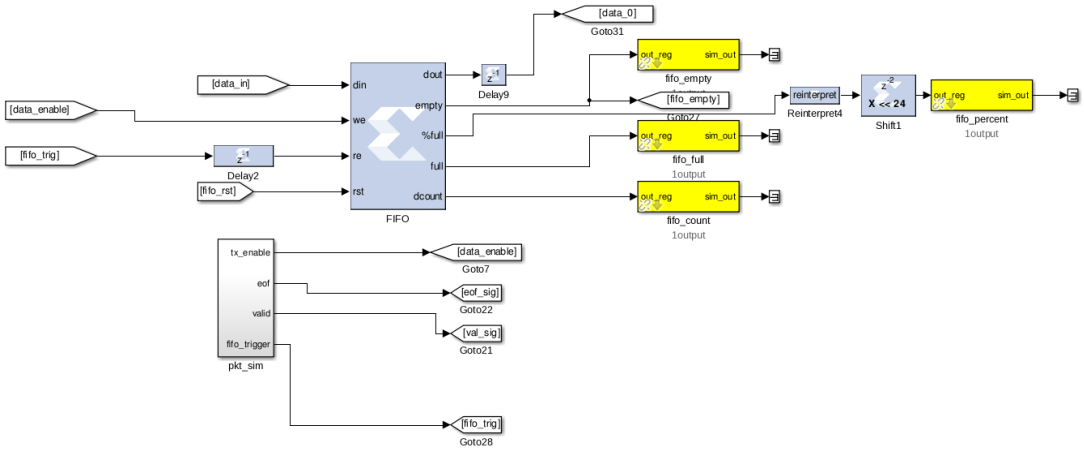

Figure 5.3: Data from the KatADC are buffered into the FIFO block to be stored before being transmitted. The 10 GbE block is able to transmit faster than the FIFO takes in data so this is mostly a fail safe. The *we* (write enable) and *re* (read enable) ports on the FIFO allow the user to meter data into and out of the FIFO in case the FIFO is full or there is a need to limit data going to the transmit block. Yellow blocks indicate registers that can be looked at on the PC to observe the status of the FIFO.

buffered with a first-in first-out buffer (FIFO) before being sent to the 10 Gigabit Ethernet (GbE) line. This goes to a PC where it is copied to a graphics processing unit (GPU) for processing.

The 10 GbE data line is what sets the maximum real-time bandwidth for the system, which is given as half the quotient of the maximum data rate (10^{10} b/s) and the bit-depth of the ADC used on the KatADC, (8 b), which is 625 MHz. With the current setup, we could have up to 1.25 GHz of real-time data acquisition. However, this comes with a large reduction in acquisition efficiency because data streams from each 10 GbE line are not contiguous in time. As a result, lots of extra data have to be taken so that streams can be shifted to be

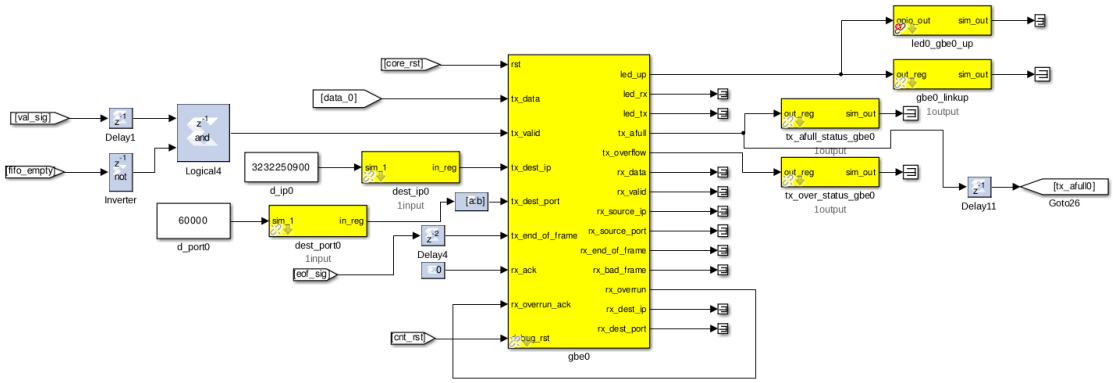

Figure 5.4: Data from the FIFO block are sent to the 10 GbE block where they are accumulated, turned into Ethernet frames, and sent to the PC. Almost all the small yellow blocks are status registers except for the *dest_ip0* and *dest_port0*, where the IP address and port number of the host PC is set for data to be sent. If the FIFO is empty the transmit flag is set to false as a fail-safe to prevent empty packets from possibly being sent. To maximize transmission efficiency, the 10 GbE block sends 8 kB jumbo frames (1024 total KatADC samples or 128 FPGA clock ticks). This needs to be configured on the PC side otherwise data are not correctly received.

aligned with each other. Unaligned data are then thrown away, which results in a significant loss of acquisition efficiency. If better timing could be realized, we can take data with a real-time bandwidth of greater than 1 GHz.

The design of the ROACH is separated into three separate pieces: The ADC Block (Figure 5.2), the FIFO block (Figure 5.3), and the Ethernet block (Figure 5.4). Data from the KatADC come in eight 1-byte packets that are combined to create an 8-byte word. This word is passed into the FIFO where data are stored and passed onto the Ethernet block. The Ethernet block takes the data words and combines them into packets that are then sent to

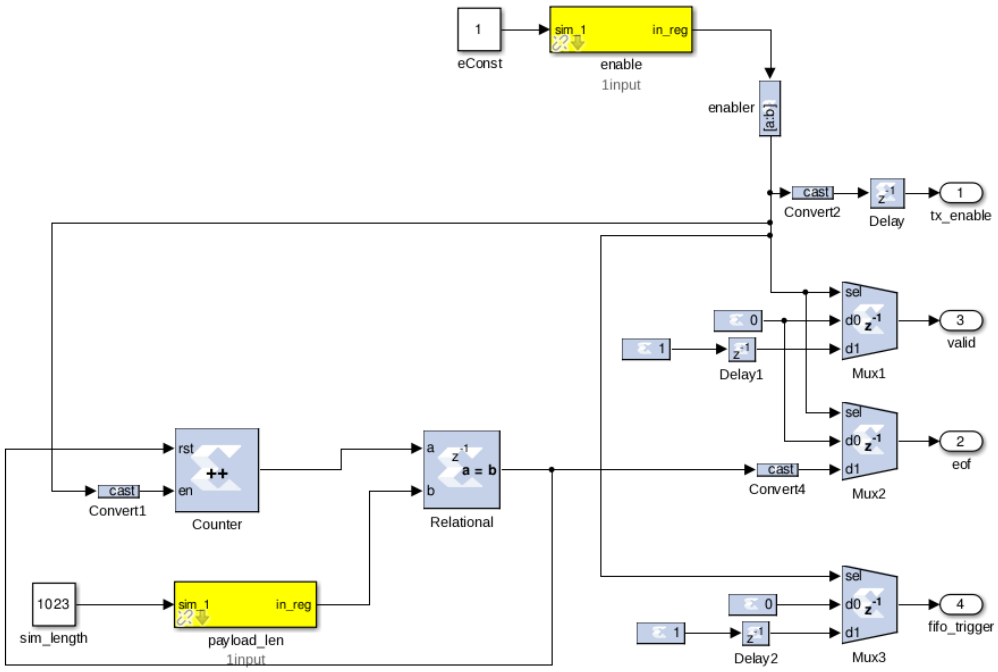

Figure 5.5: The *pkt_sim* subsystem contains the logic for generating various control signals. The size of the packets sent to the the PC is set here and is also controllable from the PC. Other signals controlled here include the end of frame (EOF) signal, which goes high on the last clock packet of the frame, read enable, which is set for the FIFO, and transmit enable on the 10 GbE block. More complicated logic may be needed if we are write limited. However, this is not the case, so the main purpose of this subsystem is to pulse EOF high for one clock cycle whenever it is time to send an Ethernet frame.

the PC. Logic for when to package Ethernet frames and send them to the PC is configured in the *pkt_sim* subsystem shown in Figure 5.5.

Ultimately, the ROACH board is being used as a conduit between the KatADC and the PC where the data are processed. Originally, the goal was to do an onboard FFT of the incoming data. Memory limitations of the ROACH then required careful averaging methods

to maintain resolution requirements while not exceeding the memory of the ROACH itself. However, GPU's now have enough memory to perform large FFT's so it is faster and easier to perform the FFT on the GPU than it is on the ROACH itself. As a result, time domain data are transferred off the ADC to the PC where they are subsequently copied to a GPU.

The entire data acquisition and analysis script is done in Python3 simultaneously and in real-time. This includes data acquisition, performing the FFT, writing to disk, monitoring the RF spectrum in the lab space outside the shielded room, and displaying run information.[1]

5.2 Using the ROACH

Now that the DAQ system has been developed, we can develop the next phase of the experiment around it. This involves careful examination of some of the noise issues that reduce the dynamic range and require a rethinking of how to perform the experiment to limit the effect of high-Q spurious signals, that mimic dark photon signals, and are injected into the data acquisitions by the ROACH. This section details this effort.

5.2.1 ROACH Spurs

Candidate signals are estimated to have a Q of $\sim 10^6$. If we assume that that is true across the entire span, then to maximize the SNR, we would like 50 Hz resolution (quotient of the minimum frequency and Q). To determine the length of the FFT required to do that, we

[1]There are actually slight delays due to experimental design choices. These are described in Section 5.2.3.

can take the clock rate (given by Nyquist as twice the maximum frequency in the span[121]) and divide it by the required resolution bandwidth (RBW).[2] We would also like the length of the FFT to be a power of 2 since computational efficiency is important for a real-time system. From these requirements, we calculate the required FFT length as

$$\begin{aligned} n &= \lceil \log_2 (2 f_{max}/RBW) \rceil \\ &= 24. \end{aligned} \tag{5.1}$$

A 2^{24}-point FFT has a resolution of $f_s/2^n = 35.76\,\text{Hz}$ for a sampling rate f_s of 600 MHz, which exceeds the requirement of at least 50 Hz resolution. Exceeding the resolution bandwidth requirement will not reduce the sensitivity, however it will spread out a dark photon signal across multiple bins.

Spurious signals (spurs) are those that appear as coherent, narrowband signals that mimic the presence of a dark photon and represent a false positive dark matter event detection. Therefore it is important to analyze, catalog, and eliminate, to the greatest extent possible, spurs in the detection system. We start the discussion on spurs by examining how the baseline power-per-bin is reduced by doing a long FFT. An FFT can be viewed as a series of bandpass filters, splitting up the power of the signal into a series of bins. From Parseval's Theorem [121], the FFT is power preserving so there is an equivalency between the power of the signal in the time domain, and the power of the signal in the frequency domain. Assuming that the power-ber-bin is constant, then the baseline (equivalently the power in

[2] Windowing will increase the resolution bandwidth by the ENBW. For this simple calculation assume that the resolution bandwidth has had the ENBW already accounted for. See Section 2.2 for more information.

each bin) is proportional to the the number of bins. The quotient of the signal power in the time domain and the power-per-bin in the frequency domain is called the *process gain*. For a real signal, the process gain, G_p for a length M FFT is given by

$$G_p = 10\log_{10}\left(\frac{M}{2}\right). \tag{5.2}$$

As an example, for a 2^{24}-point FFT like that calculated in Equation 5.1, this is 72.2 dB. Assuming that the power spectral-density-per-bin is constant, this means that the FFT will push down the baseline by a factor of $1.66 * 10^7$. This is fantastic for improving the SNR, but we immediately run into problems.

Now, any ADC has distortion products. These are caused by any nonlinearity that exists whether it be timing, integral nonlinearities from sampling, offset mismatch in interleaved ADCs, etc [129]. These nonlinearities cause spurious signals in the sampled output that present themselves as high-Q spurs on the baseline independent of the presence of a real candidate signal. Therefore, understanding and mitigating these spurs (to the extent possible) is very important for this experiment because a dark photon signal will look exactly like a spur. Any spur has to be treated as a candidate and carefully excluded in analysis. This becomes very difficult and time consuming to do in the limit that there are many spurs.

A common figure of merit for ADCs is the spurious-free dynamic range (SFDR), which quantifies the ratio between an ADC's full-scale range (or the carrier signal amplitude) and the largest spur. A visual definition is shown in Figure 5.6. For the ADC08D1520, which is the ADC chip in the KatADC, the SFDR is between 50 and 60 dB.

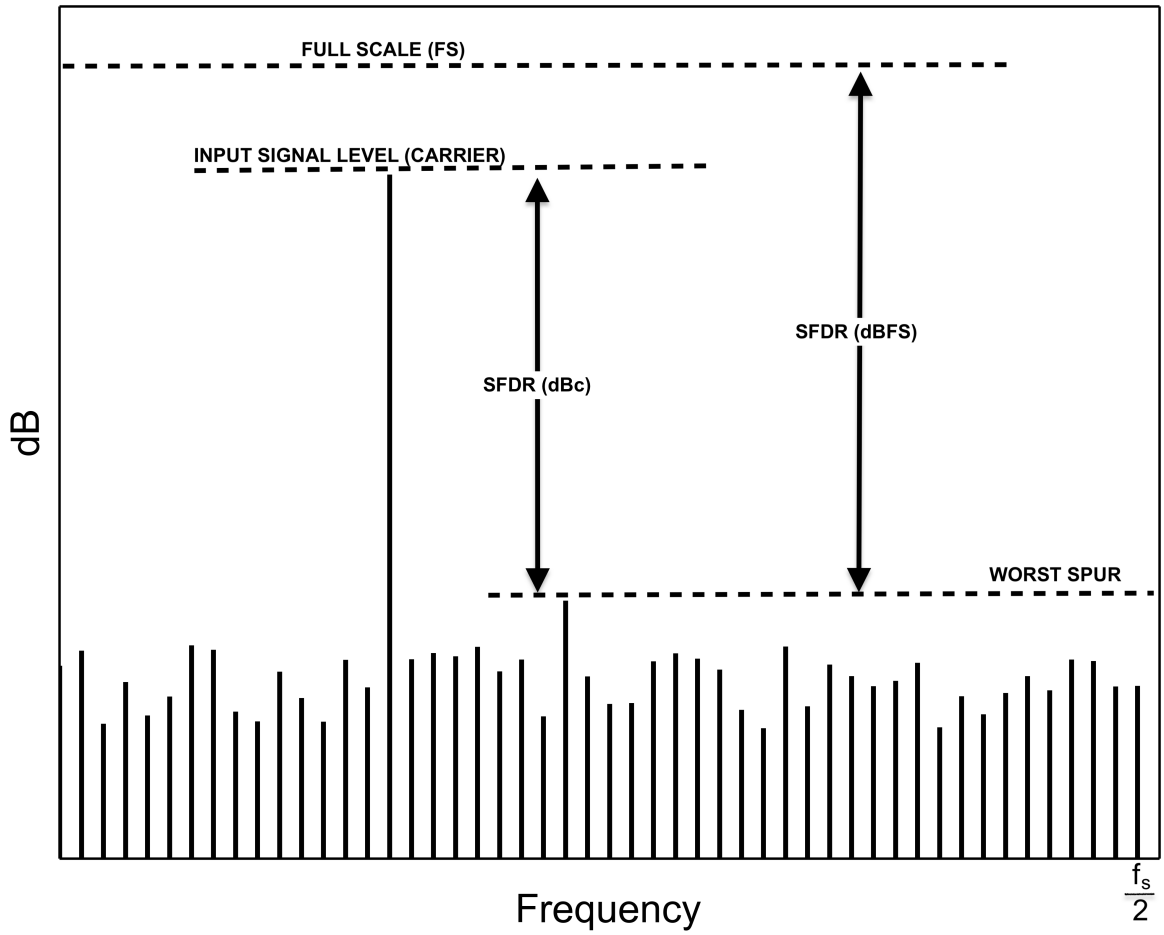

Figure 5.6: A schematic view defining SFDR. Here, the frequency axis goes from DC to half the sampling rate f_s (Nyquist). SFDR can alternatively refer to the size of the input signal relative to the amplitude of the largest spur (dBc) or the amplitude of the maximum signal level (full scale) relative to the amplitude of the largest spur (dBFS). This diagram is inspired by a similar one in [130].

Because the SFDR of the ADC is more than the process gain of the FFT, the baseline will be below the level of spurs. Figure 5.7 shows the extent of this problem. To collect these data, the input to the KatADC was terminated and approximately 5 minutes of data were collected and averaged together corresponding to a total of 10^4, 2^{24}-point acquisitions. The expectation is that the power spectral density will present as the flat Johnson noise (k_BT) of a 50 Ω terminator since the frequencies of interest are well within the Rayleigh-Jeans region [131, pages 20-27]. Instead, there are a large number of high-Q spurs punctuated by one large one at 150 MHz.

This spur is called the *main interleaving spur*. Interleaving is a common technique for high speed ADCs that allows the use of multiple, identical ADCs to sample at a slower rate than data are actually digitized. Slight differences between the gain, phase, and offset between the ADCs cause a nonlinearity that expresses itself as a spur in the FFT. This spur is located at $k/\alpha \times f_s$, with k a non-negative integer, α the number of interleaved ADCs (2 for the ADC08D1520), and f_s the sampling rate. Therefore, this spur is always at $1/2f_s$ ([129] [132]).

Now, Figure 5.7 is a worst case scenario, in a sense, because the baseline is at the noise floor of the ADC. However, even if the total signal power is increased to the maximum input level of the ADC (where the possibility of saturating the ADC becomes very likely, which, in turn, produces a lot of other spurious mixing products), the baseline of the spectrum will still be below the level of the biggest spur because the processing gain is larger than the SFDR.

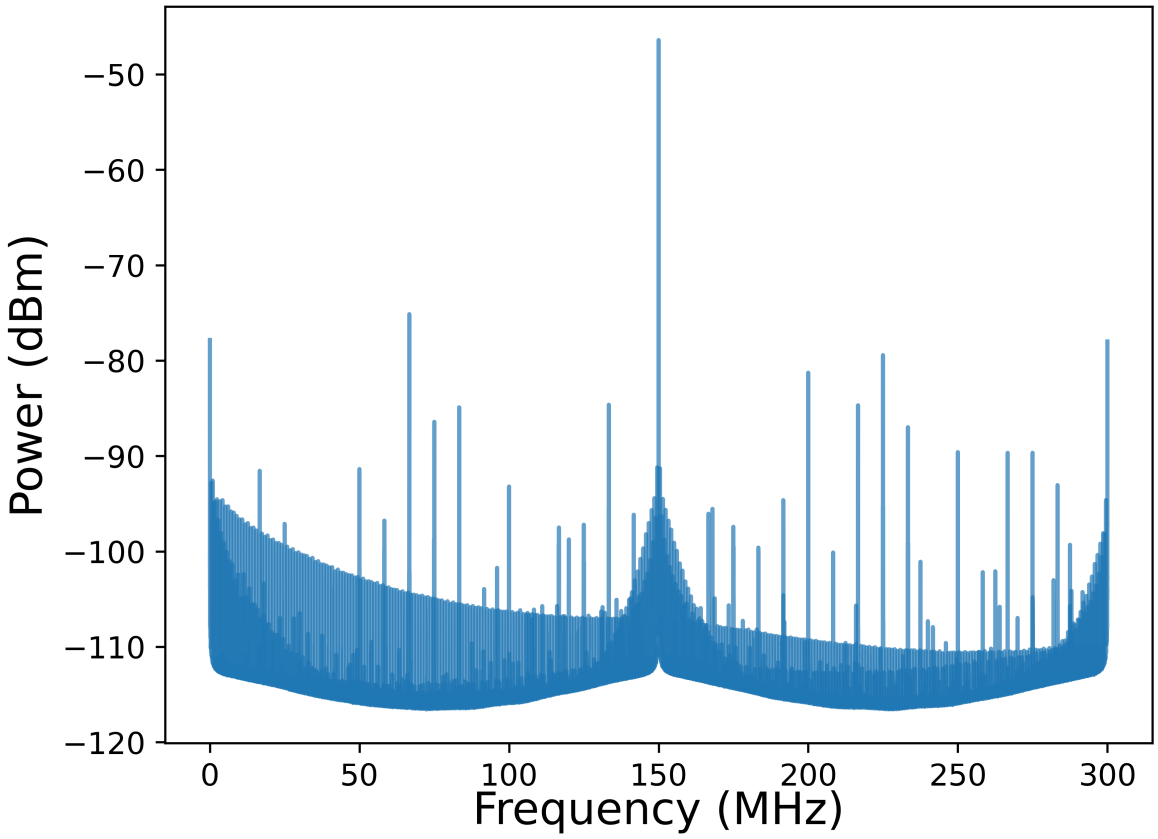

Figure 5.7: 10,000 2^{24}-point FFT power spectra averaged together with the input to ROACH terminated with a 50 Ω terminator. This test shows the large number of spurs that exist when the sum of system gain and process gain is larger than the SFDR. These spurs are identical to dark photons candidates. Therefore, this test also highlights the necessity for strategies to remove or mitigate the effect of these spurs.

One idea to handle this, is to disregard the largest spur since it is always at one quarter of the clock rate. The second largest spur is at -75 dBm. Redefining the SFDR with with respect to this spur, makes the modified SFDR 82 dB (the maximum power input for this ADC is 7 dBm). Now the SFDR is greater than the process gain by 10 dB.[3] This is not the entire story, though, because arguments up to now have only applied to a single FFT.

There is a further factor called *averaging gain*, which is proportional to the number of acquisitions. Assuming that the baseline is Johnson noise, which is a good approximation since the dominant noise source is thermal, then the uncertainty in the baseline is proportional to the ${n_{acq}}^{1/2}$ where n_{acq} is the number of acquisitions taken ([122]). The averaging gain, G_A, is then given (in dB) by

$$G_A = 5\log_{10}\left(\left\lfloor \frac{t \cdot f_s}{2^N} \right\rfloor\right) \tag{5.3}$$

for an acquisition that lasts for a time t at a sample rate f_s, and an FFT of length 2^N. Using $f_s = 600\,\text{MHz}$, and $N = 24$, in 1 day, the averaging gain is 17 dB. Even though the SFDR is 10 dB below the processing gain, we are able to see fluctuations on the baseline that are 7 dB less than that so we will still see many of the high Q spurs. All of this is to motivate that spurs are an inescapable consequence of the current acquisition scheme.

[3]This is also why we do not want to do a longer FFT even though we are capable of doing so. Every factor of 2 increases the process gain by 3 dB, which pushes the SFDR closer to the process gain.

5.2.2 Identifying the Source of Spurious Signals

A perennial question has been whether we can identify the source of the spurs and fix the source or develop a method to mitigate the effects of the spurs. One idea is that the spurs are being generated by the ROACH and being picked up by the KatADC. The KatADC does not have its own power connections, and, as a result, gets all of its power from the ROACH from the 5, 3.3, 2.5, and 1.8 V sources passed from the ROACH over the Z-DOK+ connector to the KatADC. Not only are these voltages generated using switching DC-to-DC converters, but the same ground that is used for all the digital lines (e.g. the PowerPC) is then shared with the KatADC.

Measuring the AC-coupled output from the output of each of the converters shows spurs at each transition as shown in Figure 5.8. This noise should get filtered out, but it can also be picked up on the ground of the ROACH, which would be seen by the KatADC. One attempt to determine if this noise is coming in on the ground is to enable the digital attenuator on the KatADC with the input to the KatADC grounded. If spurious signals are not attenuated when the digital attenuator is enabled, then it is highly suggestive that these signals are coming through the ground on the KatADC.

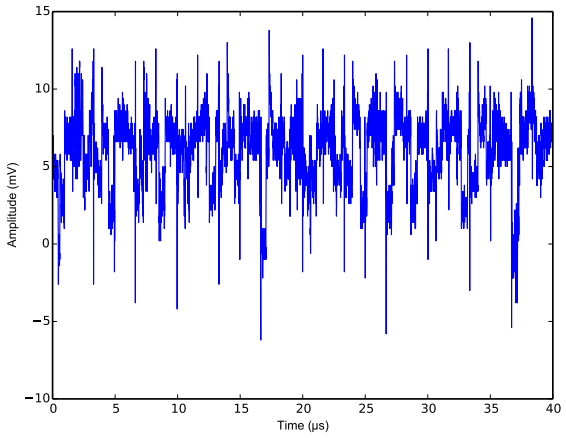

(a) 1.0 V DC-to-DC converter

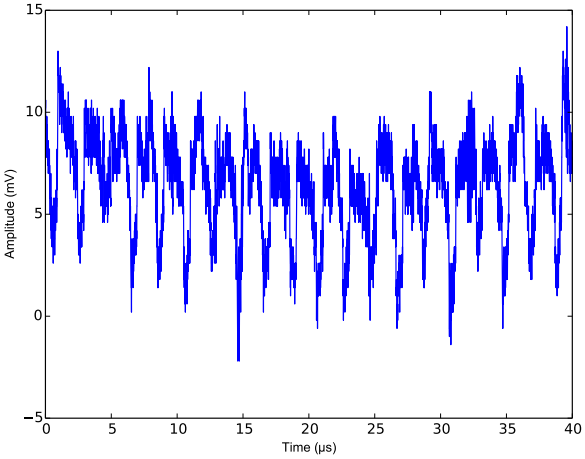

(b) 1.5 V DC-to-DC converter

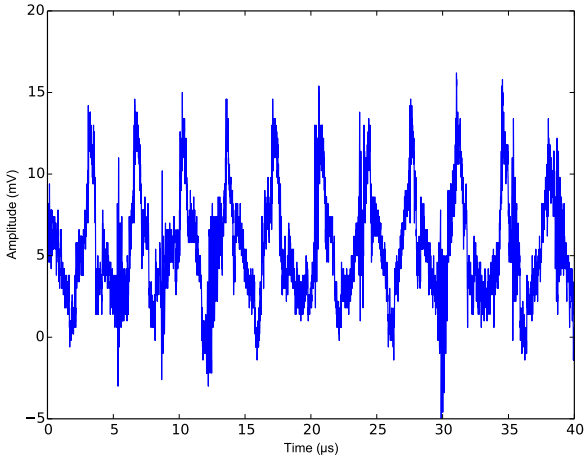

(c) 1.8 V DC-to-DC converter

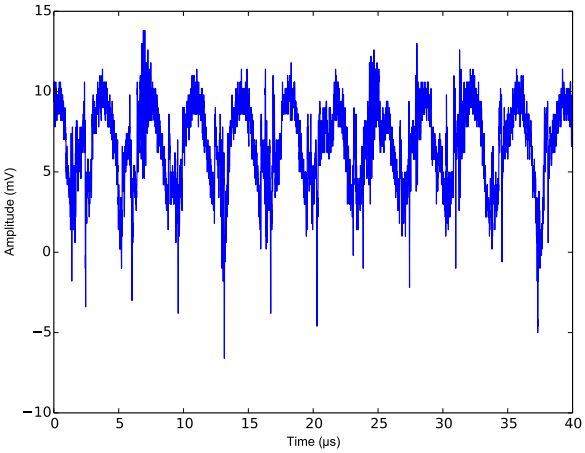

(d) 2.5 V DC-to-DC converter

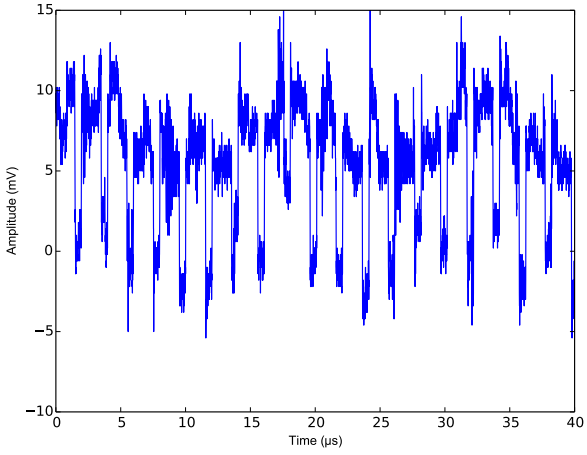

(e) 3.3 V DC-to-DC converter

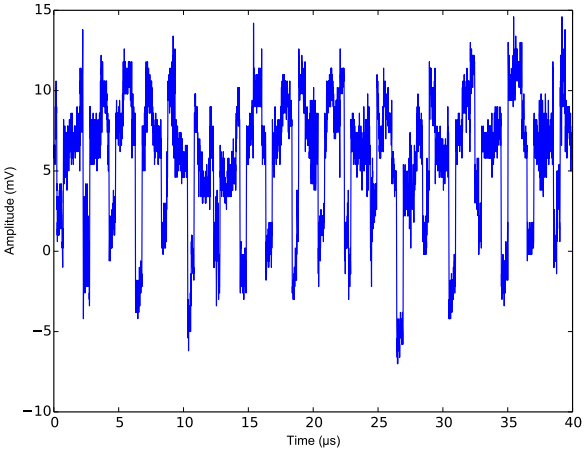

(f) 5.0 V DC-to-DC converter

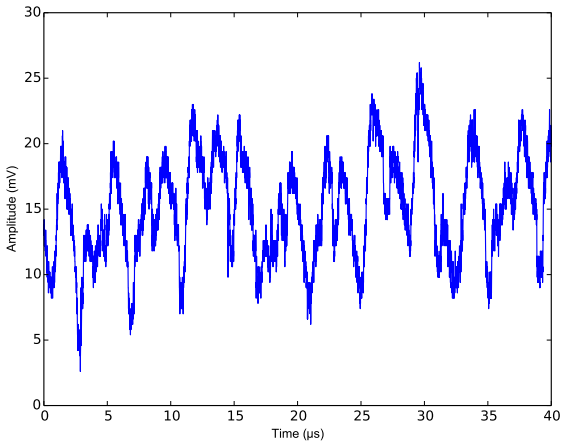

(g) 12.0 V DC-to-DC converter

Figure 5.8: AC-coupled noise coming from the 1.0, 1.5, 1.8, 2.5, 3.3, 5.0, and 12.0 V switching DC-to-DC converters on the ROACH board. Data were taken by probing right at the output of each DC-to-DC converter. It is hypothesized that these transients may be the source of the spurs.

Terminating the input to the ROACH and doing an acquisition with the variable attenuator set at 31 dB (maximum) or 0 dB (off) reveals that including attenuation reduces the size of the spurs but does not eliminate them. An example is shown in 5.9. This suggests that other strategies to mitigate the effects of the spurs have to be developed.

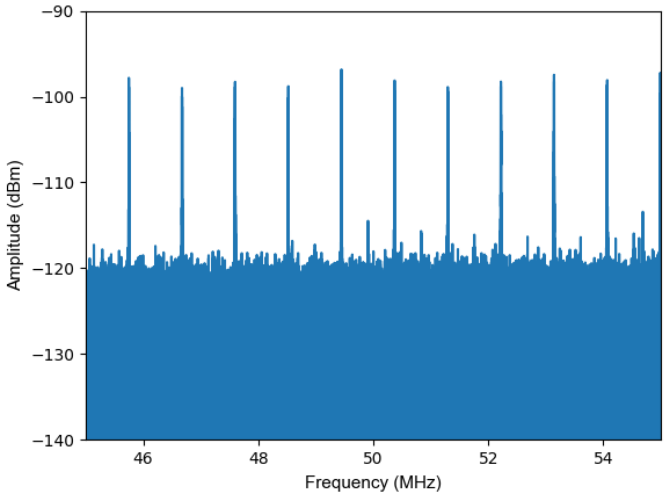

(a) Digital attenuator set to 0 dB

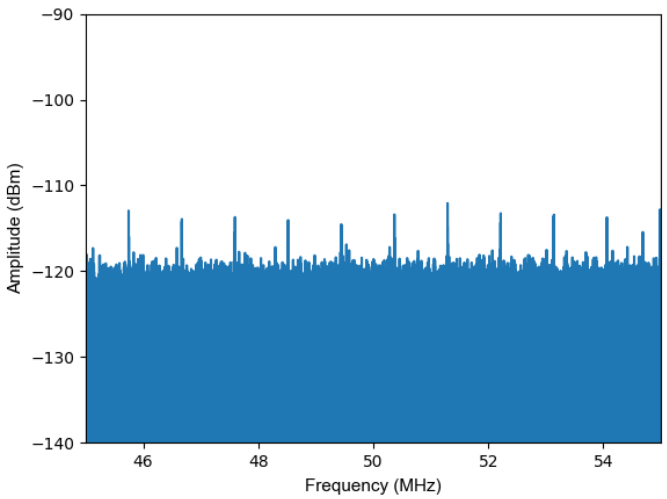

(b) Digital attenuator set to 31 dB

Figure 5.9: Changing the digital attenuator from (a) 0 dB to (b) 31 dB and zooming in on some of the periodic spurs around 50 MHz shows that while some of the spurs have been attenuated, they have not been eliminated. This suggests that these spurs are coming into the ADC through the RF signal chain and the ground.

Data coming into the KatADC pass through a programmable attenuator, get amplified, and then pass through a balun that turns the single-ended input signal into a differential one. In principle, this not only removes the DC component giving a better dynamic range, but also reduces any common-mode noise because of the 180 ° phase difference of the balun's outputs.

However, any signals that are not common-mode will not be filtered out by the balun. One option is to float the ground on the balun and have the signal be fully differential from the output of the antenna through to the input of the ADC bypassing much of the hardware on the KatADC. However, this requires hardware changes across the entire signal chain: The antenna's balun needs to be removed, fully differential amplifiers are needed, shielded differential cables need to be designed, and new panel feedthroughs need to be drilled. Luckily, there are other ways to mitigate the effects of the spurs that do not require an effective redesign of the entire hardware chain. This is discussed in Sections 5.2.3 and 5.2.1.

5.2.3 Stability of Spurious Signals

One way to mitigate the impact of spurious signals in the data is to switch back and forth between two systems: One that has background and signal and one that has only background. For the next data run these will be the biconical antenna and a 50 Ω terminator, respectively. However, stability, both in frequency and amplitude, of these spurs needs to be determined.

This is important not only because these spurs mimic dark photon signals, but also because switching leads to a reduction in acquisition efficiency. To determine how frequently to switch, the setup in Figure 5.10 was used where two $50\,\Omega$ terminators were used, one on each arm of a single-pole double-throw (SPDT) switch. Terminators were used because they are both well matched to the input of the amplifier and also because they will not receive external RF that could confuse results. This test could be done without the switch, however, the switch will be included in the next data run, so it is included here to closely replicate the ultimate system design.

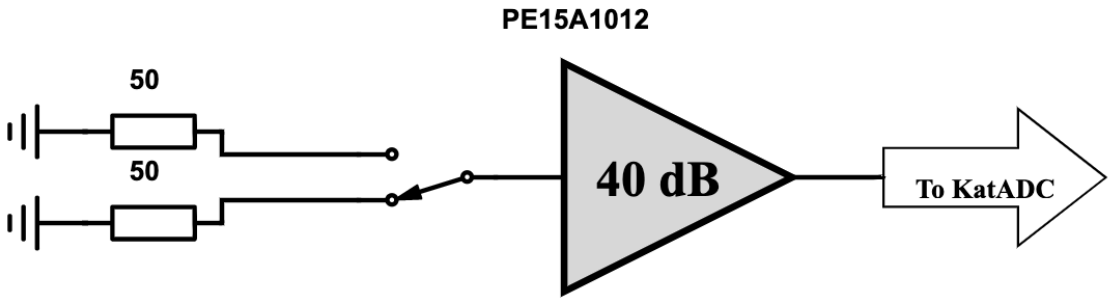

Figure 5.10: Schematic diagram for doing switching tests. The SPDT switch was triggered via a phototransistor that is controlled from a PC located outside the shielded room. Both arms of the switch were connected to $50\,\Omega$ terminators to mitigate the effect of RF being received that could mimic spurs. Output was amplified (to match how data are processed in the actual setup) before being sent to the KatADC.

Spur stability was determined by taking varying number of acquisitions on each arm of the SPDT before switching. For all tests, the total number of acquisitions taken was 10,000 (5,000 for each arm of the switch) except when 10,000 acquisitions were taken on

each arm of the switch and the total acquisitions taken were 20,000. Acquisition length for all tests was 28 ms (2^{24}-samples) to copy the planned acquisition length for the next run of the experiment. The power spectra for all acquisitions on each arm of the switch were linearly averaged together, respectively, and then the two averages divided by each other to produce an averaged ratio spectrum.

By the Central Limit Theorem, this process created a Gaussian-distributed ratio distribution, with a mean around 0, for each test [122]. Spurs that varied on short enough time scales with respect to the time between switching were seen on the ratio plot. Results of this experiment are shown in Figure 5.11.

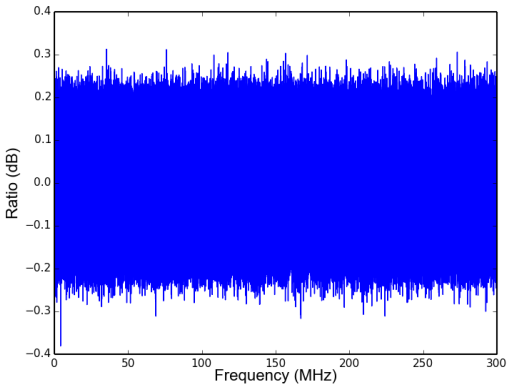

(a) 28 ms

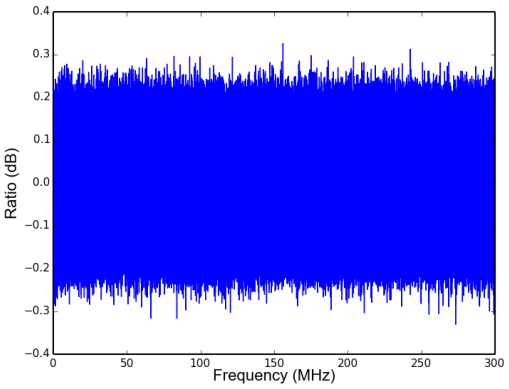

(b) 280 ms

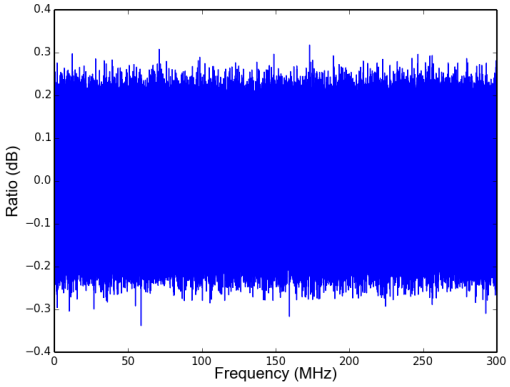

(c) 2.8 s

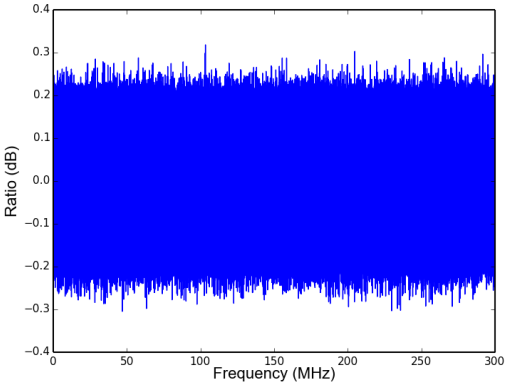

(d) 28 s

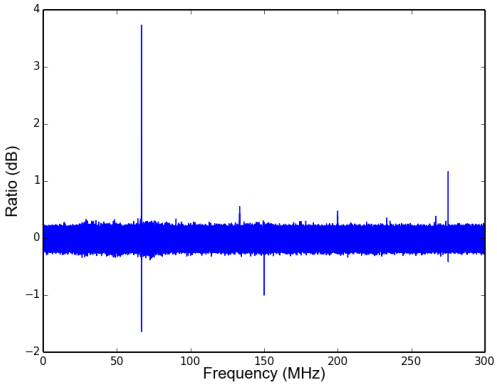

(e) 280 s

Figure 5.11: Looking at the stability of high Q spurs over time by changing the time interval between acquisitions. Each plot shows the quotient of two separate 5,000-average acquisitions (in dB) versus frequency using the setup shown in Figure 5.10 except when the time between switches was set at 280s and 20,000 total acquisitions were taken. The ratio distributions have very few spurs all the way out until the time between switches is 28 s. A large number of spurs are evident when the time between acquisitions was set to 280 s. This informs the amount of time to take before switching between the biconical antenna and a 50 Ω terminator for the next run of the experiment.

Surprisingly, spurs were quite stable even out to 28s. We can make this more quantitative by looking at the number of candidates for each run. As motivated in Chapter 3, candidates are defined by the height of the signal relative to the standard deviation of the baseline. Keeping with that premise, large signals have been defined as any signal whose magnitude is greater than 5 standard deviations (since the mean is 0 dB to high precision). For $(2^{23} - 1)$ Gaussian-distributed samples, we expect to see a mean value of 4.8 *large* signals.[4] This expectation is consistent with what is shown in Table 5.1 for all runs except for 10,000

[4]This is the product of twice (to make the result two-sided) the complementary cumulative distribution function, or the survival function, of a normal distribution, evaluated at 5 standard deviations and $\left(2^{23} - 1\right)$ (the number of samples in the displayed ratio distributions).

Acquisitions per Switch	Standard deviation (mdB)	Number of $> 5\sigma$ signals
1	61.43	7
10	61.41	6
100	61.42	5
1,000	61.41	1
10,000	62.27	96

Table 5.1: Standard deviation and number of large signals (defined as signals with a magnitude greater than 5 standard deviations) for each run shown in Figure 5.11.

acquisitions per switch where there are 96 large signals. This also agrees with qualitative visual inspection in Figure 5.11 where many more spurs are evident when the time between switches is set to 280 s versus any time between switches less than this.

This test informs how frequently we should switch back and forth for the next phase of the experiment. Specifically, it says that we should switch every 28 s, which is equal to 1,000 acquisitions. The rated switching time for the SPDT switch is 10 ms [133]. This means that even if we give 1 second to switch that the acquisition efficiency is still 96.5 % leading to a reduction in the limit on ε of 0.9 %, which is a small effect. Furthermore, since spurs are generated on the ROACH, we expect to see spurs regardless of what is on the input to the KatADC. Therefore, even though the next data run will include a biconical antenna and a 50 Ω terminator instead of two 50 Ω terminators, like in this test, this result still holds.

5.3 Reach of the proposed experiment

Using the ROACH, projections for the next run overlaid with current experimental and astrophysical limits are shown in Figure 5.12. Some discussion of the astrophysical limits and their robustness is in order. The γ–γ' CMB bound (brown) comes from conversion of normal CMB photons to dark photons and does not require that the dark photons be dark matter or even have a cosmic abundance. The γ'–γ bound (dark photon to regular photon) is model dependent because it requires that the dark photon abundance exists at the time of conversion [93]. Not only is it assumed that the dark photon is dark matter today, it assumes that it also existed back in the early universe, in most cases before matter-radiation equality when we do not actually have any evidence that dark matter existed. For the dark photon to be dark matter today but not to exist back then implies that it would have to be produced sometime between then and now (actually between then and matter-radiation equality). Thus the γ'–γ bound is weaker than other astrophysical bounds, and speculative. The intergalactic medium (IGM) heat bound arises from dark photons converting in the ionized intergalactic medium, below the plasma frequency and heating it above observed infrared (IR) bounds[134].

The dashed black line represents the forecast for the second phase of this experiment. It relies on a series of technical improvements in the different frequency bands, ranging from amplifiers at gigahertz frequencies to bolometers at terahertz. Ultimately, this experiment is limited by the warm walls of the shielded room.

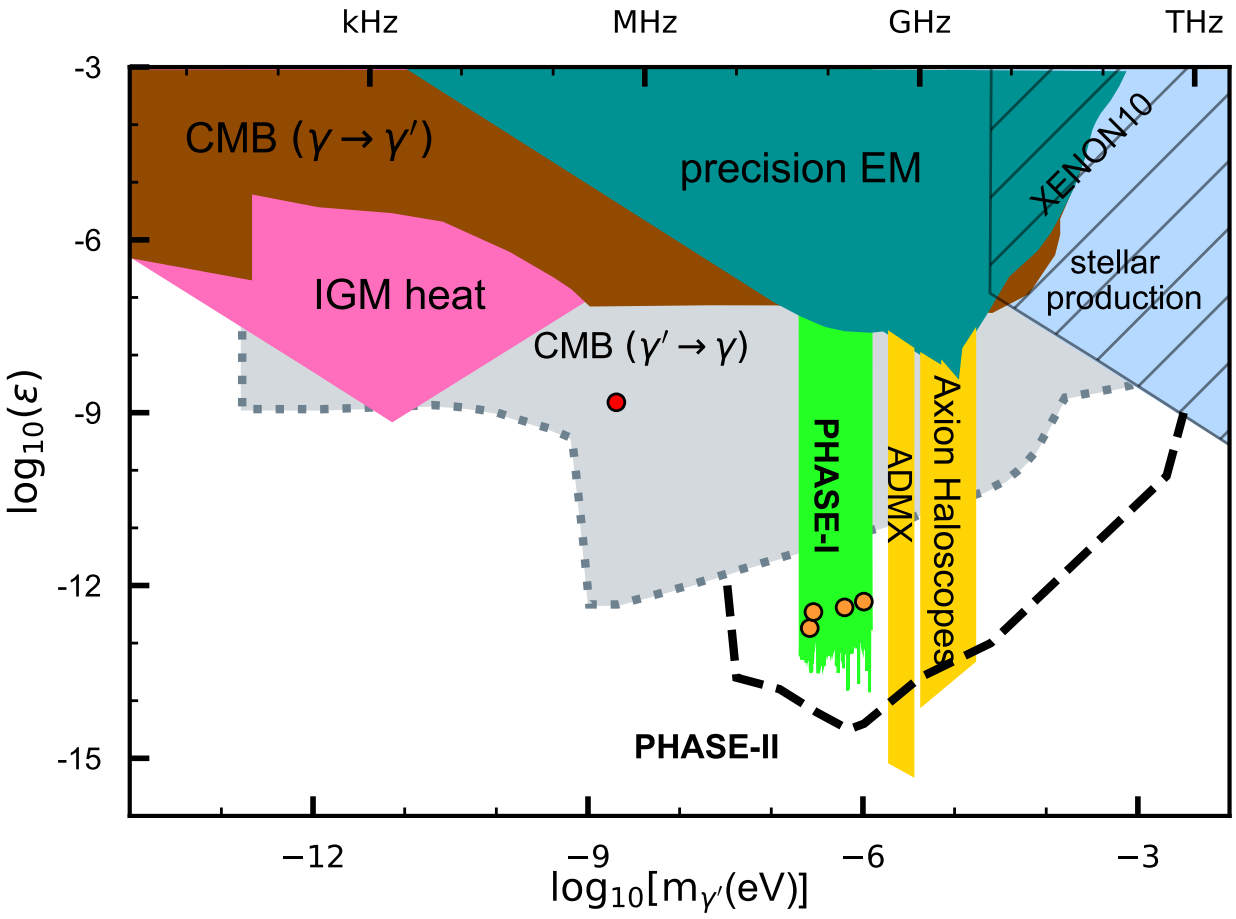

Figure 5.12: Projected reach of the Dark E-Field Radio Experiment in the next phase. The weak kinetic mixing factor is plotted versus dark photon mass in eV. The light $\gamma' - \gamma$ CMB region is a speculative model-dependent constraint above which hidden photons would not account for the total dark matter density. For reference, planned ADMX axion searches are shown in yellow, because those experiments may detect dark photons [93, 135]. Recent advances, [136, 137], may improve these limits. The orange points in Phase-I show calibrated exclusion regions at four spot frequencies at 5 σ measured in the current noisy experiment. The red dot shows the point exclusion limit measured by Phipps *et al.* (2019). The Phase-I and -II limits are based on 1 month integration using the ROACH. Phase-I green region shows 5σ extrapolated limits using the current antenna with the ROACH sampling at a resolution of 10^6 or better over the entire 50-300 MHz span. Phase-II are wide-bandwidth sampling experiments.

Chapter 6

Future Plans and Conclusions

We have demonstrated the feasibility of the Dark E-Field Radio Experiment and conducted a proof-of-concept data acquisition run between 50 and 300 MHz. Furthermore, we have developed a custom DAQ system based on the ROACH platform to perform a real-time FFT with a resolution of 10^6 or greater between 50 and 300 MHz. This chapter will conclude with a few notes about future improvements to the Dark E-Field Radio Experiment and some points of consideration as we continue to develop the experiment.

6.1 Improvements in Understanding of the AF

The AF relates the incident electric field to the measured port voltage. The coupling of the RF shield to the antenna leads to a complicated and geometry-dependent modal structure, which necessitates an accurate EM simulation to compute the AF for all the positions and

orientations of the antenna used in the data run. Furthermore, because the limit for ε is dependent on the AF, it is important to have a good understanding, both intuitive and modeled, such that greater confidence can be achieved in extracting dark photon coupling limits.

However, this is a difficult problem because not only does the AF vary over the frequency range of interest, but it also depends on its position and orientation inside the shielded room. Even more so, the dimensions of the RF shield are such that neither near-field nor far-field approximations can be made.[1] This simultaneously makes computer modeling a necessity, and intuitive understanding difficult.

In order to reduce inhomogeneity of the fields, reverberation chambers typically use large stirrers. These consist of big, metallic reflectors of various geometries that change their orientations to introduce different boundary conditions inside the chamber in a process called *mode stirring*. Moving the antenna inside the room is a manual equivalent of this process. Whereas mode stirrers physically modify the boundary conditions of the room for a fixed antenna position in order to achieve statistical uniformity, the process of changing the position of the antenna for fixed boundary conditions is essentially equivalent[139].

The next run will take advantage of this by moving the antenna to a series of different positions and orientations within the room to increase the statistical uniformity of the fields. This both reduces the inhomogeneity of the fields and also removes the risk of placing the

[1]This is traditionally defined for an electromagnetically short antenna by the distance r, in number of RF wavelengths, λ, away from the center of the antenna by $r \ll \lambda$ (Fresnel zone) and $r \gg 2\lambda$ (Fraunhofer zone), respectively [138, Section 2-31].

antenna on a null of the field.

However, the optimal number of locations in which to move the antenna has not been determined. We can estimate an adequate number of positions for antenna placement by performing Monte Carlo simulations of the average energy density at the peak frequencies of the known RF modes of a rectangular cavity with the same dimensions as the room. We choose to look at energy densities instead of field strengths because the sensitivity to ε is linearly related to the local dark matter energy density. By sampling at random locations inside the room at each of the known modes of the room (up to the highest frequency of interest), we obtain the field amplitudes at a series of points. The algorithm is as follows:

- Compute the transverse electric (TE_{mnp}) and transverse magnetic (TM_{mnp}) modes of a rectangular RF cavity with the same dimensions as the shielded room.
- For each resonance, calculate the E- and B-fields for a chosen number n points
- Calculate the energy density for each field point.
- Average all energy densities together.
- Compute a ratio of the known average energy density to the sampled energy density.
- Repeat the above steps many times for statistics.
- Compute the resulting means and standard deviations of the ratio distributions.

Room modes are specified by a wavevector $\vec{k}$ defined by

$$\vec{k} = \begin{bmatrix} k_x \\ k_y \\ k_z \end{bmatrix} = \begin{bmatrix} \frac{m\pi}{a} \\ \frac{n\pi}{b} \\ \frac{p\pi}{c} \end{bmatrix}. \tag{6.1}$$

Here, a, b, and c specify the dimensions of the room and m, n, and p are the mode numbers. Assuming that the propagation direction is in the z-direction, allowable TE-mode numbers are $m, n \in \mathbb{Z} \geq 0$ and $p \in \mathbb{Z} > 0$ with $m + n \neq 0$. Likewise, allowable TM-mode numbers are $m, n \in \mathbb{Z} > 0$ and $p \in \mathbb{Z} \geq 0$. Note that for $m, n, p \neq 0$, TE- and TM-modes are degenerate. The electric and magnetic field vectors for each mode are given by

$$\vec{E}^{TM}_{mnp} = \begin{bmatrix} \frac{-k_x k_z E_0}{k_x^2+k_y^2}\cos(k_x x)\sin(k_y y)\sin(k_z z) \\ \frac{k_y k_z E_0}{k_x^2+k_y^2}\sin(k_x x)\cos(k_y y)\sin(k_z z) \\ E_0 \sin(k_x x)\sin(k_y y)\cos(k_z z) \end{bmatrix} \tag{6.2a}$$

$$\vec{H}^{TM}_{mnp} = \begin{bmatrix} \frac{-\frac{i}{c}\sqrt{\vec{k}\cdot\vec{k}}\varepsilon_0 k_y E_0}{k_x^2+k_y^2}\sin(k_x x)\cos(k_y y)\cos(k_z z) \\ \frac{\frac{i}{c}\sqrt{\vec{k}\cdot\vec{k}}\varepsilon_0 k_x E_0}{k_x^2+k_y^2}\cos(k_x x)\sin(k_y y)\cos(k_z z) \\ 0 \end{bmatrix} \tag{6.2b}$$

$$\vec{E}^{TE}_{mnp} = \begin{bmatrix} \frac{-\frac{i}{c}\sqrt{\vec{k}\cdot\vec{k}}\mu 0 k_y H_0}{k_x^2+k_y^2}\cos(k_x x)\sin(k_y y)\sin(k_z z) \\ \frac{\frac{i}{c}\sqrt{\vec{k}\cdot\vec{k}}\mu 0 k_x H_0}{k_x^2+k_y^2}\sin(k_x x)\cos(k_y y)\sin(k_z z) \\ 0 \end{bmatrix} \tag{6.2c}$$

$$\vec{H}^{TE}_{mnp} = \begin{bmatrix} \frac{-k_x k_z H_0}{k_x^2+k_y^2}\sin(k_x x)\cos(k_y y)\cos(k_z z) \\ \frac{k_y k_z H_0}{k_x^2+k_y^2}\cos(k_x x)\sin(k_y y)\cos(k_z z) \\ H_0 \cos(k_x x)\cos(k_y y)\sin(k_z z) \end{bmatrix} \tag{6.2d}$$

These are derived in [120]. Here, the amplitude E_0 and H_0 are related via

$$\frac{E_0}{H_0} = \sqrt{\frac{\mu_0}{\varepsilon_0}} \approx 377\Omega, \tag{6.3}$$

the impedance of free space. From these fields, the energy density is then defined by

$$u = \frac{1}{2}\left[\varepsilon_0 \left(\vec{E}^{TE}_{mnp} + \vec{E}^{TM}_{mnp}\right) \cdot \left(\overline{\vec{E}^{TE}_{mnp} + \vec{E}^{TM}_{mnp}}\right) + \mu_0 \left(\vec{H}^{TE}_{mnp} + \vec{H}^{TM}_{mnp}\right) \cdot \left(\overline{\vec{H}^{TE}_{mnp} + \vec{H}^{TM}_{mnp}}\right)\right]. \tag{6.4}$$

Note that there is an implicit double count in Equation 6.4 because TE- and TM-modes are degenerate for $m, n, p \neq 0$. As a result, the calculated energy density is overestimated for $m \vee n \vee p = 0$ (the prefactor should be 1/4). This is corrected in the computation of the expected average energy density by multiplying the expected output energy density by an extra factor of 2. Computing the average energy density of the field is done by finding the average of the square of the fields. Fortunately, this integration is easy to perform over a (non-zero) integral number of periods

$$\frac{1}{2\pi|n|}\int_0^{2\pi n} \sin^2(x) = \frac{1}{2\pi|n|}\int_0^{2\pi n} \cos^2(x) = \frac{1}{2}. \tag{6.5}$$

As a result, the expected average value of the trigonometric functions in 6.2 is given by

$$2^{-d} = \frac{1}{8}, \tag{6.6}$$

where $d = 3$ is the number of spatial dimensions. The case of different propagation directions can be solved for by permuting the dimensions of the room and leaving everything else fixed.

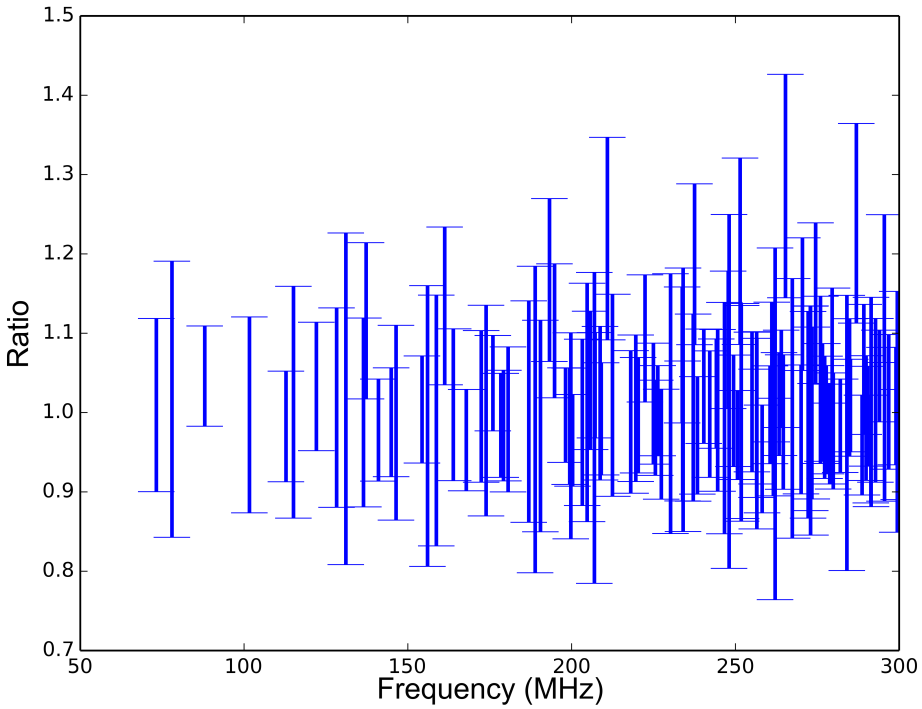

Figure 6.1: Ratio distribution of the sampled average modal energy density normalized to the analytic average energy density for 24 samples. Here, all modes less than 300 MHz are shown for a featureless, ideal room with dimension (x, y, z) = (3.07, 3.68, 2.47) m. For each mode, 100 different runs of 24 samples is done for statistics. Each data point represents the mean ratio of these 100 runs. Error bars indicate the $\pm 1\sigma$ range of this result. For this run, the mean ratio is 1.02 with a an average error of 0.101 = 10.1 %.

As an illustration, the simulations of a run consisting of moving the antenna to 24 random positions in the room are shown in Figure 6.1. Since the frequency of the dark photon is unknown, the figure of merit is the average standard deviation of the resulting distribution, which is 10 %. In other words, by moving the antenna to 24 positions in the room, the

measured energy density is accurate to 10% (assuming that equal amounts of data are taken at each antenna location). In actuality, this is a worst case scenario, because only frequencies where the mode energy is peaked are being simulated, wherein field non-uniformity is maximal. Off resonance, the field distribution will be more uniform.

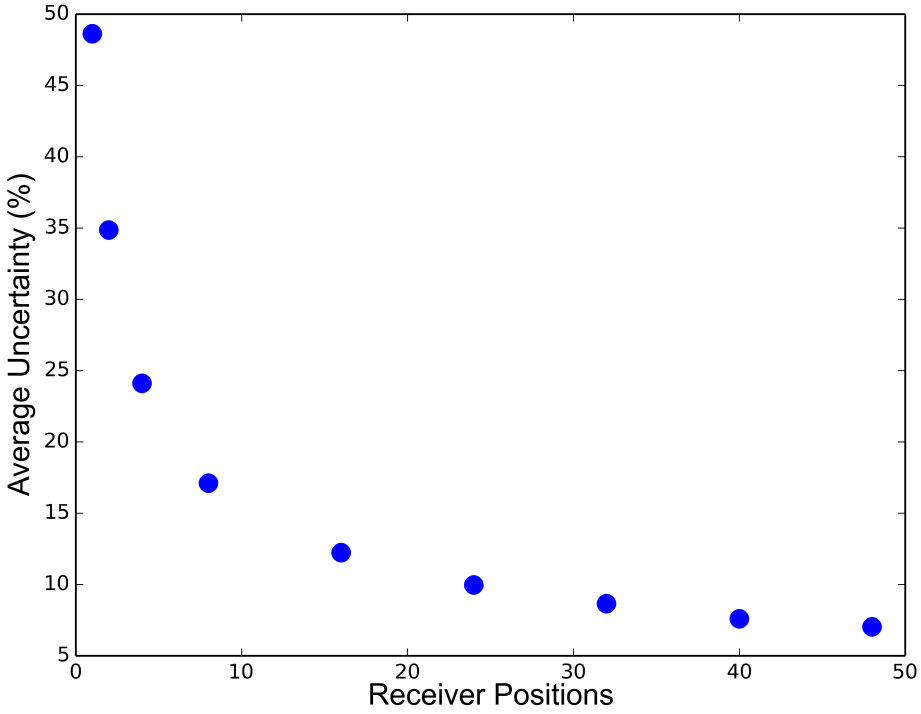

Figure 6.2: Uncertainty in the energy density plotted against the number of positions of the antenna. As expected, the uncertainty asymptotically decreases as the number of antenna positions becomes infinite. This can be used both to determine the number of locations to move the antenna but also the expected systematic uncertainty in the energy density.

This process can be repeated for different numbers of averages in the room to produce the

curve shown in Figure 6.2.[2] As expected, the uncertainty asymptotically decreases as the number of antenna positions increases. This supports the claim that this technique can be used to create a statistically uniform field environment akin to mode stirring. Also, this informs run logistics. While an increased number of antenna positions decreases the uncertainty in the measured energy density, it competes with acquisition efficiency, which falls off rapidly as it entails disruptions caused by having to manually change the location of the antenna inside the shielded room.

A statistically uniform field environment also reduces the uncertainty on AF making it significantly less prone to large fluctuations as multiple antenna positions are averaged over.

6.2 Next Run Logistics

The next run will be a two week scan over the 50–300 MHz frequency span using the new ROACH data acquisition system. It will include the veto system monitoring the RF outside of the shielded room and also the new switching scheme to reduce the effects of spurs. As argued in Section 6.1, we will move the antenna around the room to reduce uncertainty of the AF. A sample acquisition from the prototype of the event display for the next run that shows all of these pieces, is shown in Figure 6.3.

This run will inform future plans for the experiment. Increasing the run time to one year will only improve ε by a factor of 2.3 ($26^{1/4}$) over a two week run, so it makes sense to expand

[2] As before, 100 trials for each mode less than 300 MHz was calculated. Average ratio was 1, as expected for all data points shown in Figure 6.2.

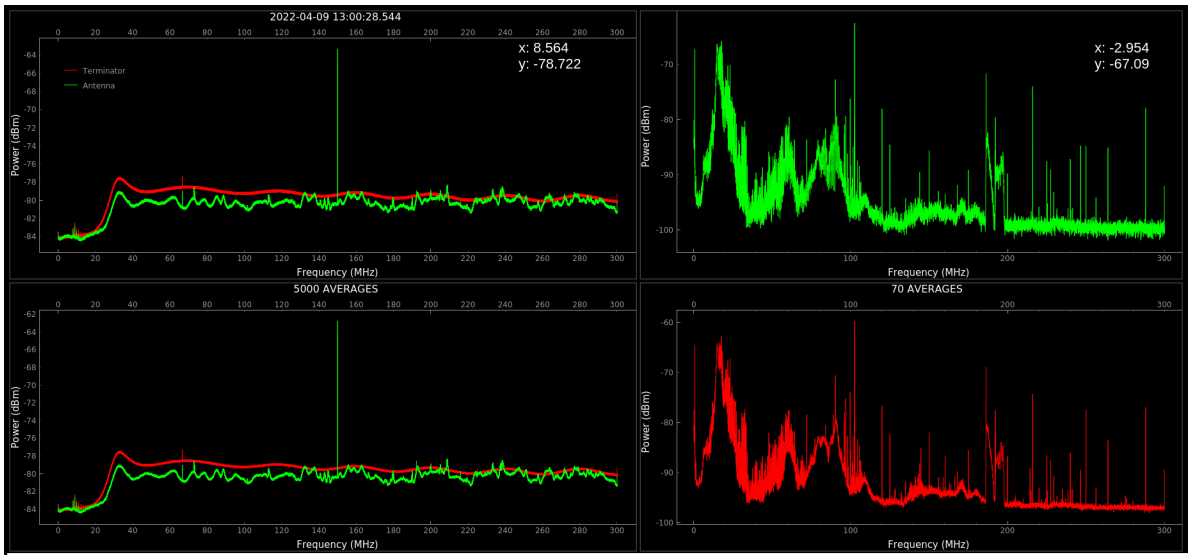

Figure 6.3: Preliminary event display showing power (in dBm) versus frequency (from 0 to 300 MHz) plots for the next run of the experiment. The left-side shows run data using the biconical antenna (green) and a 50 Ω terminator (red) inside the shielded room. Top left shows the current RMS average for a single position of the biconical antenna. Bottom left shows the total RMS average of all positions for a run. The right-side shows the spectra measured using the biconical antenna in the lab space outside the shielded room. Top-right shows the RMS average in the lab space outside the shielded room for a single position of the biconical antenna inside the shielded room. Bottom-right shows the RMS average in the lab space outside the shielded room for all positions of the antenna inside the shielded room for an entire data run. Each plot is updated as new data is acquired.

the search to other frequency bands. From Chapter 5 this can immediately be accomplished by increasing the bandwidth to 600 MHz. To maintain the resolution the FFT length will have to be increased by a factor of 2. Further span increases will require a modification of the current data acquisition system because more than a single 10 GbE line will have to be used.

It is substantially more complicated to reduce the temperature of the room. If the

temperature of the room can be lowered to that of liquid nitrogen then the temperature of the walls will be 77 K. Assuming a cryogenically cooled amplifier with a 10 K noise temperature then the the total system noise is 87 K. This will improve ε by a factor of 1.8 $[(295/87)^{1/2})]$.

Cooling the room is more viable if the dimension of the room is reduced by a factor of 10. However, this will raise the resonant frequencies of the room up by a factor of 10 as well. This technique is better adapted to searching for dark photons in the GHz regime (μeV mass range).

In total, this experiment has proven the feasibility of the Dark E-Field Experiment detection mechanism and has been used to set constraining limits on the dark photon coupling strength, ε. A combination of design and technical improvements promises to improve these limits further in future runs and also to expand the search space into other mass regions.

Bibliography

[1] I. Newton. *Opticks, or, a treatise of the reflections, refractions, inflections & colours of light*. Courier Corporation, 1952.

[2] J. B. Hearnshaw. *The Analysis of Starlight : One Hundred and Fifty Years of Astronomical Spectroscopy*. Cambridge University Press, 1986.

[3] L. D. Schmadel. *Dictionary of Minor Planet Names*. 5th ed. Springer Publishing, 2003. ISBN: 3-540-00238-3.

[4] V. Trimble. "History of Dark Matter in Galaxies". In: *Planets, Stars and Stellar Systems: Volume 5: Galactic Structure*. Ed. by Gerard Gilmore. New York, NY: Springer, 2013, pp. 1093–1116.

[5] G. Bertone and D. Hooper. "History of dark matter". In: *Reviews of Modern Physics* 90.4 (2018), p. 045002.

[6] J.C. Kapteyn. "First Attempt at a Theory of the Arrangement and Motion of the Sidereal System". In: *APJ* 55 (May 1922), p. 302. DOI: 10.1086/142670.

[7] A. Friedmann. “On the Possibility of a world with constant negative curvature of space”. In: *General Relativity and Gravitation* 31.12 (1999), pp. 2001–2008.

[8] G. Lemaitre. “Republication of: A homogeneous universe of constant mass and increasing radius accounting for the radial velocity of extra-galactic nebulae”. In: *General Relativity and Gravitation* 45.8 (2013), pp. 1635–1646.

[9] E. Hubble. “A relation between distance and radial velocity among extra-galactic nebulae”. In: *Proceedings of the national academy of sciences* 15.3 (1929), pp. 168–173.

[10] F. Zwicky. “On the Masses of Nebulae and of Clusters of Nebulae”. In: *The Astrophysical Journal* 86 (1937), p. 217.

[11] R. G. Strom. “How was atomic HI (λ= 21 cm line) in space discovered?” In: *International Journal of Modern Physics: Conference Series*. Vol. 23. World Scientific. 2013, pp. 472–477.

[12] H. I. Ewen and E. M. Purcell. “Observation of a Line in the Galactic Radio Spectrum: Radiation from Galactic Hydrogen at 1,420 Mc./sec.” In: *Nature* 168.4270 (1951), pp. 356–356.

[13] V.C. Rubin, Jr. Ford W.K., and N. Thonnard. “Extended rotation curves of high-luminosity spiral galaxies. IV. Systematic dynamical properties, Sa -¿ Sc.” In: *APJL* 225 (Nov. 1978), pp. L107–L111. DOI: 10.1086/182804.

[14] P. Pismis. “ON THE WAVY NATURE OF ROTATION CURVES IN GALAXIES”. In: *Sbc* 9600 (1965), p. 700.

[15] M. S. Roberts. “A high-resolution 21-CM hydrogen-line survey of the Andromeda nebula”. In: *The Astrophysical Journal* 144 (1966), p. 639.

[16] V. C. Rubin and Jr. Ford W. K. “Rotation of the Andromeda nebula from a spectroscopic survey of emission regions”. In: *The Astrophysical Journal* 159 (1970), p. 379.

[17] K. C. Freeman. “On the disks of spiral and S0 galaxies”. In: *The Astrophysical Journal* 160 (1970), p. 811.

[18] J. A. Tyson, G. P. Kochanski, and I. P. Dell’Antonio. “Detailed mass map of CL 0024+ 1654 from strong lensing”. In: *The Astrophysical Journal* 498.2 (1998), p. L107.

[19] L. L. R. Williams and P. L. Schechter. “The quest for the golden lens”. In: *Astronomy & Geophysics* 38.5 (1997), pp. 10–14.

[20] A. Einstein and H. Minkowski. *The principle of relativity: original papers*. University of Calcutta, 1920.

[21] A. Einstein. “Die Grundlage der allgemeinen Relativitätstheorie”. In: *Annalen der Physik* 354.7 (1916), pp. 769–822. DOI: https://doi.org/10.1002/andp.19163540702. eprint: https://onlinelibrary.wiley.com/doi/pdf/10.1002/andp.19163540702. URL: https://onlinelibrary.wiley.com/doi/abs/10.1002/andp.19163540702.

[22] T. Sauer. "Nova Geminorum 1912 and the origin of the idea of gravitational lensing". In: *Archive for history of exact sciences* 62.1 (2008), pp. 1–22.

[23] D. Valls-Gabaud. "The conceptual origins of gravitational lensing". In: *AIP Conference Proceedings*. Vol. 861. 1. American Institute of Physics. 2006, pp. 1163–1163.

[24] A. Einstein. "Lens-like action of a star by the deviation of light in the gravitational field". In: *Science* 84.2188 (1936), pp. 506–507.

[25] D. Walsh, R. F. Carswell, and R. J. Weymann. "0957+ 561 A, B: twin quasistellar objects or gravitational lens?" In: *Nature* 279.5712 (1979), pp. 381–384.

[26] M. Bartelmann. "Gravitational lensing". In: *Classical and Quantum Gravity* 27.23 (2010), p. 233001.

[27] D. Clowe et al. "A direct empirical proof of the existence of dark matter". In: *The Astrophysical Journal* 648.2 (2006), p. L109.

[28] A. R. Liddle. "Acceleration of the universe". In: *New Astronomy Reviews* 45.4-5 (2001), pp. 235–253.

[29] M. Tanabashi et al. "Review of Particle Physics". In: *Phys. Rev. D* 98 (3 Aug. 2018), p. 030001. DOI: 10.1103/PhysRevD.98.030001. URL: https://link.aps.org/doi/10.1103/PhysRevD.98.030001.

[30] M. Williams. "Cosmic Dawn Holds the Answers to Many of Astronomy's Greatest Questions". In: *Phys Org* (Sept. 15, 2021). URL: https://phys.org/news/2021-09-cosmic-dawn-astronomy-greatest.html (visited on 09/15/2021).

[31] W. Hu and S. Dodelson. "Cosmic microwave background anisotropies". In: *Annual Review of Astronomy and Astrophysics* 40.1 (2002), pp. 171–216.

[32] Planck Collaboration et al. "Planck 2015 Results: I. Overview of Products and Scientific Results". In: *Astronomy & Astrophysics* 594 (2015), pp. 1–38.

[33] A. A. Penzias and R. W. Wilson. "A measurement of excess antenna temperature at 4080 Mc/s." In: *The Astrophysical Journal* 142 (1965), pp. 419–421.

[34] C. L. Bennett et al. "Four-year COBE DMR cosmic microwave background observations: maps and basic results". In: *The Astrophysical Journal* 464.1 (1996), p. L1.

[35] C. L. Bennett et al. "Nine-year Wilkinson Microwave Anisotropy Probe (WMAP) observations: final maps and results". In: *The Astrophysical Journal Supplement Series* 208.2 (2013), p. 20.

[36] N. Aghanim et al. "Planck 2018 results". In: *Astronomy & Astrophysics* 641 (Sept. 2020), A6. ISSN: 1432-0746. DOI: 10.1051/0004-6361/201833910. URL: http://dx.doi.org/10.1051/0004-6361/201833910.

[37] B. Bassett and R. Hlozek. "Baryon acoustic oscillations". In: *Dark energy: observational and theoretical approaches* (2010), p. 246.

[38] C. H. Lineweaver. "Inflation and the cosmic microwave background". In: *The New Cosmology*. World Scientific, 2005, pp. 31–65.

[39] W. Hu. *Intermediate Guide to the Acoustic Peaks and Polarization*. 2001. URL: http://background.uchicago.edu/~whu/intermediate/intermediate.html (visited on 04/20/2022).

[40] R. J. Nemiroff and B. Patla. "Adventures in Friedmann cosmology: A detailed expansion of the cosmological Friedmann equations". In: *American Journal of Physics* 76.3 (2008), pp. 265–276.

[41] E. J. Copeland, M. Sami, and S. Tsujikawa. "Dynamics of dark energy". In: *International Journal of Modern Physics D* 15.11 (2006), pp. 1753–1935.

[42] G. Steigman. "Primordial Nucleosynthesis in the Precision Cosmology Era". In: *Annu. Rev. Nucl. Part. Sci.* 57 (2007), pp. 463–491.

[43] A. Coc and E. Vangioni. "Primordial Nucleosynthesis". In: *International Journal of Modern Physics E* 26.08 (2017), p. 1741002.

[44] B. D. Fields et al. "Big-Bang Nucleosynthesis after Planck". In: *Journal of Cosmology and Astroparticle Physics* 2020.03 (Mar. 2020), pp. 010–010. ISSN: 1475-7516. DOI: 10.1088/1475-7516/2020/03/010. URL: http://dx.doi.org/10.1088/1475-7516/2020/03/010.

[45] R. J. Cooke, M. Pettini, and C. C. Steidel. "One percent determination of the primordial deuterium abundance". In: *The Astrophysical Journal* 855.2 (2018), p. 102.

[46] P. Motloch. "Testing consistency of Ω b h^2 in the Planck data". In: *Physical Review D* 101.12 (2020), p. 123509.

[47] J. L. Feng et al. *Planning the Future of U.S. Particle Physics (Snowmass 2013): Chapter 4: Cosmic Frontier*. 2014. arXiv: 1401.6085 [hep-ex].

[48] K. Griest. "The Search for the Dark Matter: WIMPs and MACHOs". In: *Annals of the New York Academy of Sciences* 688.1 (June 1993), pp. 390–407. ISSN: 0077-8923. DOI: 10.1111/j.1749-6632.1993.tb43912.x. URL: http://dx.doi.org/10.1111/j.1749-6632.1993.tb43912.x.

[49] A. Gould. "Extending the MACHO search to about 10^6 solar masses". In: *The Astrophysical Journal* 392 (1992), pp. 442–451.

[50] J. Hart et al. "The telescope system of the macho program". In: *Publications of the Astronomical Society of the Pacific* 108.720 (1996), p. 220.

[51] C. Alcock et al. "MACHO Project Limits on Black Hole Dark Matter in the 1–30 $10^{-6}M_{\odot}$ Range". In: *The Astrophysical Journal* 550.2 (Apr. 2001), pp. L169–L172. ISSN: 0004-637X. DOI: 10.1086/319636. URL: http://dx.doi.org/10.1086/319636.

[52] C. Alcock et al. "EROS and MACHO Combined Limits on Planetary-Mass Dark Matter in the Galactic Halo". In: *The Astrophysical Journal* 499.1 (May 1998), pp. L9–L12. ISSN: 0004-637X. DOI: 10.1086/311355. URL: http://dx.doi.org/10.1086/311355.

[53] C. Alcock et al. “The MACHO Project: Microlensing Results from 5.7 Years of Large Magellanic Cloud Observations”. In: *The Astrophysical Journal* 542.1 (Oct. 2000), pp. 281–307. ISSN: 1538-4357. DOI: 10.1086/309512. URL: http://dx.doi.org/10.1086/309512.

[54] Y. R. Rahal et al. “The EROS2 search for microlensing events towards the spiral arms: the complete seven season results”. In: *Astronomy & Astrophysics* 500.3 (Apr. 2009), pp. 1027–1044. ISSN: 1432-0746. DOI: 10.1051/0004-6361/200811515. URL: http://dx.doi.org/10.1051/0004-6361/200811515.

[55] S. N. Calchi and L. Mancini. “Microlensing towards the Large Magellanic Cloud: Self-lensing for OGLE-II and OGLE-III”. In: *Monthly Notices of the Royal Astronomical Society* 416.2 (2011), pp. 1292–1301.

[56] C. Corianò and P. H Frampton. “Does CMB Distortion Disfavour Intermediate Mass Dark Matter?” In: *arXiv preprint arXiv:2012.13821* (2020).

[57] J. Ricotti, J. P. Ostriker, and K. J. Mack. “Effect of Primordial Black Holes on the Cosmic Microwave Background and Cosmological Parameter Estimates”. In: *The Astrophysical Journal* 680.2 (June 2008), pp. 829–845. ISSN: 1538-4357. DOI: 10.1086/587831. URL: http://dx.doi.org/10.1086/587831.

[58] Y. Ali-Haïmoud and M. Kamionkowski. “Cosmic microwave background limits on accreting primordial black holes”. In: *Physical Review D* 95.4 (Feb. 2017). ISSN: 2470-

0029. DOI: 10.1103/physrevd.95.043534. URL: http://dx.doi.org/10.1103/PhysRevD.95.043534.

[59] B. Carr et al. "Constraints on primordial black holes". In: *Reports on Progress in Physics* 84.11 (Nov. 2021), p. 116902. ISSN: 1361-6633. DOI: 10.1088/1361-6633/ac1e31. URL: http://dx.doi.org/10.1088/1361-6633/ac1e31.

[60] G. Arcadi et al. "The Waning of the WIMP? A Review of Models, Searches, and Constraints". In: *Eur. Phys. J. C* 78.3 (2018), pp. 1–57. URL: https://arxiv.org/abs/1703.07364.

[61] P. Cushman et al. "Snowmass CF1 summary: WIMP dark matter direct detection". In: *arXiv preprint arXiv:1310.8327* (2013).

[62] T. M. Undagoitia and L. Rauch. "Dark matter direct-detection experiments". In: *Journal of Physics G: Nuclear and Particle Physics* 43.1 (2015), p. 013001.

[63] Laura. Baudis and (The DARWIN Collaboration). "DARWIN dark matter WIMP search with noble liquids". In: 375.1 (July 2012), p. 012028. DOI: 10.1088/1742-6596/375/1/012028. URL: https://doi.org/10.1088/1742-6596/375/1/012028.

[64] Y. Fukuda et al. "Evidence for Oscillation of Atmospheric Neutrinos". In: *Physical Review Letters* 81.8 (Aug. 1998), pp. 1562–1567. ISSN: 1079-7114. DOI: 10.1103/physrevlett.81.1562. URL: http://dx.doi.org/10.1103/PhysRevLett.81.1562.

[65] J. N. Bahcall and Jr. Davis R. "Solar neutrinos: a scientific puzzle". In: *Science* 191.4224 (1976), pp. 264–267.

[66] Q. R. Ahmad et al. "Measurement of the Rate of $\nu_e + d \rightarrow p + p + e^-$ Interactions Produced by ^8B Solar Neutrinos at the Sudbury Neutrino Observatory". In: *Phys. Rev. Lett.* 87 (7 July 2001), p. 071301. DOI: 10.1103/PhysRevLett.87.071301. URL: https://link.aps.org/doi/10.1103/PhysRevLett.87.071301.

[67] F. Capozzi et al. "Global constraints on absolute neutrino masses and their ordering". In: *Physical Review D* 95.9 (2017), p. 096014.

[68] S. Dodelson and L. M. Widrow. "Sterile neutrinos as dark matter". In: *Physical Review Letters* 72.1 (1994), p. 17.

[69] M. Drewes. "The phenomenology of right handed neutrinos". In: *International Journal of Modern Physics E* 22.08 (2013), p. 1330019.

[70] A. A. Aguilar-Arevalo et al. "Significant Excess of Electronlike Events in the MiniBooNE Short-Baseline Neutrino Experiment". In: *Physical Review Letters* 121.22 (Nov. 2018). ISSN: 1079-7114. DOI: 10.1103/physrevlett.121.221801. URL: http://dx.doi.org/10.1103/PhysRevLett.121.221801.

[71] P. B. Denton. "Sterile Neutrino Searches with MicroBooNE: Electron Neutrino Disappearance". In: *arXiv preprint arXiv:2111.05793* (2021).

[72] S. Böser et al. "Status of light sterile neutrino searches". In: *Progress in Particle and Nuclear Physics* 111 (Mar. 2020), p. 103736. ISSN: 0146-6410. DOI: 10.1016/j.ppnp.2019.103736. URL: http://dx.doi.org/10.1016/j.ppnp.2019.103736.

[73] H. -Y. Cheng. "The strong CP problem revisited". In: *Physics Reports* 158.1 (1988), pp. 1–89.

[74] M. Kawasaki et al. "Oscillons of axion-like particle: mass distribution and power spectrum". In: *Journal of Cosmology and Astroparticle Physics* 2021.01 (Jan. 2021), pp. 061–061. ISSN: 1475-7516. DOI: 10.1088/1475-7516/2021/01/061. URL: http://dx.doi.org/10.1088/1475-7516/2021/01/061.

[75] I. Stern. *ADMX Status*. 2017. arXiv: 1612.08296 [physics.ins-det].

[76] J. Preskill, M. B. Wise, and F. Wilczek. "Cosmology of the invisible axion". In: *Physics Letters B* 120.1-3 (1983), pp. 127–132.

[77] L. F. Abbott and P. Sikivie. "A cosmological bound on the invisible axion". In: *Physics Letters B* 120.1-3 (1983), pp. 133–136.

[78] M. Dine and W. Fischler. "The not-so-harmless axion". In: *Physics Letters B* 120.1-3 (1983), pp. 137–141.

[79] A. E. Nelson and J. Scholtz. "Dark light, dark matter, and the misalignment mechanism". In: *Physical Review D* 84.10 (Nov. 2011). ISSN: 1550-2368. DOI: 10.1103/physrevd.84.103501. URL: http://dx.doi.org/10.1103/PhysRevD.84.103501.

[80] P. J. E. Peebles. "Large-scale background temperature and mass fluctuations due to scale-invariant primeval perturbations". In: *apjl* 263 (Dec. 1982), pp. L1–L5. DOI: 10.1086/183911.

[81] Joel R. Primack. *Whatever Happened to Hot Dark Matter?* 2001. arXiv: astro-ph/0112336 [astro-ph].

[82] Julio F Navarro. "The structure of cold dark matter halos". In: *Symposium-international astronomical union*. Vol. 171. Cambridge University Press. 1996, pp. 255–258.

[83] D. N. Spergel and P. J. Steinhardt. "Observational evidence for self-interacting cold dark matter". In: *Physical review letters* 84.17 (2000), p. 3760.

[84] A. Browman et al. "The Decay Width of the Neutral pi Meson". In: *Phys. Rev. Lett.* 33 (1974), p. 1400. DOI: 10.1103/PhysRevLett.33.1400.

[85] A. Caputo et al. "Dark photon limits: A handbook". In: *Phys. Rev. D* 104 (9 Nov. 2021), p. 095029. DOI: 10.1103/PhysRevD.104.095029. URL: https://link.aps.org/doi/10.1103/PhysRevD.104.095029.

[86] H. Primakoff. "Photo-Production of Neutral Mesons in Nuclear Electric Fields and the Mean Life of the Neutral Meson". In: *Phys. Rev.* 81 (5 Mar. 1951), pp. 899–899. DOI: 10.1103/PhysRev.81.899. URL: https://link.aps.org/doi/10.1103/PhysRev.81.899.

[87] L. M. Capparelli et al. "Axion-like particle searches with sub-THz photons". In: *Physics of the Dark Universe* 12 (2016), pp. 37–44.

[88] P. Sikivie. "Experimental Tests of the "Invisible" Axion". In: *Phys. Rev. Lett.* 51 (16 Oct. 1983), pp. 1415–1417. DOI: 10.1103/PhysRevLett.51.1415. URL: https://link.aps.org/doi/10.1103/PhysRevLett.51.1415.

[89] S. J. Asztalos et al. "SQUID-Based Microwave Cavity Search for Dark-Matter Axions". In: *Physical Review Letters* 104.4 (Jan. 2010). ISSN: 1079-7114. DOI: 10.1103/physrevlett.104.041301. URL: http://dx.doi.org/10.1103/PhysRevLett.104.041301.

[90] M. Silva-Feaver et al. "Design Overview of DM Radio Pathfinder Experiment". In: *IEEE Transactions on Applied Superconductivity* 27.4, 2631425 (June 2017), p. 2631425. DOI: 10.1109/TASC.2016.2631425.

[91] A. Phipps et al. "Exclusion limits on hidden-photon dark matter near 2 nev from a fixed-frequency superconducting lumped-element resonator". In: *Microwave Cavities and Detectors for Axion Research*. Springer, 2020, pp. 139–145.

[92] A. Wagner et al. "Search for hidden sector photons with the admx detector". In: *Physical review letters* 105.17 (2010), p. 171801.

[93] P. Arias et al. "WISPy cold dark matter". In: *J. Cosmol. Astropart. Phys.* 2012.06 (June 2012), p. 013. URL: https://arxiv.org/abs/1201.5902.

[94] P.W. Graham, J. Mardon, and S. Rajendran. "Vector Dark Matter from Inflationary Fluctuations". In: *Phys. Rev. D* 93 (2016), p. 103520. URL: https://arxiv.org/abs/1504.02102.

[95] B. Holdom. "Two U(1)'s and $\in$ charge shifts". In: *Phys. Lett. B* 166.2 (Jan. 1986), p. 196. DOI: 10.1016/0370-2693(86)91377-8.

[96] R. Foot and X.-G. He. "Comment on Z-Z' mixing in extended gauge theories". In: *Phys. Lett. B* 267.4 (Sept. 1991), p. 509. DOI: 10.1016/0370-2693(91)90901-2.

[97] T.G. Rizzo. "Kinetic mixing and portal matter phenomenology". In: *Phys. Rev. D* 99.11 (June 2019), p. 115024. URL: https://arxiv.org/abs/1810.07531.

[98] M. Tanabashi et al. "Review of Particle Physics". In: *Phys. Rev. D* 98 (3 Aug. 2018), p. 030001. DOI: 10.1103/PhysRevD.98.030001. URL: https://link.aps.org/doi/10.1103/PhysRevD.98.030001.

[99] M. Fabbrichesi, E. Gabrielli, and G. Lanfranchi. "The dark photon". In: *arXiv preprint arXiv:2005.01515* (2020).

[100] Z. Maki, M. Nakagawa, and S. Sakata. "Remarks on the unified model of elementary particles". In: *Progress of Theoretical Physics* 28.5 (1962), pp. 870–880.

[101] T. Hawkins. "Cauchy and the Spectral Theory of Matrices". In: *Historia mathematica* 2.1 (1975), pp. 1–29.

[102] M. Fabbrichesi, E. Gabrielli, and G. Lanfranchi. *The Physics of the Dark Photon: A Primer*. Springer, 2021.

[103] A. S. Goldhaber and M. M. Nieto. "Photon and graviton mass limits". In: *Reviews of Modern Physics* 82.1 (2010), p. 939.

[104] M. Luty. *Massless Spin 1 Particles and Gauge Fields Physics 230B Lecture Notes*. Oct. 2021.

[105] M. Luty. *Massive Spin 1 Particles and Vector Fields Physics 230B Lecture Notes*. Oct. 2021.

[106] M. Schumann. "Direct Detection of WIMP Dark Matter: Concepts and Status". In: *J. Phys. G* 46.10 (2019), p. 103003. URL: https://arxiv.org/abs/1903.03026.

[107] S. Ritz et al. *Building for Discovery: Strategic Plan for US Particle Physics in the Global Context*. 2014. URL: https://www.usparticlephysics.org/.

[108] M. Battaglieri et al. "US Cosmic Visions: New Ideas in Dark Matter 2017: Community Report". In: 2017. arXiv: 1707.04591. URL: https://arxiv.org/abs/1707.04591.

[109] S.R. Parker et al. "Cryogenic resonant microwave cavity searches for hidden sector photons". In: *Phys. Rev. D* 88 (11 2013), p. 112004. URL: https://arxiv.org/abs/1410.5244.

[110] S. Chaudhuri et al. "Radio for hidden-photon dark matter detection". In: *Phys. Rev. D* 92 (7 Oct. 2015), p. 075012. URL: https://arxiv.org/abs/1411.7382.

[111] K. Freese, M. Lisanti, and C. Savage. "Annual modulation of dark matter: a review". In: *arXiv preprint arXiv:1209.3339* (2012).

[112] *40 dB Gain, 0.8 dB NF, 18 dBm P1dB, 10 MHz to 1,000 MHz, Low Noise High Gain Amplifier SMA*. PE15A1012. Rev 1.0. Pasternack Enterprises Inc. 2015.

[113] F. J. Harris. "On the use of windows for harmonic analysis with the discrete Fourier transform". In: *Proceedings of the IEEE* 66.1 (1978), pp. 51–83.

[114] *RSA5000 Series Real-time Spectrum Analyzer*. UGD20101-1110. Rigol Technologies, Inc. 2017.

[115] J. O. Smith. *Spectral Audio Signal Processing*. online book, 2011 edition. http://ccrma.stanford.edu/~jos/sasp/, 2022.

[116] *Antenna Factor*. http://web.archive.org/web/20220210164807/https://www.antenna-theory.com/definitions/antennafactor.php. Accessed: 2022-05-18.

[117] R. H. Dicke. "The Measurement of Thermal Radiation at Microwave Frequencies". In: *Rev. Sci. Instrum.* 17 (1946), p. 268. DOI: 10.1063/1.1770483. URL: https://aip.scitation.org/doi/10.1063/1.1770483.

[118] *COMSOL Multiphysics*. 5.4. Available at https://www.comsol.com/. COMSOL, Inc. One First Street, Suite 4 Los Altos, CA 94022.

[119] *CST Microwave Studio 2019*. 2019. Available at https://www.3ds.com/products-services/simulia/products/cst-studio-suite/. Dassault Systemes, Inc. 625 Market St #14, San Francisco, CA 94105.

[120] D. Hill. *Electromagnetic Fields in Cavities*. Hoboken, N.J.: Wiley, 2009. DOI: 10.1002/9780470495056.

[121] A. V. Oppenheim and R. W. Schafer. *Discrete-Time Signal Processing*. 3rd ed. Schafer, 2010.

[122] H. Fischer. *A history of the central limit theorem: From classical to modern probability theory*. Springer, 2011.

[123] A. Phipps et al. "Exclusion Limits on Hidden-Photon Dark Matter near 2 neV from a Fixed-Frequency Superconducting Lumped-Element Resonator". In: *Springer Proc. Phys.* 245 (2020), p. 139. URL: https://arxiv.org/abs/1906.08814.

[124] *SMA Connectors*. Available at https://web.archive.org/web/20220104004849/https://www.amphenolrf.com/connectors/sma-connectors.html. Amphenol® RF. 2020.

[125] J. Hickish et al. "A Decade of Developing Radio-Astronomy Instrumentation using CASPER Open-Source Technology". In: *J. Astron. Instrum.* 5.4, 1641001 (Dec. 2016), p. 1641001. URL: https://arxiv.org/abs/1611.01826.

[126] *KatADC*. https://casper.astro.berkeley.edu/wiki/KatADC. Accessed: 2022-05-19.

[127] *Z- DOK* and Z- DOK + Connectors*. Available at https://www.te.com/commerce/DocumentDelivery/DDEController?Action=showdoc&DocId=Specification+Or+Standard%7F114-13068%7FC%7Fpdf%7FEnglish%7FENG_SS_114-13068_C.pdf%7F6367555-1. TE Connectivity. Apr. 2011.

[128] *Virtex-6 Family Overview*. Available at https://docs.xilinx.com/v/u/en-US/ds150. Xilinx. Aug. 2015.

[129] X. Lin. *Spurs Analysis in the RF Sampling ADC*. Texas Instruments, 2018.

[130] W. Kester. *Understand SINAD, ENOB, SNR, THD, THD + N, and SFDR so You Don't Get Lost in the Noise Floor*. English. Version Revision A. Oct. 2008. 8 pp.

[131] G. B. Rybicki and A. P. Lightman. *Radiative Processes in Astrophysics*. Wiley-VCH, 2004.

[132] *ADC08D1520 Low Power, 8-Bit, Dual 1.5 GSPS or Single 3.0 GSPS A/D Converter*. ADC08D1520. Texas Instruments. Mar. 2013.

[133] *SPDT Ramses SMA 3GHz Failsafe 12Vdc TTL Diodes Pins Terminals*. R57031210. Radiall. 2017.

[134] S. Dubovsky and G. Hernández-Chifflet. "Heating up the Galaxy with hidden photons". In: *J. Cosmol. Astropart. Phys.* 2015.12, 054 (Dec. 2015), p. 054. URL: https://arxiv.org/abs/1509.00039.

[135] A. Wagner et al. "Search for hidden sector photons with the ADMX detector". In: *Phys. Rev. Lett.* 105.17 (2010), p. 171801. URL: https://arxiv.org/abs/1007.3766.

[136] N. Du et al. "Search for Invisible Axion Dark Matter with the Axion Dark Matter Experiment". In: *Phys. Rev. Lett.* 120 (15 Apr. 2018), p. 151301. URL: https://arxiv.org/abs/1804.05750.

[137] T. Braine et al. "Extended Search for the Invisible Axion with the Axion Dark Matter Experiment". In: *Phys. Rev. Lett.* 124 (10 Mar. 2020), p. 101303. URL: https://arxiv.org/abs/1910.08638.

[138] J. D. Kraus. *Antennas*. Ed. by A. E. Elken. 2nd ed. United States of America: McGraw-Hill, Inc., 1988.

[139] R. Serra et al. "Reverberation chambers a la carte: An overview of the different mode-stirring techniques". In: *IEEE Electromagnetic Compatibility Magazine* 6.1 (2017), pp. 63–78.